HYPERVELOCITY JET INTERACTION WITH LIGHTWEIGHT FLYER PLATES

A THESIS SUBMITTED TO
THE GRADUATE SCHOOL OF NATURAL AND APPLIED SCIENCES
OF
THE MIDDLE EAST TECHNICAL UNIVERSITY

BY
TANSEL DENİZ

IN PARTIAL FULFILLMENT OF THE REQUIREMENTS
FOR
THE DEGREE OF DOCTOR OF PHILOSOPHY
IN
THE DEPARTMENT OF MECHANICAL ENGINEERING

JANUARY 2022

Approval of the thesis:

HYPERVELOCITY JET INTERACTION WITH LIGHTWEIGHT FLYER PLATES

Submitted by **TANSEL DENİZ** in partial fulfillment of the requirements for the degree of **Doctor of Philosophy in Mechanical Engineering Department, Middle East Technical University** by,

Prof. Dr. Halil Kalıpçılar
Dean, Graduate School of **Natural and Applied Sciences** _____

Prof. Dr. M. A. Sahir Arıkan
Head of Department, **Mechanical Engineering** _____

Prof. Dr. Metin Akkök
Supervisor, **Mechanical Eng. Dept., METU** _____

Prof. Dr. R. Orhan Yıldırım
Co-Supervisor, **Mechanical Eng. Dept., METU** _____

Examining Committee Members:

Assoc. Prof. Dr. Hüsnü Dal
Mechanical Engineering Dept., METU _____

Prof. Dr. Metin Akkök
Mechanical Engineering Dept., METU _____

Prof. Dr. Ömer Anlağan
Mechanical Engineering Dept., Bilkent University _____

Prof. Dr. Bilgehan Ögel
Metallurgical and Materials Engineering Dept., METU _____

Prof. Dr. S. Kemal İder
Mechanical Engineering Dept., Çankaya University _____

Date: **20.01.2022**

I hereby declare that all information in this document has been obtained and presented in accordance with academic rules and ethical conduct. I also declare that, as required by these rules and conduct, I have fully cited and referenced all material and results that are not original to this work.

Name, Last name : TANSEL DENİZ

Signature : _____

ABSTRACT

HYPERVELOCITY JET INTERACTION WITH LIGHTWEIGHT FLYER PLATES

Deniz, Tansel
Ph.D., Department of Mechanical Engineering
Supervisor: Prof. Dr. Metin Akkök
Co-Supervisor: Prof. Dr. R. Orhan Yıldırım

January 2022, 129 pages

Explosive Reactive Armor (ERA) is an efficient way of defeating threats with shaped charge warheads. It comprises an explosive layer between two steel plates. In the typical arrangement, cassettes are placed in obliquity to the flight path of the jet. Shaped charge jet detonates the explosive layer and flyer plates are accelerated in opposite directions. The mechanism of the plates is to deflect or disrupt the jet. On the other hand, the plates may damage the structure of the vehicle. Moreover, the plates flying in the outer direction may possess a threat to nearby personnel or vehicles. To overcome this shortcoming, it is plausible to propose cassettes with brittle or low-density materials.

This thesis aims to investigate the potential of ceramics and glass as flyer plate materials. First, the ballistic protection performance of steel-steel cassettes with varying plate and explosive layer thickness is examined. Then, for a given areal density, the front and back plates of the cassette are changed selectively with alternative materials, and the ballistic performance is tested. The materials that reveal the best performance as front and back plates are selected. Finally, the performance of non-steel cassettes with selected materials

is investigated. Hydrocode numerical modeling is performed to understand the nature of the interaction between jet and flyer plates.

It is seen that ceramics can be used as a replacement for steel in ERA, achieving similar or even better efficiency. It is also revealed that the performance of ceramic flyer plates depends on compressive strength, fracture toughness, and bulk impedance.

Keywords: flyer plate, hypervelocity jet, reactive cassettes, ERA, ceramics

ÖZ

HAFİF MALZEMELERDEN OLUŞAN UÇAN PLAKA İLE YÜKSEK HIZLI JET ETKİLEŞİMİ

Deniz, Tansel
Doktora, Makina Mühendisliği Bölümü
Tez Yöneticisi: Prof. Dr. Metin Akkök
Ortak Tez Yöneticisi: Prof. Dr. R. Orhan Yıldırım

Ocak 2022, 129 sayfa

Patlayıcı tepkimeli zırh (PTZ), çukur imlâlı harp başlığı içeren tehditlere karşı kullanılan etkili bir yöntemdir. PTZ kaseti, iki çelik plakanın arasına patlayıcı bir katmanın yerleştirilmesi ile oluşur. Tipik bir uygulamada kasetler, tehdidin geliş doğrultusuna açılı olarak yerleştirilir. Çukur imla jeti, patlayıcı katmanı infilak ettirerek uçan plakaları karşıt yönlerde ivmelendirir. Uçan plakalar; çukur imla jetinin saptırılması ve/veya bozulması mekanizmaları ile çalışır. Öte yandan, söz konusu uçan plakalar, uygulama yapılan aracın yapısına zarar verebilir. Ayrıca dışarı yönde ivmelenen plakalar çevredeki personel veya diğer araçlar için tehlike arz edebilir. Bahsedilen olumsuzlukları gidermek için, kırılgan ve/veya düşük yoğunluklu malzemelerden üretilen plakalar içeren PTZ kasetlerinin uygulanabileceği değerlendirilmiştir.

Bu tezin amacı; cam ve seramik tipi malzemelerin PTZ uçan plakası olarak potansiyelinin değerlendirilmesidir. İlk olarak, çelik plakalardan oluşan PTZ kasetlerinde uçan plaka ve patlayıcı kalınlığının balistik koruma performansına etkisi incelenmiştir. Daha sonra seçilen sabit bir alansal yoğunluk için çelik-çelik PTZ kasetlerinde ön ve arka çelik plakalar sırası ile aday malzemeler ile değiştirilmiştir. Ön ve arka plaka olarak en yüksek

performansı sağlayan aday malzemeler seçilerek çelik plaka içermeyen PTZ kasetleri oluşturulmuş ve performansları test edilmiştir. Bu çalışmalara ek olarak çukur imla jeti ile uçan plakalar arasındaki etkileşimin incelenmesi amacı ile hidrokod sayısal benzetimler gerçekleştirilmiştir.

Çalışma sonucunda, PTZ kasetlerinde çelik yerine seramikler kullanılarak çelik kasete benzer ve hatta daha yüksek performanslar elde edilebileceği anlaşılmıştır. Ayrıca, seramik tipi uçan plakalar için PTZ kaset performansının söz konusu malzemenin basma dayancı, kırılma tokluğu ve hacimsel (bulk) empedans gibi mekanik özelliklerine bağlı olduğu gösterilmiştir.

Anahtar Sözcükler: uçan plaka, yüksek hızlı jet, reaktif kaset, PTZ, seramik

To My Family

ACKNOWLEDGMENTS

First of all, I would like to express my gratitude to my thesis supervisors Prof. Dr. Metin Akkök and Prof. Dr. R. Orhan Yıldırım, for their guidance, advice, criticism, and endless support during my whole graduate studies.

Besides my supervisor, I would like to thank my committee members, Prof. Dr. Ömer Anlağan, Assoc. Prof. Dr. Hüsnü Dal, Prof. Dr. Bilgehan Ögel, and Prof. Dr. S. Kemal İder for their valuable discussion and insights.

I would also like to thank all of my colleagues Kaan Toksoy, Murat Kamberoğlu, and Gamze Sapancı for their valuable discussions and Ege Arkın Dileklioğlu for his support in experimental work. Moreover, I am grateful to Dr. Thomas Hartmann from Numerics GMBH for supplying extra SPEED dongles for my study.

The thesis was funded by a SAYP contract. I also appreciate TÜBİTAK BİDEB for their financial support during my graduate study.

To my wife, without whom, this thesis would not exist.

TABLE OF CONTENTS

LIST OF TABLES

TABLES

LIST OF FIGURES

FIGURES

LIST OF ABBREVIATIONS

AD	Areal Density
AFRP	Aramid Fiber Reinforced Plastic
Al	Aluminum alloy
BISO	Built-in Stan-doff Distance
BMP	Backward Moving Plate or B-plate; front plate in cassette configuration
CE	Chemical Energy
CFRP	Carbon Fiber Reinforced Plastic
DOP	Depth of penetration or residual penetration
EM	Mass Efficiency
ERA	Explosive Reactive Armor
ES	Space Efficiency
FMP	Forward Moving Plate or F-plate; back plate in cassette configuration
GFRP	Glass Fiber Reinforced Plastic
HEL	Hugoniot Elastic Limit
HVRB	History Variable Reactive Burn
KE	Kinetic Energy
LSD	Long Stand-off Distance
PC	Polycarbonate
PE	Polyethylene
PETN	Pentaeritritol tetranitrat
PTZ	Patlayıcı Tepkimeli Zırh
RHA	Rolled homogenous armor (according to MIL-DTL-12560K)
SAYP	Savunma Sanayi için Araştırmacı Yetiştirme Programı
SCJ	Shaped Charge Jet
SOD	Stand-off Distance
SSD	Short Stand-off Distance
St	Steel

LIST OF SYMBOLS

AD_{ERA}	Areal density of ERA cassette or module (g/cm^2)
AD_{REF}	Areal density of reference penetration on RHA (g/cm^2)
AD_{RES}	Areal density of residual penetration on RHA (g/cm^2)
b	Parameter in Umin model (-)
c_b	Necking speed (mm/μs)
D	Detonation velocity of the explosive (mm/μs)
D_{cf}	Crater diameter on the semi-infinite target for a given jet element (mm)
d_j	Diameter of jet segment (mm)
E_M	Mass efficiency (-)
E_S	Space efficiency (-)
g	Normalized gap distance between jet particles (-)
g_0	Empirical parameter for particulated jet penetration (-)
h	Thickness of plate (Equation 2.3)
h_M	Thickness of plate M in Gurney velocity calculations (mm)
h_N	Thickness of plate N in Gurney velocity calculations (mm)
h_{ERAm}	Thickness of the ERA module, including distance to base armor (mm)
h_{BMP}	Thickness of BMP (mm)
h_{EXP}	Thickness of explosive layer (mm)
h_{FMP}	Thickness of FMP (mm)
K	Definition given in Equation 2.3
L	Height of the ERA cassette (mm)
L_1	Hit position on the BMP (mm)
L_2	Hit position on the FMP (mm)
L_j	Length of interacting jet part (Equation 2.1)
L_p	Length of interacting plate part (Equation 2.1)
l_j	Length of the jet segment (mm)
$\dot{m}_j$	Mass flux of jet (Equation 2.2)
$\dot{m}_p$	Mass flux of plate (Equation 2.2)
P	Penetration (mm)
P_{ERA}	Thickness of ERA cassette or module (cm)
P_{REF}	Reference depth of penetration of warhead in RHA (cm)
P_{RES}	Residual depth of penetration in RHA behind ERA (cm)
pos_i	Initial position of the i'th jet particle (mm)
R_t	Target resistance to penetration (Equation 2.11)
R_{tP}	Resistance of target to penetration (kPa)
R_{tR}	Resistance of target to hole growth (kPa)
r_c	Crater radius on flyer plate (mm)

r_{cf}	Crater radius according to Szendrei eqn., $D_{cf}/2$ (mm)
r_j	Radius of the jet segment (mm)
SOD	Stand-off distance to base armor (mm)
SOD_1	Stand-off distance to ERA cassette (mm)
t_{act}	Activation time of the explosive layer (μs)
$t_{arrival}$	Arrival time of jet segment to crater bottom (μs)
t_b	Break-up time (μs)
t_{BMP}	Life span of BMP (μs)
t_c	Hole closure time (μs)
t_e	Interaction time of jet segment and flyer plate (μs)
t_{FMP}	Life span of FMP (μs)
t_{VO}	Virtual origin time (μs)
U_0	Parameter in Umin model (m/s)
U_{min}	Minimum penetration velocity (mm/μs)
U_p	Penetration velocity (mm/μs)
v_j	Axial velocity of jet segment (mm/μs)
V_{CR}	Critical velocity (Equation 2.11)
V_{FP}	Instantaneous velocity of the flyer plate (mm/μs)
V_G	Gurney velocity of the explosive (mm/μs)
V_j	Incident jet velocity (Figure 2.1)
V_p	Flyer plate velocity (Figure 2.1)
V_{pj}	Velocity ratio of plate and jet (Equation 2.3)
V_{PM}	Flyer plate M's final velocity in Gurney calculation (mm/μs)
V_{rel}	Relative velocity (Equation 2.13)
V_t	Deflected jet velocity (Figure 2.1)
Y_j	Yield strength of jet (kPa)

LIST OF SYMBOLS (GREEK LETTERS)

α	Naz's coefficient (-)
α	Actual deflection angle (Figure 2.1)
ΔV	Velocity increment along the jet (mm/μs)
φ	Observed deflection angle (Figure 2.1)
η	Disruptive efficiency (Equation 2.7)
λ	Adjustment parameter for the width of the strip (Equation 2.3)
ρ_{ERA}	Average density of ERA cassette or module (g/cm^3)
ρ_{EXP}	Density of the explosive material (g/cm^3)
ρ_{FP}	Density of the flyer plate material (g/cm^3)
ρ_j	Density of jet particle (g/cm^3)
ρ_p	Density of flyer plate (Equation 2.3)
ρ_{RHA}	Density of RHA (g/cm^3)
ρ_t	Density of the target or base armor (g/cm^3)
τ	Time constant for flyer plate acceleration (-)
τ_b	Break-up time duration (μs)
θ	NATO impact angle on ERA cassette

CHAPTER 1

INTRODUCTION

Explosive Reactive Armor (ERA) is an efficient way of stopping the shaped charge jet (SCJ) which is formed by the initiation of a shaped charge warhead. Understanding the basics of ERA necessitates comprehension of SCJ and its penetration mechanisms.

In this chapter, a brief introduction is given by providing basic information about shape charges and hydrodynamic penetration (see Sections 1.1 and 1.2). Then, the fundamentals of ERA are given in Section 1.3. Next, the literature survey on ERA configurations with alternative materials is given in Section 1.4. The chapter is concluded by the aim of the thesis (Section 1.5).

1.1. Classification of Warhead Types

A warhead is defined as "the specific device or part of an armament system that damages a desired target and renders it incapable of performing its intended function" [1]. Within the context of this definition, these warheads are divided into two diverse categories in which: 1) damage is caused by explosives that accelerate metal or/and produce blast effects, and 2) propellants accelerate metallic penetrators to lethal velocities.

Conventional literature describes the first kind (high-explosive) devices as chemical energy warheads (CE) and the second kind as kinetic energy (KE) penetrators. Moreover, high-explosive warheads can be classified into two categories which are directed energy and omnidirectional warheads (Figure 1.1).

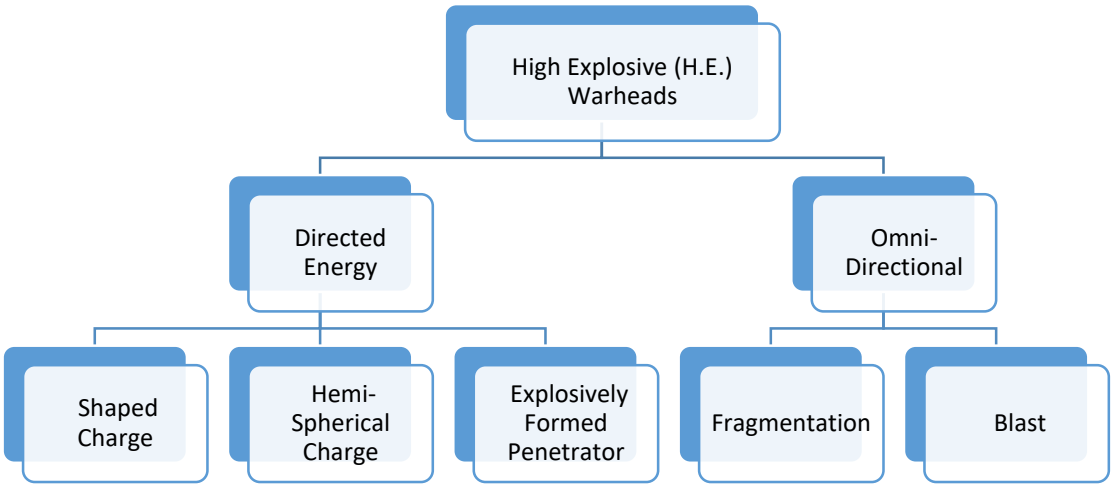

Figure 1.1 Family of high-explosive warheads [1]

Directed energy warheads possess a metal lined cavity and focus the energy of the explosive to form a hypervelocity penetrator. These warheads can also be divided into three groups, namely shaped charge, hemispherical charge, and explosively formed penetrator. A typical shaped charge warhead produces a hypervelocity jet with tip speeds ranging in 7-10 km/s. On the contrary, an explosively formed penetrator produces a slug or fragment of velocity as 2-3 km/s [1].

1.2. Hypervelocity Jet Penetration Mechanics

1.2.1 Ideal Jets and Homogenous Targets

The mechanical strength of jet and target material are overtaken by the strain levels and strain rates induced by the impact of the shaped charge jets. Therefore, the strength effects can be neglected all together [2, 3]. Thus, the penetration process can be assumed as flow of incompressible fluid into another incompressible fluid. At steady state, a stagnation volume is established at the interface of jet and target, and moves at a velocity U into the target. The stagnation pressure, p applies to both sides of this interface. Then, the Bernoulli equation for the incompressible flow of a jet of constant velocity, V_j gives Equations 1.1 and 1.2 [4].

$$p = \frac{1}{2}\rho_j (V_j - U)^2 \tag{1.1}$$

$$p = \frac{1}{2}\rho_t U^2 \tag{1.2}$$

where ρ_j and ρ_t are the densities of the jet and target material. The penetration velocity, U is found by rearranging Equations 1.1 and 1.2:

$$U = \frac{\mathrm{V_j}}{1+\sqrt{\frac{\rho_t}{\rho_j}}} \tag{1.3}$$

The penetration depth, P from the impact of jet of length L is given in Equation 1.4 [4].

$$P = \frac{LU}{V_j - U} = L\sqrt{\rho_j/\rho_t} \tag{1.4}$$

Equations 1.3 and 1.4 can be used to have an approximation of the penetration depth and penetration-time history of an ideal jet impacting a homogeneous target. Based on this, Allison and Vitali [5] introduced the concept of linear velocity gradient jet emerging from a "virtual origin" and obtained penetration of a continuous jet as a function of time. Then, DiPersio and Simon [6] extended this theory by assumption of instantaneous jet breakup and presented explicit formulas for three cases: penetration of continuous jet, penetration of partially continuous and partially particulated jet and penetration of fully particulated jet. This work is revisited by Held [7], and penetration formulas as a function of time are presented. Moreover, he calculated penetration cutoff velocities by plotting hydrodynamic predictions and experimental results on the same graph. The predictions of ideal penetration depths as a function of limiting residual jet velocity, V_r for three regimes is given in Equations 1.5-1.7.

1. Continuous jet:

$$P\ (\mathrm{V_r}) = Z_0 \left(\left(\frac{V_0}{V_r}\right)^{\frac{1}{\gamma}} - 1 \right) \tag{1.5}$$

2. Partially continuous, partially particulated jet:

$$P\ (\mathrm{V_r}) = \left[\frac{\left[(1+\gamma)(V_0 t_b)^{\frac{1}{1+\gamma}} Z_0\ ^{\gamma(1+\gamma)} - V_r t_b\right]}{\gamma}\right] \tag{1.6}$$

3. Long standoff, fully particulated jet:

$$P\ (\mathrm{V_r}) = \ (V_0 - V_r) t_b/\gamma \tag{1.7}$$

where, Z_0 is the standoff distance from the virtual origin, V_0 is the jet tip velocity, t_b is the jet breakup time, and γ is the square root ratio of density of target and jet material.

Ideal penetration curves for the penetration of shaped charge jet on RHA for a jet tip velocity of V_0=8.5 mm/μs and jet breakup time t_b=130 μs are plotted in Figure 1.2, in which an experimental penetration versus standoff curve for the warhead is also included [1]. It can be concluded that, the penetration cutoff velocity increases with the standoff distance, as deviations from the ideal jet come into play.

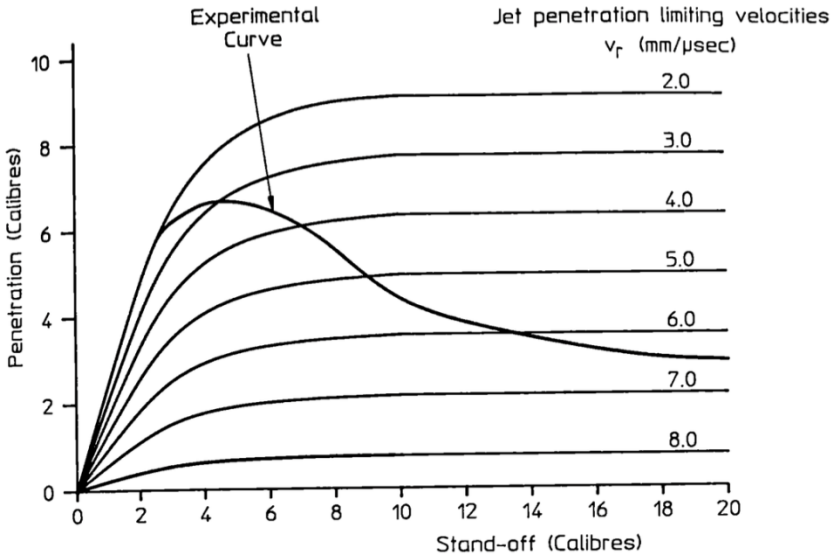

Figure 1.2 Ideal penetration standoff curves as a function limiting velocity [1]

1.2.2 Non-ideal Jets and Homogenous Targets

The differences of ideal jet concept and practical jets are as follows [1]:

- Misalignments from jet velocity vectors from jet axis
- Nonlinearity of the jet velocity profile
- Time dependence of breakup as a function of position in the jet

Practical jets may possess particles with tumbling and lateral (drift) motions away from the mean longitudinal axis of the jet. Figure 1.3 gives a simple representation of this condition, compared with the straight, well-ordered particulated jet.

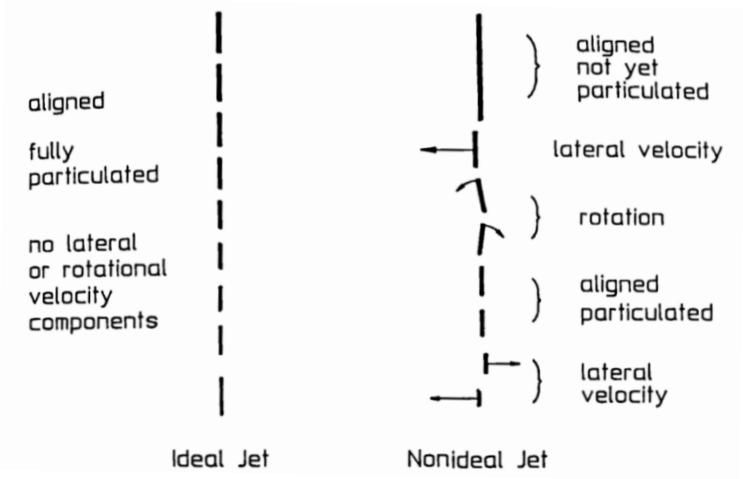

Figure 1.3 Qualitative comparison of ideal and non-ideal jets [1]

1.3. Fundamentals of Reactive Armor

The penetration capability of SCJs increased a lot since the Second World War, rendering the protection of armored vehicles impossible by classical means. There is a need for lighter and more efficient way of stopping those jets. One way of achieving this goal is to use reactive armor. It is first proposed by Held [8] in the western world and as described by Rototaev in the Warsaw Pact [9]. In USA, similar ideas are known however in their studies, the emphasis is on the disruption of the jet by the explosive (which is termed as explosive pill armor) while the emphasis in this thesis is on the disruption by the moving metal plates. In literature, definition of ERA is published in references [10, 11, 12, 13]. Additional references dealing directly with

ERA are [14, 15, 16, 17, 18, 19, 20, 21, 22] and indirectly, with interaction of jets with moving plates are given in [23, 24, 25, 26, 27, 28].

The schematic view of the interaction of shaped charge jet with ERA cassette is given in Figure 1.4 [29] in which basic features of the interaction such as key hole and the disrupted jet are depicted.

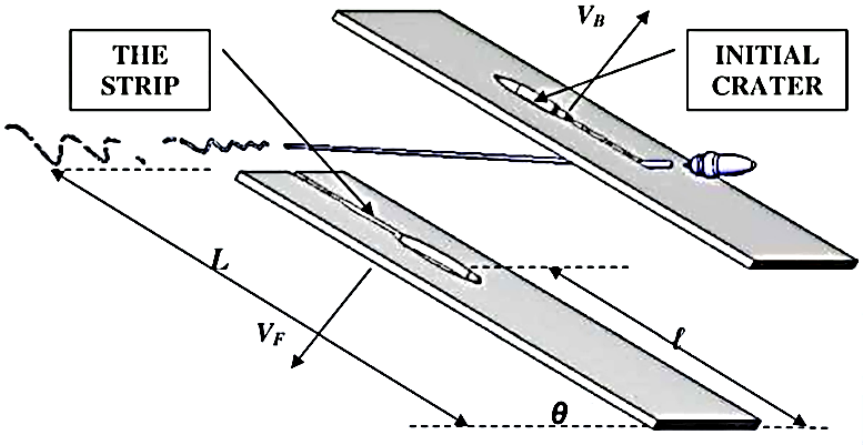

Figure 1.4 Schematic view of an ERA cassette interaction with shaped charge jet [29]

The efficiency of ERA is based on three different mechanisms [30]:

1. Dynamic Plate Thickness

The high explosive layer will detonate if a SCJ perforates BMP and hits the explosive charge. The plates of the cassette will be accelerated by the detonation pressure and fly in opposite directions with velocities corresponding to the mass ratio of explosive and plates [31]. Oblique orientation of the plates results in new plate material being fed into the flight path of SCJ. Thus, “dynamic plate thickness” constitutes one working mechanism of reactive armor.

2. Deflection

Some portion of the kinetic energy of the SCJ will be consumed during the perforation process of the plates. During the interaction, momentum transfer in transverse direction to SCJ flight path will deflect or even disrupt the jet. A deflected

or disrupted jet does not hit the same crater hole, so that the penetration performance of the SCJ will be drastically reduced.

3. Shock load and explosive products

Detonation shockwave and the expanding products of detonation can also introduce transverse movements to the SCJ if they are streaming out of the holes in the flyer plates, mostly not symmetrically formed.

Radiographic image of SCJ passing through ERA cassette reveals that after the interaction; SCJ consists of three parts (Figure 1.5) a relatively short, fairly intact and little disturbed leading part (the precursor) (A), damaged main part of the jet (B) and undamaged tail section of the jet (C) which comes through ERA cassette without any interaction with flyer plates.

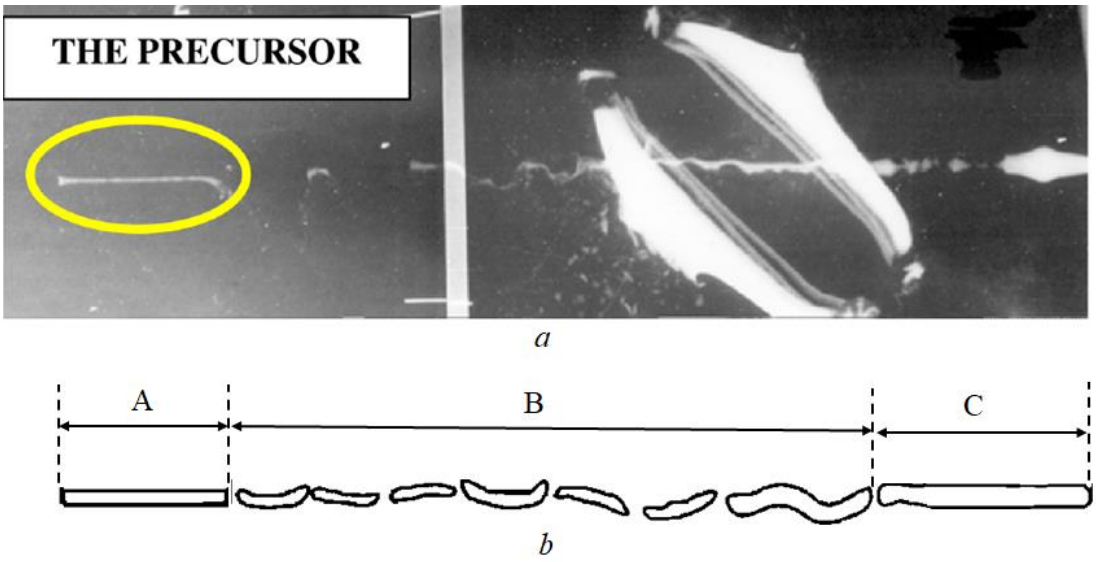

Figure 1.5 Structure of SCJ after passing reactive cassette: (a) Flash X-ray [29], (b) schematic view [32]

Increasing the efficiency of the reactive cassette requires solving the following tasks: 1) reducing the length of the precursor; 2) increasing the extent of damage to the main part of the SCJ; 3) avoiding passing of the tail section of SCJ without exposure to flying plates.

Solving these problems requires an understanding of the physical processes occurring during the interaction of the SCJ with ERA flyer plates. The main physical processes that determine the efficiency of ERA protection capacity should include: 1) formation of holes in the plates of ERA cassettes when they contact with SCJ; 2) initiation of detonation in the explosive charge; 3) explosively acceleration of plates; 4) the interaction of moving plates with the SCJ.

Within the context of design activities; these particular issues can be dealt by increasing the physical understanding of the followings:

- Effective opening of cassette
- Interaction time of cassette
- Mass flux and momentum transfer methods
- Material effects

1.3.1 Weight and Space Efficiencies

The ballistic protection performance of explosive reactive armor (ERA) is measured by its effectiveness. Generally speaking, it is obvious that the higher the effectiveness, the better. Depending on the application, the need arises for a low-weight ERA in some applications and for a small volume ERA for others. For some applications a small amount of explosive is requested whereas for other cases collateral damage is what counts.

It is clear that many definitions can be used to define the effectiveness. Within the context of this chapter, the following definitions will be used for measuring the effectiveness of ERA cassettes, based on space and weight needed to stop the SCJ. Equations 1.8 and 1.9 define the space (E_S) and mass (E_M) efficiencies of ERA cassettes.

$$E_S = \frac{P_{REF}}{P_{ERA}+P_{RES}} \tag{1.8}$$

$$E_M = \frac{AD_{REF}}{AD_{ERA}+AD_{RES}} \quad (1.9)$$

In these equations $AD_{REF} = P_{REF} * \rho_{RHA}$, $AD_{ERA} = P_{ERA} * \rho_{ERA}$ and $AD_{RES} = P_{RES} * \rho_{RHA}$ are the areal densities of reference RHA block, ERA module and residual witness penetration respectively. The definitions are given in Figure 1.6.

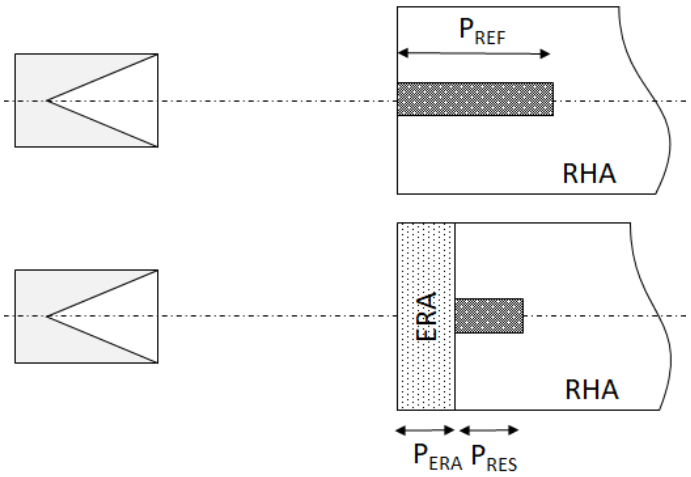

Figure 1.6 Illustration of variables for space and mass efficiencies

1.4. Test Results with Lightweight Materials from Literature

In the pioneer work by Kaufmann et al [33], ballistic protection efficiencies of ERA cassettes with lightweight plates are compared with classical 3/3/3 steel cassette configuration[1] (made of "S 235 JR" steel according to DIN EN 10025-2). Plates of steel, aluminum, polycarbonate (PC), polyethylene (PE) and glass fiber reinforced plastic (GFRP) (Table 1.1) are used with the same areal densities.

[1] 3/3/3 refers to a cassette configuration with 3 mm steel + 3 mm explosive + 3 mm steel.

Table 1.1 Materials test as flyer plates [33]

Material	**Abbreviation**	**Density [g/cm^3]**	**Thickness of Plate [mm]**	**Mass of Plate [g]**
Steel	St	7.83	3	705
Aluminum	Al	2.70	9	729
Polycarbonate	PC	1.20	20	720
Polyethylene	PE	0.95	25	712
Glass fibre reinforced plastic	GFRP	1.94	12	698

They used a shaped charge warhead with 50 mm cone diameter; for which, 381±10 mm depth of penetration is achieved in stacked RHA at 250 mm stand-off distance and 358±15 mm depth of penetration at 500 mm stand-off distance. The explosive layer is 3 mm Detasheet 1000 with 6750 m/s velocity of detonation and 1950 m/s gurney constant. The schematic view of experimental setup is given in Figure 1.7. The same experimental setup is employed by this research group in all follow-up works.

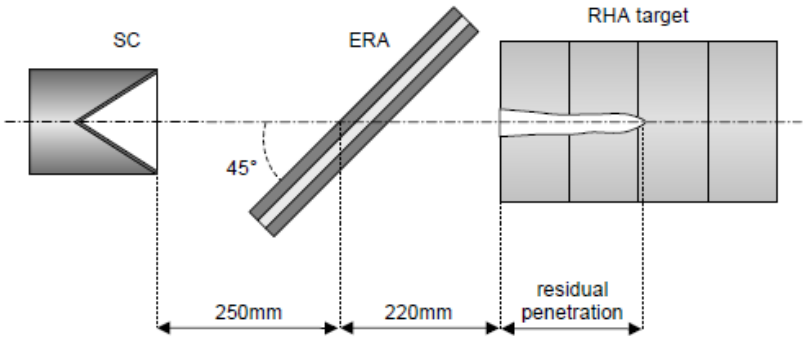

Figure 1.7 Schematic view of the experimental setup [33]

The results of the performed tests are given in Figure 1.8 in which ballistic protection efficiencies of constructed cassettes are given in terms of weighted RHA equivalency (RHA_{eq}) of the configuration, which is given by Equation 1.10.

$$RHA_{eq} = \frac{P_{REF} - P_{RES}}{P_{REF}} \tag{1.10}$$

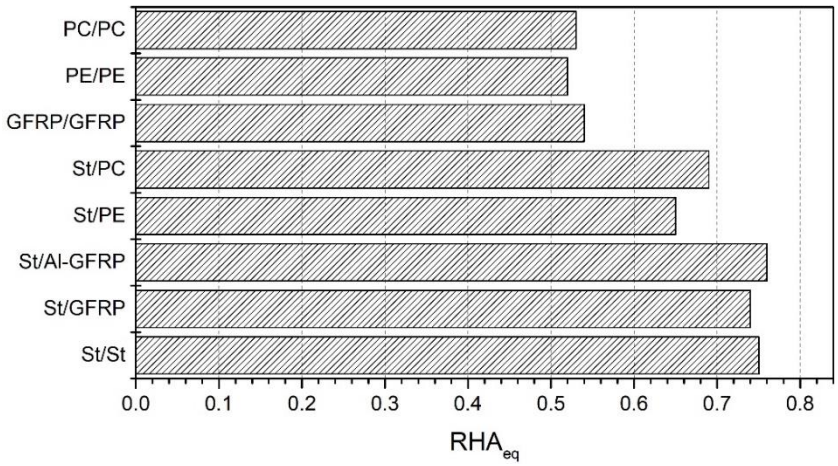

Figure 1.8 RHA equivalencies for constructed cassettes [33]

It is found that combined application of steel as the BMP and composite (GFRP) as the FMP leads to a protection level which is very close to the one of the symmetric steel arrangement. Symmetric GFRP, PE and PC cassettes revealed higher residual penetrations than steel cassettes, which means lower performance.

In a follow up work by Bianchi et al [34]; effect of using ceramic, fiber reinforced plastics and aluminum as flyer plates is addressed. They constructed cassettes with the same areal densities and tested symmetric and asymmetric configurations using the same test setup depicted in Figure 1.7. The mechanical properties of the tested plates are given in Table 1.2. The explosive material is PETN based.

Mass efficiency (EM) results of symmetric cassettes reveals that (Figure 1.9) cassettes constructed with alumina yield better results compared to steel cassettes whereas aluminum has lower efficiency and CFRP provides half of the efficiency of steel cassette (Steel CrNi).

Table 1.2 Materials tested as flyer plates [34][2]

Material	**Abbreviation**	**Density [g/cm^3]**	**Y_0 [MPa]**	**Thickness [mm]**	**Hardness [HV]**
Steel CrNi	St	7.81	360	3.0	230
Steel 235	St 235	7.85	235	3.0	120
Aluminum	Al	2.70	480	8.0	145
Glass fibre reinforced plastic	GFRP	2.50	1500*	12.0	40 Barcol
Carbon fibre reinforced plastic	CFRP	1.50	2000*	15.0	55 Barcol
Aramid fibre reinforced plastic	AFRP	1.40	2900*	18.0	45 Barcol
Alumina 99.7%	Al_2O_3 99%	3.90	2900**	5.8	1650
Alumina 98%	Al_2O_3 98%	3.86	2200**	6.1	1400
Alumina 96%	Al_2O_3 96%	3.80	1900**	5.8	1400
Alumina 90%	Al_2O_3 90%	3.61	1700**	6.5	1150
Silicon carbide	SiC	3.25	3000**	7.3	2200

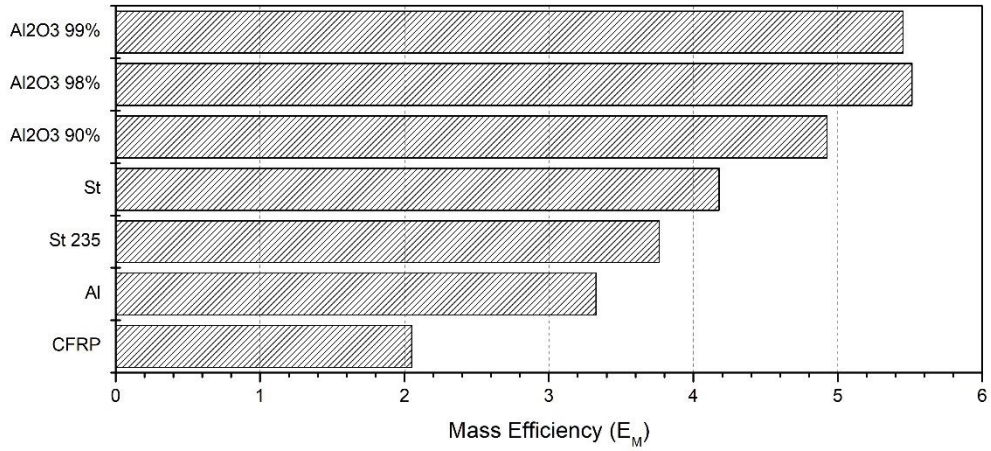

Figure 1.9 Mass efficiency values for symmetric cassettes [34]

E_M values for asymmetric ERA cassettes for which front plate or back plate is varied and the other plate is kept as steel (steel CrNi) are given in Figure 1.10 and Figure 1.11.

[2] * corresponds to tensile strength, ** corresponds to compressive strength, otherwise it is yield strength

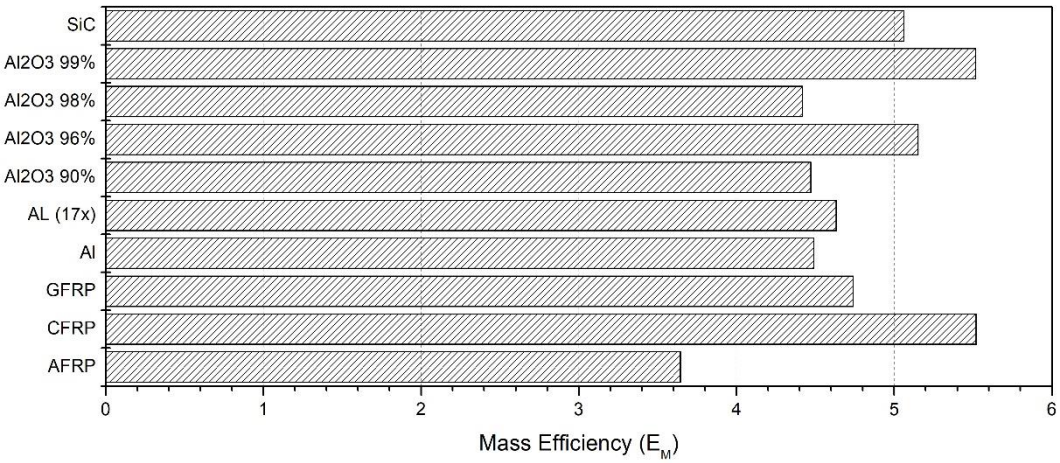

Figure 1.10 Mass efficiency values for asymmetric cassettes (BMP is varied, FMP is kept as steel) [34]

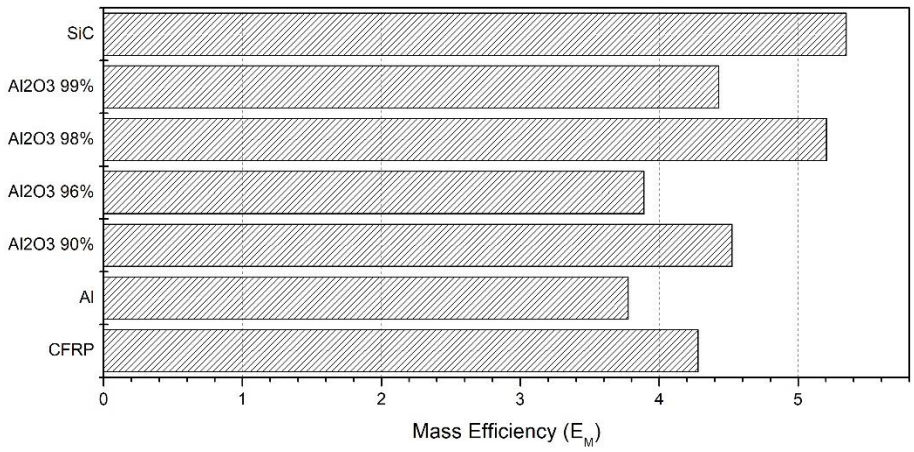

Figure 1.11 Mass efficiency values for asymmetric cassettes (FMP is varied, BMP is kept as steel) [34]

From Figure 1.10 it is seen that CFRP, alumina (99% and 96%) and SiC as front plate yield better efficiency than steel, whereas alumina (98% and 90%), aluminum alloys and GFRP reveal similar results to steel. Moreover, results for asymmetric cassettes with varied back plate assume better results for SiC and alumina (98%) flyer plates (Figure 1.11). The general trend is that harder inert plates lead to higher efficiencies.

Based on these results, other combinations of materials (mainly ceramics) are tested (Figure 1.12).

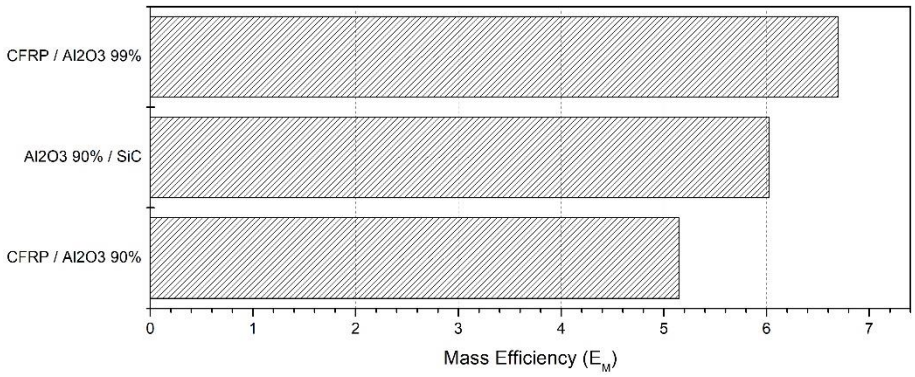

Figure 1.12 Mass efficiency for non-metallic cassettes [34]

The results depicted in Figure 1.12 suggest that there is a significant increase in ERA efficiency. For the same weight (or areal density), an ERA based on ceramics almost doubles the mass efficiency with respect to steel cassettes.

In another follow up work by Koch et al [35], ballistics protection efficiencies of both steel and alumina cassettes are compared by a number of tests, in which, plate thicknesses and explosive thicknesses are varied. The areal densities of constructed cassettes are in the range of 2.5 – 14.0 g/cm^2. The mechanical properties of the flyer plates are given in Table 1.3.

Table 1.3 Materials tested as flyer plates [35]

Material	**Density [g/cm^3]**	**Hardness [HV]**	**Tensile Strength [MPa]**	**Compressive Strength [MPa]**	**Yield Strength [MPa]**	**Thickness [mm]**	**Weight [g]**
Steel 235	7.85	120	400	400	235	1.0 3.0 6.0	240 700 1450
Steel 1.4301	7.90	230	600	600	360	1.0 3.0 6.0	240 700 1450
Armox 600	7.85	630	2000	2000	1500	6.0	1450
Alumina 99.5%	3.90	1650	280	2900	-	2.9 5.9 11.8	350 700 1400

The tests are performed according to the test setup depicted in Figure 1.7. It is seen that for steel cassettes, light rear plates reveal better results whereas for alumina, higher mass of the cassette yields higher EM compared to lower mass cassettes. Mass efficiency versus space efficiency results are given in Figure 1.13.

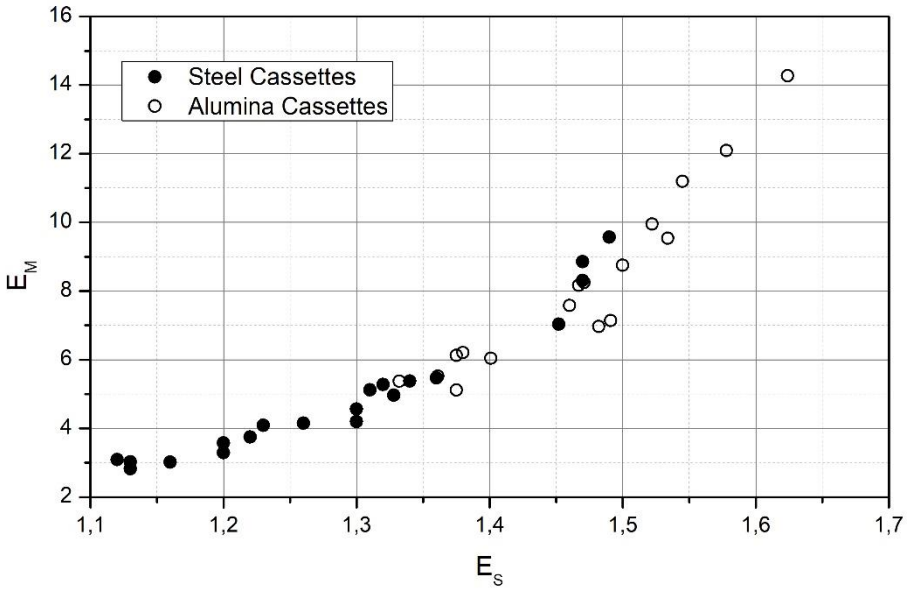

Figure 1.13 Mass (E_M) versus space efficiency (E_S) results of tests [35]

From Figure 1.13 it can be seen that alumina cassettes in general, provide better results in both mass and space efficiency. This can also be observed in the plot of E_M versus E_S for ERAs constructed with heaviest plates and 3 mm explosive sheets.

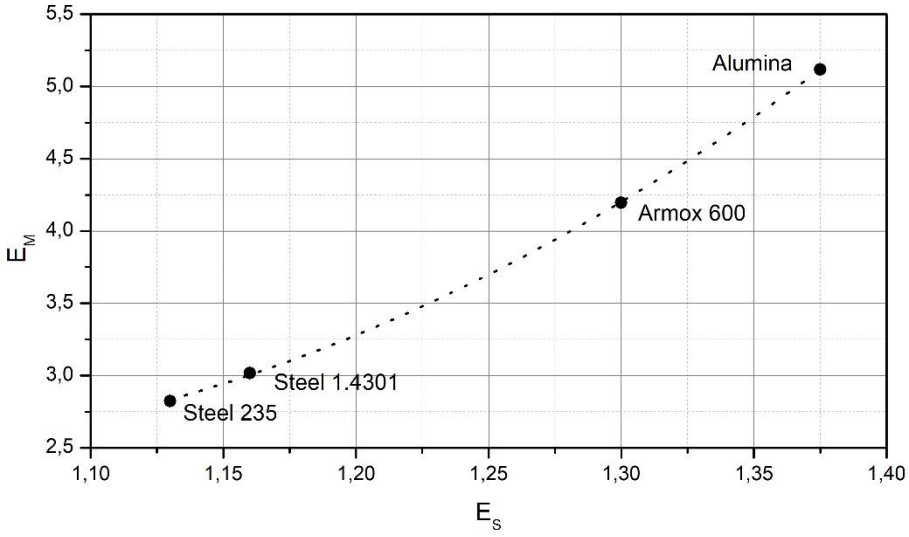

Figure 1.14 Mass (E_M) versus space efficiency (E_S) for ERAs with heavy plates (1400-1450 g) and 3 mm explosive sheets [35]

In the follow up work by Mayseless et al [36], the effect of varying space at the back of the ERA configuration is examined. The backing space is taken as 220 mm or 620 mm for each configuration (Figure 1.15). The materials that are tested are given in Table 1.4.

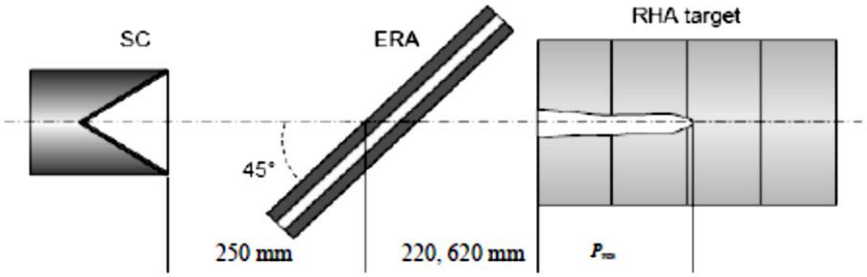

Figure 1.15 Experimental setup for the tests [36]

Table 1.4 Materials tested as flyer plates [36]

Material	Density [g/cm^3]	Hardness [HV]	Tensile strength [MPa]	Compressive strength [MPa]	Thickness [mm]
Steel 1.4301	7.90	230	600	600	3.0
Alumina 99.7%	3.99	1700	300	3000	5.9
PE HD	0.94	D64	30	20	24
Cevodur UTR (GFRP)	1.83	-	70	250	12

The resulting residual penetrations for each configuration for long stand-off distance (LSD) and short stand-off distance (SSD) are presented in Figure 1.16.

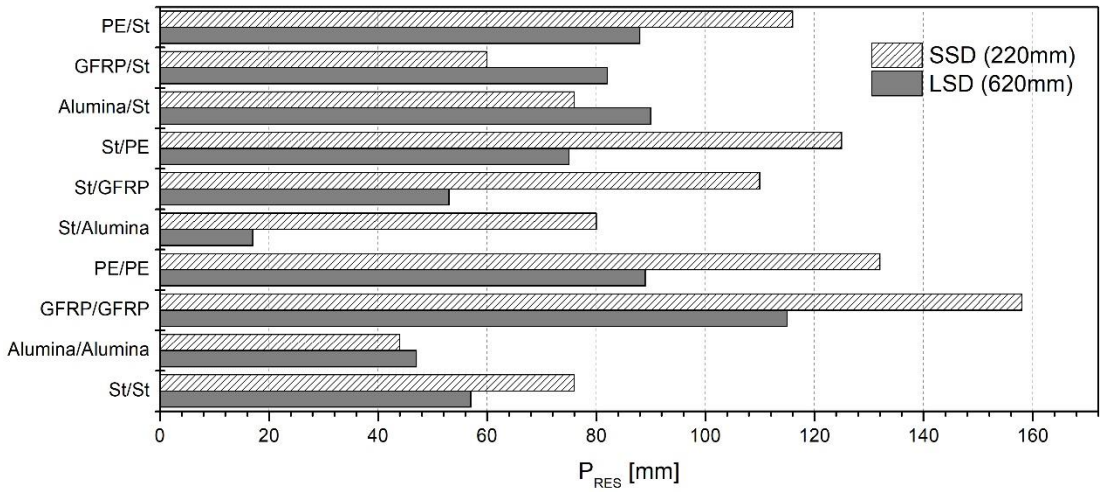

Figure 1.16 Residual penetrations (P_{RES}) for ERA cassettes for two stand-off (backing) distances [36]

From Figure 1.16 it is seen that the ballistic protection performance of each configuration changes with back space distance (being LSD or SSD). The residual penetration for symmetric cassettes revealed generally better results for LSD compared to SSD except for alumina.

In the tests results for the symmetric ceramic cassettes, the depths of penetrations are much smaller compared to the steel cassette for both standoffs. Changing the Alumina type from 99.7% to 99.5% (tests from the previous study [35]) increases residual penetration by about 30% for the SSD configuration.

Replacing the steel front plate by GFRP decreases residual penetration in the case of SSD. Residual penetrations of non-steel front plate and steel back plate cassettes are increased for cases of LSD. The ceramic front plate produces deeper penetration compared to the symmetric ceramic cassette. Comparing it to the symmetric steel cassette it is found that at SSD the residual penetration is the same but at the LSD configuration the residual penetration increases.

The cassettes with the PE front plate produced relatively deep residual penetrations, although better than the symmetric PE cassettes.

Replacing the steel back plate by ceramic gave the best result at LSD. At SSD the residual penetration is about the same as for the symmetric steel cassette, but higher compared to the symmetric ceramic cassette.

Overall, it seems that for cassettes placed far from the main armor, ERA composed of non-metallic back plate is preferred, while for cassettes placed close to the main armor it is recommended to use non-metallic front plate. Replacing the two steel plates by non-metallic plates produces good results in both test configurations only if the material is high strength ceramic.

It is interesting to note that, their study also revealed the relation between the residual penetration and the precursor[3] length that escapes the ERA cassette. The length of the precursor jet is measured from the X-Ray flashes (Figure 1.17 and Figure 1.18). It is seen that measured lengths are in agreement with the depth of penetration results.

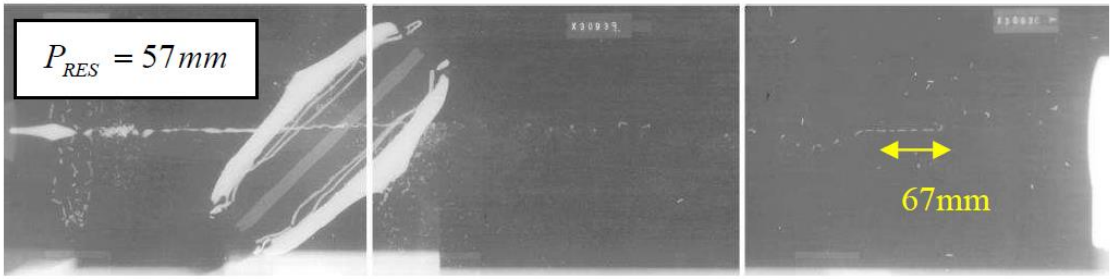

Figure 1.17 X-Ray image of jet after penetration of 3St/3/3St cassette at LSD [36]

[3] Relatively faster tip portion of the jet that escapes ERA cassette before the flyer plates take effect

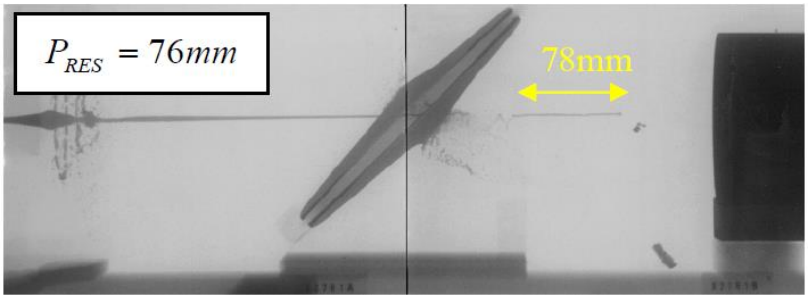

Figure 1.18 X-Ray image of jet after penetration of 3St/3/3St cassette at SSD [36]

It is stated that the jet behind the precursor has almost no contribution to the DOP in the case of the LSD, as the disruption is fully developed. Therefore, a good correlation is expected between the residual penetration and the precursor length.

Hazell et al [37] investigated the penetration of shaped charge jets into reactive cassettes with brittle materials. They used symmetric ERA design and ø89mm shaped charge warheads (Figure 1.19) to assess the performance of armor configurations with flyer plates constructed from alumina, silicon carbide, borosilicate glass, and steel (Table 1.5). Two different thicknesses are used for each material with areal densities equivalent to 2 and 4 mm steel plates.

In particular, it is noted that the performance of silicon carbide and alumina flyer plates Table 1.5 are comparable to steel (Figure 1.20). Furthermore, there is evidence that increasing the mass of the explosive material between ceramic layers improves the performance of the armor thereby providing room for optimization of a brittle material ERA system (Figure 1.21).

The patent of Mayseless [38] specifies application of flyer plates with controlled fragmentation points for reduced collateral damage. Patent by Hazell [39] follows with the ceramics case, in which, the fragmentation is uncontrolled but it also renders the fragments harmless.

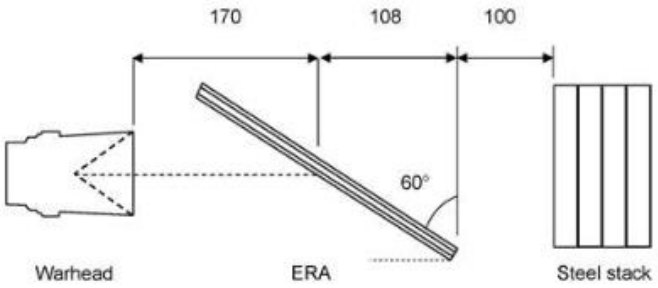

Figure 1.19 Test setup used in the study [37]

Table 1.5 Materials tested as flyer plates [37]

Material	**Grade**	**Density [g/cm^3]**	**Thickness [mm]**	**Areal Density [kg/m^2]**
Steel	Grade S275	7.800	2.0/4.0	15.6/31.2
Alumina	Sintox FA	3.724	4.0/8.0	14.9/29.8
Borosilicate glass	Borofloat	2.200	7.5/15.0	16.7/33.5
Silicon carbide	PS-5000	3.147	4.9/9.8	15.4/30.9

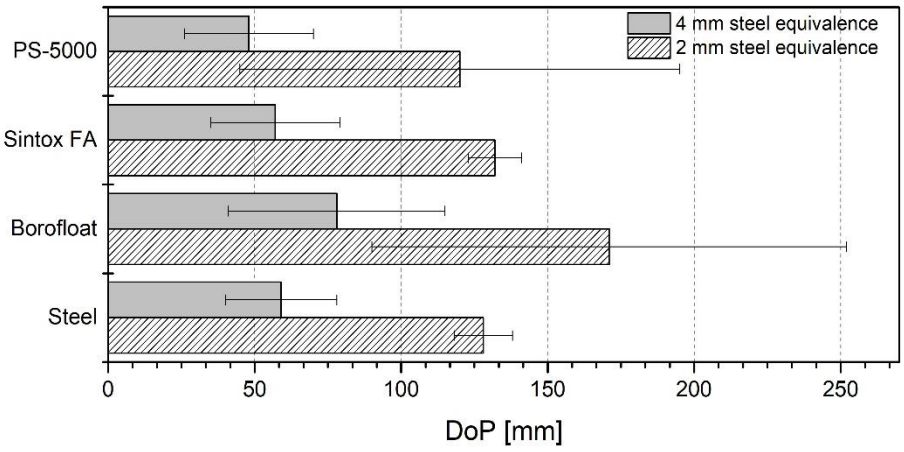

Figure 1.20 Performance of ERA systems for 2 mm steel equivalence and 4 mm steel equivalence [37]

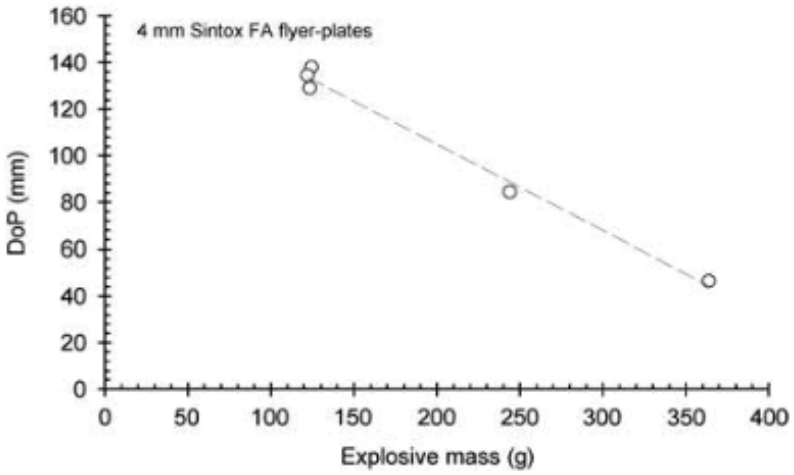

Figure 1.21 The impact of PBX mass on the performance of the ERA [37]

Liden et al [40] investigated the performance of cassettes made of alumina, silicon carbide, boron carbide and glass fibre reinforced plastic and made comparisons with simulation results. The areal density of the ERA cassettes is kept constant for all tests. They used PETN based explosive layer and performed tests with 84 mm cone diameter shaped charge. Test configurations and results are given in Table 1.6.

Table 1.6 Cassette configurations and test results [40]

Front Plate		**Back Plate**		**Explosive Thickness [mm]**	**P_{RES} [mm]**
Material	**Thickness [mm]**	**Material**	**Thickness [mm]**		
B4C	9.4	B4C	9.4	3.0	53
B4C	9.4	Domex 500	3.0	3.0	27
Domex 500	3.0	B4C	9.4	3.0	43
SiC	7.3	SiC	7.3	3.0	38
SiC	7.3	Domex 500	3.0	3.0	34
Al2O3 99.5%	6.0	Al2O3 99.5%	6.0	3.0	44
Al2O3 99.5%	6.0	Domex 500	3.0	3.0	40
GFRP	12.0	GFRP	12.0	3.0	109
Domex 500	3.0	Domex 500	3.0	3.0	30

From Table 1.6, it is seen that cassette with B4C and SiC front plate revealed similar result with regard to symmetric steel configuration, whereas, other ceramic or composite cassettes yield higher residual penetrations. Their study also showed that, using JH2 ceramic model for the simulations results in similar disturbance of the SCJ and plate response compared with X-ray images.

The experimental findings from the literature are itemized below:

- It is possible to reduce unwanted effects of ERA cassettes by using composite or ceramic flyer plates.
- Symmetric cassettes with GFRP, PE and PC have lower EM values, which is attributed to slower acceleration of plates due to their low sound speeds and higher thickness by the researchers.
- Ballistic protection efficiency correlates well with material properties like hardness and yield strength. For instance, increasing both yields higher efficiencies. The reason for higher efficiencies with higher strength comes from the fact that the plates will possess smaller crater diameters. Hence, jet particles will quickly get in touch with the plate.
- Using ceramics as flyer plates generally increases efficiencies.
- Most of the residual penetration in main target is due to the precursor, which is flying across the ERA before detonating explosive sheets imparts a significant velocity to the flyer plates.
- Increasing thickness of the explosive layer increases EM regardless of the weight of flyer plates. This is achieved by sooner re-contact of the crater edge with the SCJ.
- For steel, higher protection efficiencies are achieved with light FMP. On the other hand, for alumina, lower areal density cassettes reach lower EM values compared to higher areal density configurations.
- The space between the ERA cassette and the main armor is a significant design parameter because it may change the characteristics of the event completely. The longer distance travelled by the disturbed jet causes greater spread of its particles. Thus, the penetration is decreased.
- For larger back space distances, non-metallic back plates are preferred whereas for smaller back space distances, non-metallic front plates are preferred.
- Non-metallic front plates of thick and low density materials like PE or GFRP may contribute to the disruption process.

Many aspects of the lightweight and brittle materials are examined in the literature, and it is shown that effective or even better results can be achieved with non-metallic flyer plates, compared to steel flyer plates.

1.5. Aim of the Thesis

As outlined in the literature review, it is seen that a reactive cassette can be constructed by using non-metallic materials. Needless to say, such a cassette will render an ERA configuration with reduced collateral damage. The main targets for the reduction of shrapnel harm to the surrounding can be stated as:

- Low density
- Low velocity
- High aerodynamic drag

It can be predicted that plates manufactured by processing fine particles will turn back to particulated state easily with the application of explosive loading. Preliminary studies of the pioneers of these configurations confirm that these particles are relatively harmless compared to metallic cassettes with the advantage that the particulation takes place after the disruptive effect of the cassette has taken place. Therefore, a study should be sought in order to understand the basic mechanisms of interaction of lightweight plates and hypervelocity jets and underline the effects of main design parameters to construct a harmless (or less harmful) ERA without losing significant protection efficiency.

Literature review suggests ERA cassettes made of ceramics yield performances comparable or even preferable with respect to traditional steel cassettes.

The aim of this thesis is to investigate the ballistic protection performance of ERA cassettes made from non-metallic materials, in particular ceramics and glass. In the first part of the thesis, types of interaction between the shaped charge jet and hypervelocity plate and conditions for occurrence are proposed, and also their relevance is compared with simulation studies. Then, an engineering model for the calculation of the residual depth of penetration behind ERA is suggested. The model

calculates the precursor part and the tail section of a SCJ that escapes the ERA cassette without interaction.

In the experimental part, front and rear plates of the steel ERA cassette are changed with alternative materials to observe their effects. Then, best performing materials are combined in a non-metallic cassette and the results are compared with that of a steel cassette. The areal density is kept similar for all ERA configurations. Hydrocode numerical analyses are performed for comparison with the test results. Finally, best performing materials as front and back plates are selected and necessary material properties for a better performance are shown.

CHAPTER 2

ANALYTICAL MODELS FOR INTERACTION

It is crucial to understand the mechanics of interaction of flyer plate with hypervelocity jet for design of efficient flyer plates. Therefore, a literature survey is carried out for interaction models to be used. In this chapter, interaction models from literature and their comparison are presented. Then, necessary conditions for efficient flyer plates are proposed with complementary simulation study.

2.1. Mass Flux Model

In order to define the deflection of jet by the flyer plate, Mayseless et al. [41] considered the implication of mass and momentum conservation laws applied to the interaction of the jet with the moving plates of a reactive element. It is assumed that flyer plates remain planar and move with a velocity V_p normal to its original orientation (Figure 2.1).

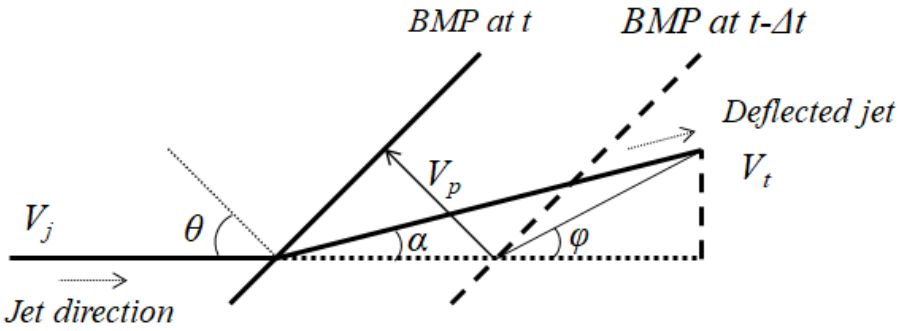

Figure 2.1. Jet deflection for BMP [41]

The plates move in opposite directions. The plate on the front side of the cassette moves in opposite direction to the jet and thus, it is named as backward-moving plate

or BMP. The other plate on the back side of the cassette moves in the direction of the jet and is named as the forward moving plate or FMP. The ratio of plate and jet length that come into interaction is given in Equation 2.1:

$$\frac{L_j}{L_p} = \frac{V_j}{V_p}\frac{1}{\tan\theta} \pm \frac{1}{sin\theta} \tag{2.1}$$

where + sign refers to BMP and – sign refers to FMP. θ is the NATO angle of impact, V_j is the local jet velocity. L_j and L_p are lengths of interacting jet and plate parts. The mass-flux ratio (Equation 2.2) is obtained by comparing the mass of the jet segment and plate strip that interact in unit time:

$$\frac{\dot{m}_J}{\dot{m}_p} = \frac{1}{K}\left(\frac{1}{V_{pj}}\frac{1}{\tan\theta} \pm \frac{1}{sin\theta}\right) \tag{2.2}$$

$$K = \left(\frac{\rho_p}{\rho_j}\right)\left(\frac{4\lambda h}{\pi d_j}\right); \qquad V_{pj} = V_p/V_j \tag{2.3}$$

where + sign refers to BMP and – sign refers to FMP. ρ is mass density, d_j is diameter of jet, h is the plate thickness. λ is a factor of the order one, that can be used to adjust the width of the strip that interact with the jet if it is larger than the jet diameter, or if required, to add plate's strength effects to the interaction process.

Mayseless et al showed that, when $\dot{m}_p < \dot{m}_J$, a stationary interaction between flyer plate and jet is possible. When $\dot{m}_p > \dot{m}_J$, a stationary interaction is impossible, which means a non-steady-state interaction is happening. In other words, when jet mass-flux is dominant, the jet penetrates the plate, the interaction being stable and the jet is deflected. On the contrary, when plate mass-flux is dominant, the plate penetrates the jet, leading to an unstable interaction and jet scattering.

2.1.1 Deflection Angle

Mayseless [41] assumed fully plastic interaction of jet segment with plate slit and provided Equation 2.4 for the deflection angle of the jet velocity vector, φ from momentum transfer.

$$tan\phi = \pm\left(\frac{1}{V_{pj}}\frac{1}{Ksin\theta}\left(\frac{1}{V_{pj}}\frac{1}{tan\theta} \pm \frac{1}{sin\theta}\right) \mp \frac{1}{tan\theta}\right)^{-1} \quad (2.4)$$

where upper signs refer to BMP and lower signs refer to FMP.

From Equation 2.4, Equation 2.5 for the calculation of deflection angle of the jet, α can be derived.

$$tan\alpha = \frac{\frac{1}{V_{pj}}\tan\phi}{\frac{1}{V_{pj}} \pm \frac{1}{cos\theta}} \quad (2.5)$$

where upper signs refer to BMP and lower signs refer to FMP.

Held [42] presented a simpler equation for jet deflection, in which, ratio of momenta of plate and jet parts in interaction are used to calculate the deflection angle:

$$tan\alpha = \frac{4h\rho_p V_p^2 \tan\theta}{\pi d_j \rho_j V_j^2} \quad (2.6)$$

2.1.2 Disruption Efficiency

Mayseless [43] postulated an efficiency description for measuring the disruptive power of a flyer plate against SCJ. The so called "disruptive efficiency" is given in Equation 2.7 is simply inverse of Equation 2.2:

$$\eta = \frac{\dot{m}_p}{\dot{m}_j} = K\left[\frac{V_{pj}sin\theta}{cos\theta \pm V_{pj}}\right] \quad (2.7)$$

When the efficiency of BMP is considered, the limiting value of η is $Ksin\,\theta$, as the plate velocity is increased. BMP maintains contact with the SCJ, unless the edges of the cassette are reached. On the other hand, FMP may lose contact with the jet, if it moves faster than the jet. Therefore, limiting normalized velocity of FMP can be found from Equation 2.8.

$$V_{pj} = cos\theta \quad (2.8)$$

Moreover, by assuming an efficiency value for Equation 2.7, the lower limit of the normalized FMP velocity can be found. Therefore:

$$cos\theta > V_{pj} > \frac{cos\theta}{Ksin\theta/\eta+1} \tag{2.9}$$

2.2. Modes of Interaction

Literature review presented in Section 2.1 suggests that BMP mainly deflects the jet and FMP is responsible for the disruption of the jet. Therefore, special emphasis should be given to the interaction of the jet with FMP for efficient design of reactive cassette. In this section, work related to define the mode of interaction of the FMP with hypervelocity jet is presented. This part is original work within context of this thesis.

Interaction of forward moving plate and a jet segment is depicted in Figure 2.2 along with decompositions of the plate velocity, where jet velocity is V_j, flyer plate velocity is V_p and velocity of interaction point on plate is $V_p/cos\theta$.

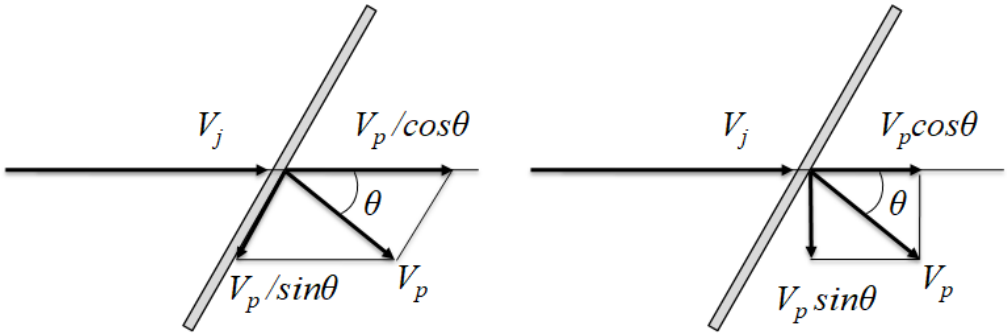

a. relative velocity of jet and contact point on the plate
(Phase velocity $=V_j - V_p/cos\theta$)

b. relative velocity of particles
($V_{rel} = V_j - V_p cos\theta$)

Figure 2.2 Jet and plate velocities and velocity decomposition for FMP

From Figure 2.2, it can be seen that if the velocity of the interaction point is higher than the velocity of the jet, the plate is moving too fast with respect to jet. Therefore, there will be no interaction if the following condition is satisfied [43]:

$$\frac{V_p}{cos\theta} \geq V_j \tag{2.10}$$

It can be assumed that at relatively low velocities, hydrodynamic penetration equation with strengths (according to Alekseevski-Tate equation [44, 4]) can be employed. However, there will be a critical velocity, V_{CR}, below which penetration will not occur. This velocity can be calculated by equating penetration velocity, U_p to zero in Alekseevski-Tate equation.

$$V_{CR} = \sqrt{\frac{2(R_t - Y_j)}{\rho_j}} \tag{2.11}$$

Therefore, jet will not penetrate the flyer plate if this critical velocity is greater than the phase velocity [45]. This situation can be expressed by rearranging Equation 2.10:

$$\frac{V_p}{cos\theta} \geq V_j - V_{CR} \tag{2.12}$$

The penetration velocity of jet into flyer plate material is calculated using Alekseevski-Tate equation and relative velocity of jet and flyer plate:

$$U_P = \frac{V_{rel} - \sqrt{\frac{\rho_t}{\rho_j} V_{rel}^2 + \left(1 - \frac{\rho_t}{\rho_j}\right)\frac{2(R_t - Y_j)}{\rho_j}}}{1 - \rho_t/\rho_j} \qquad V_{rel} = V_j - V_p \cos\theta \tag{2.13}$$

In an efficient interaction, the whole thickness of the flyer plate should come into contact with jet material, so that there can be a regime of non-efficient use of flyer plate material if the flyer plate is just about to be perforated:

$$\frac{V_p}{cos\theta} \geq U_p \tag{2.14}$$

The definition of "disruption efficiency" is given in Section 2.1.2. Mayseless et al [41] claimed in their fundamental paper that disruption of the jet occurs on condition that mass fluxes of jet and plate are similar. Therefore, if the mass flux of the jet is greater than that of the plate, the jet is penetrating the plate. Additionally, if the mass

fluxes are similar, or the mass flux of the plate is greater; the plate will highly disturb the jet. Based on this and assuming $\dot{m}_p = \dot{m}_J$ (i.e. $\eta=1$) for efficient interaction, a criterion for the forward moving plate velocity can be given by using Equation 2.9.

$$\frac{V_p}{cos\theta} \geq \frac{V_j}{Ksin\theta+1} \tag{2.15}$$

For $\dot{m}_p < \dot{m}_J$, deflection of the jet will occur, as in the case of backward moving plate. Above mentioned penetration conditions indicate the regimes of interaction and are summarized in Table 2.1.

Table 2.1 Summary of regimes of interaction between SCJ and FMP

Regime #	**Description**	**Criterion**	**Remarks**
1)	No interaction	$\frac{V_p}{cos\theta} \geq V_j$	Plate is faster than jet
2)	No penetration	$\frac{V_p}{cos\theta} \geq V_j - V_{CR}$	$V_{CR} = \sqrt{\frac{2(R_t - Y_j)}{\rho_j}}$
3)	Partial penetration but no perforation of the plate	$\frac{V_p}{cos\theta} \geq U_p$	$U_P = \frac{V_{rel} - \sqrt{\frac{\rho_t}{\rho_j}V_{rel}^2 + \left(1 - \frac{\rho_t}{\rho_j}\right)\frac{2(R_t - Y_j)}{\rho_j}}}{1 - \rho_t/\rho_j}$ $V_{rel} = V_j - V_p cos\theta$
4)	Effective interaction	$\frac{V_p}{cos\theta} \geq \frac{V_j}{Ksin\theta + 1}$	η is taken as 1
5)	Deflection of the jet	$\frac{V_p}{cos\theta} < \frac{V_j}{Ksin\theta + 1}$	

In regime 1, the velocity of the contact point on the plate (intersection of jet direction vector and plate) is faster than the jet. Therefore, the jet cannot touch the plate and no interaction occurs.

In regime 2, minimum velocity of the jet for penetration of the plate is found by taking the penetration velocity in Alekseevski – Tate model which depends on the plate's resistance to penetration, jet material yield strength and jet density. Therefore, if the phase velocity is lower than this critical velocity, the jet cannot penetrate the plate and ricochets from the surface of the plate. Although no jet escapes from the plate, this is not an efficient way of interaction since the plate will be consumed quickly by getting out of sight of the jet's direction and will not interact with the tail section of the jet.

The regime 3 is also another way of inefficient interaction of jet with the forward moving plate since the whole thickness of the flyer plate does not come into interaction with the jet. Instead, partial penetration occurs and the plate is not perforated. More efficient use of plate material and explosive thickness can be achieved in the fourth regime, with less amount of explosive which means lower collateral damage

The regime 4 is the most efficient interaction regime since non-steady interaction of the plate and jet results in a highly disrupted jet. The minimum velocity requirement is calculated by taking the disruption efficiency parameter ($\eta = \dot{m}_p/\dot{m}_j$) as unity [43].

The regime 5 accounts for the deflection of the jet for the interaction of the forward moving plate with the lead sections of the jet as the plate achieves its final velocity. This regime is also the general case for the backward moving plate.

The regimes of interaction are shown in Figure 2.3 for the interaction of a copper jet of 3 mm in diameter with high strength steel plate of 5 mm thickness and a NATO angle of $\theta = 60°$ for varying V_{pj} ($V_{pj}=V_p/V_j$). The figure reveals that regime 4 is around $V_{pj}=0.2$, which begins with the maximum efficiency line and ends with the no perforation of the plate, indicating the beginning of regime 3.

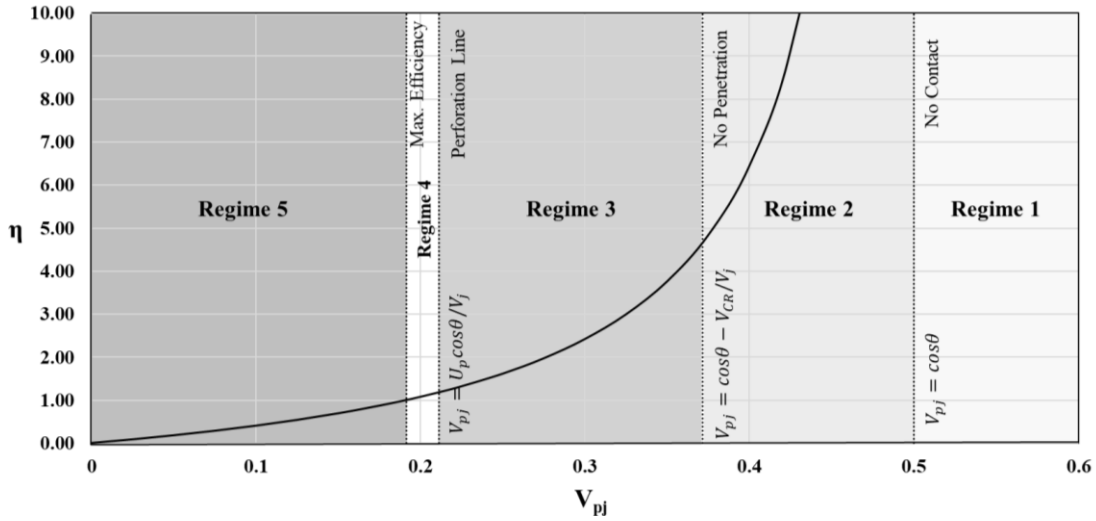

Figure 2.3 Disruption efficiency for varying V_{pj} with different regimes of interaction

2.3. Numerical Simulations

This part summarizes the findings from the numerical simulation study. Engineering models that describe the interaction are presented in Sections 2.1. In common, momentum transfer to the jet in transverse direction is taken into account to estimate the deviation from original direction. The efficiency of the moving plate is attributed to the amount of momentum transfer. In spite of their simplicity, these models proved to be efficient in quickly comparing different flying plate configurations. For further evaluation of the jet-plate interaction, configurations for varying mass-flux ratio are simulated.

For simplification and ease of comparison with postulated criteria (Section 2.2), copper jets of constant diameter and velocity are impacted on flat flyer plates of constant velocity. The velocity and diameter of the jet, and thickness and velocity of the flyer plate are varied to achieve different mass-flux ratios while keeping all the other parameters constant. Simulations are performed in commercial 3D Eulerian hydrocode SPEED. Simulation matrix is given in Table 2.2. As it is evident from engineering models, FMP disturbs the jet much more than the BMP as a result of the lower phase velocity, and therefore emphasis is given to the interaction with FMP.

Table 2.2 Simulation matrix

Sim #	Type	V_j [mm/μs]	V_p [mm/μs]	d_j [mm]	h [mm]	η (Equation 2.7)	Regime (Figure 2.3)
R1	BMP	5	1	3	5	0.46	
R2	FMP	5	1	3	5	1.08	
1	FMP	8	0.9	3	10	0.93	5
1M*	FMP	8	0.9	3	10	0.93	5
2	FMP	5	0.9	3	10	1.82	4
3	FMP	4	1.2	3	10	4.76	3
4	FMP	4.9	0.9	3	5	0.93	4
5	FMP	3.4	0.9	3	5	1.82	3
6	FMP	8	0.9	3	9	0.84	5
7	FMP	8	0.9	3	4	0.37	5
8	FMP	4	1.8	3	5	14.29	2
9	FMP	4	1.2	3	5	2.44	3
10	FMP	4	1.1	3	5	1.96	3
11	FMP	4	1	3	5	1.61	3
12	FMP	4	0.9	3	5	1.32	3
13	FMP	4	0.8	3	5	1.08	4
14	FMP	4	0.7	3	5	0.87	5
15	FMP	4	0.6	3	5	0.69	5
16	FMP	4	0.5	3	5	0.54	5
17	FMP	4	0.4	3	5	0.40	5

*: Plate material's strength is 1500 MPa.

In the simulations, half symmetry of the interaction is taken into consideration to reduce the run time of simulations. Plate size is taken as 150x150 mm. The jet length is taken as 150 mm. Shock equation of state and Johnson-Cook strength and failure models are used for plate and jet materials. The mesh size is taken as 0.5 mm for the entire x-axis (along the jet axis), whereas, for y-axis 0.5 mm from 0 to 10 mm, and between 0.5 and 1 mm up to 50 mm with a growth factor of 1.1, and 1 mm between 50-80 mm. Similar mesh size is applied in z-axis; 0.5 mm between 0 to 10 mm, 1 mm up to 30 mm with a growth rate of 1.1, and 1 mm between 30-60 mm. The resulting number of cells is approximately 8.5 million with an average run time of 2 days per simulation. The accuracy due to chosen mesh size is further validated by

varying average mesh size from 1.0 mm down to 0.2 mm and no significant change is observed between 0.5 mm and 0.2 mm.

A screenshot of the simulation model, at the beginning of simulation is given in Figure 2.4.

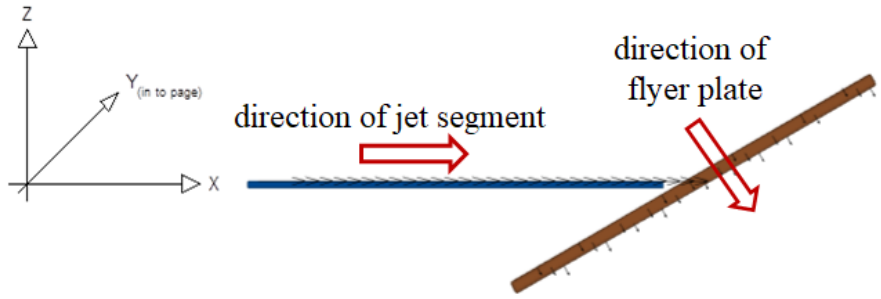

Figure 2.4 Simulation model setup for FMP

2.3.1. Detailed Analysis of the Simulation Results

Simulations R1 and R2 are compared for the interaction type of BMP and FMP. A jet segment of a constant 3 mm diameter and 5 mm/μs velocity is impacted on 5 mm thick high hardness steel plate moving at 1 mm/μs velocity at 60° obliquity. The snapshots of simulations at 30 μs for BMP and 45 μs for FMP are given in Figure 2.5. The momentum diagram of jet material at transverse direction is given in Figure 2.6.

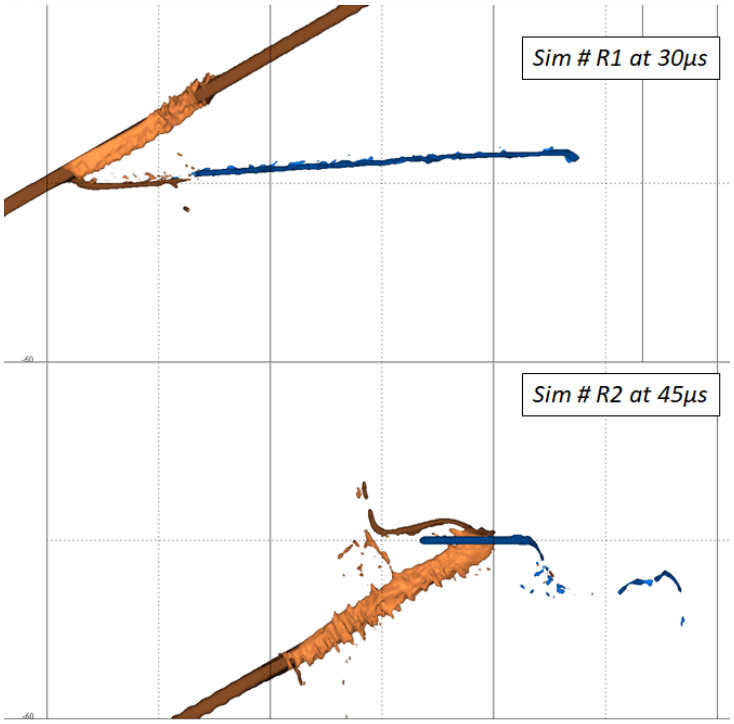

Figure 2.5 General interaction types for flyer plates, top: BMP (at 30μs) and bottom: FMP (at 45 μs)

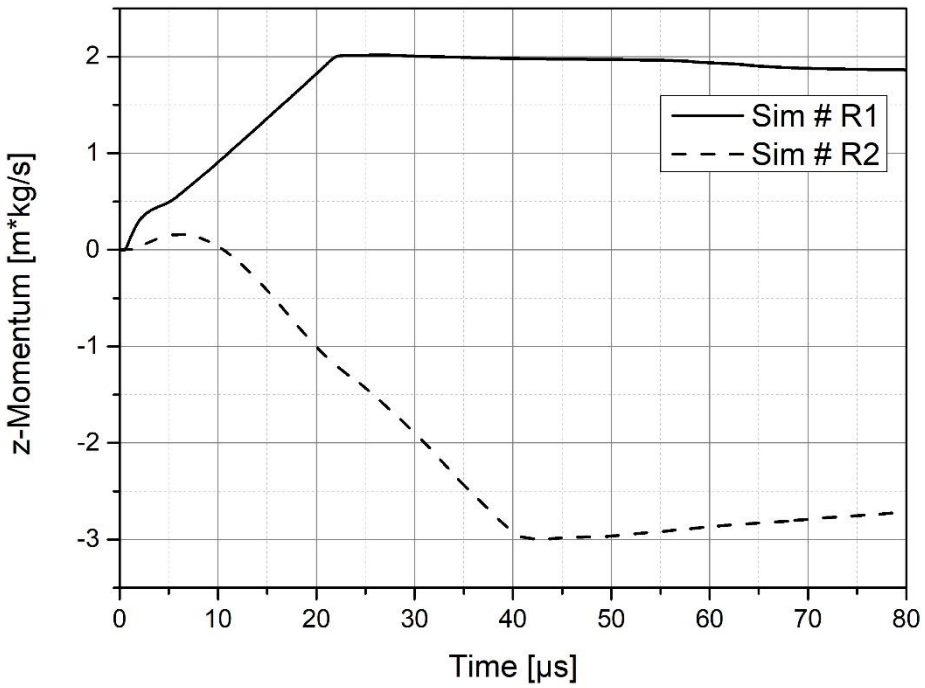

Figure 2.6 Comparison of momenta of jet for #R1 and R2 at transverse direction

It is evident that interaction with BMP slightly deflects the jet whereas with FMP yields in highly disruption of the jet. This result is also indicated from the disruption efficiencies (η) of 0.46 and 1.08, respectively. Further confirmation can also be observed from the comparison of transverse momenta of the jets due to interaction with BMP and FMP. The net momentum transfer in FMP is 1.5 times that of BMP.

The effect of plate material strength is examined by comparison of simulation #1 and 1M. Plate material is taken as St1006 (having 350 MPa yield strength) in simulation #1 and high hardness steel (with 1504 MPa yield strength) in simulation #1M. The comparison of simulations at 30 μs and jet momenta are given in Figure 2.7 and Figure 2.8, respectively.

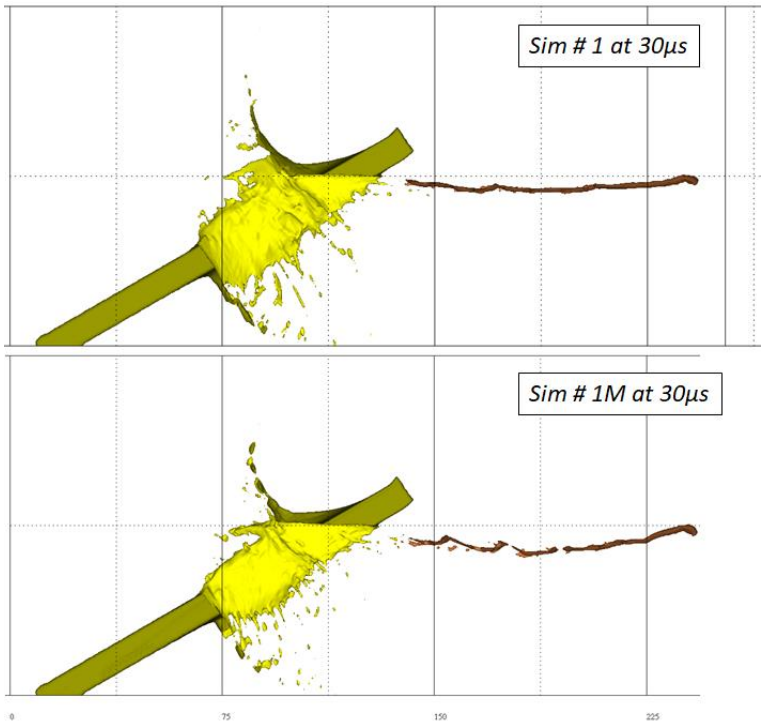

Figure 2.7 Comparison of simulation #1 and 1M at 30 μs

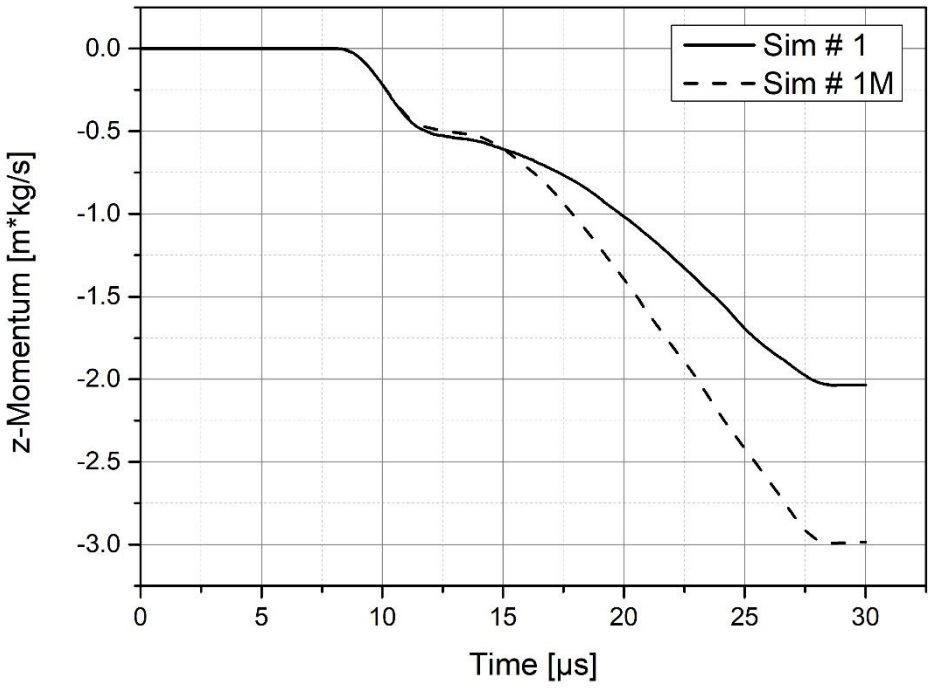

Figure 2.8 Comparison of jet momenta for simulation #1 and 1M

It is seen from Figure 2.7 that flyer plate strength has an impact on jet disruption. Comparison of jet material momentum change also confirms this result. From Figure 2.8, it can be observed that harder plate transfers more transverse momentum than the softer plate.

Simulation #1 and 4 are compared for results of different combinations of jet velocity and plate thickness which yield the same disruption efficiency 0.93. Simulation screenshots and transverse momenta of jet material are given in Figure 2.9 and Figure 2.10.

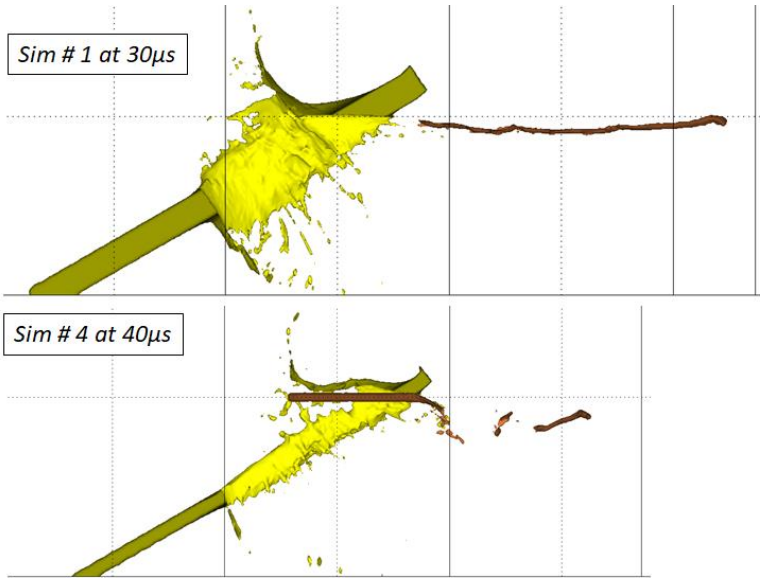

Figure 2.9 Comparison of simulation # 1 and 4 at 30 µs and 40 µs respectively

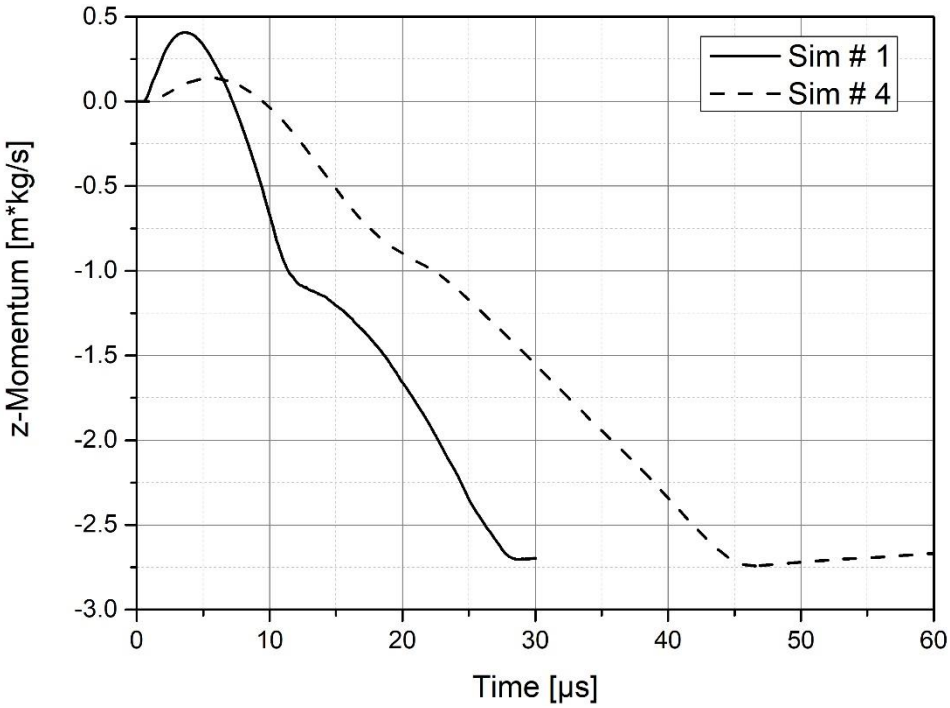

Figure 2.10 Comparison of jet momenta for simulation #1 and 4

The comparison of mass flux ratios of simulation #1 and 4 predicts a similar type of interaction, which is further supported by momentum transfer to the jet material (Figure 2.10) with a similar slope to the negative z-values. The positive values in

momenta are a result of first impact and deflection of front portion of the jet in upwards direction. As the jet penetrates the plate and steady state interaction begins, the jet is being deflected in negative z-direction and the momenta gets negative values. The comparison of the screenshots of simulations (Figure 2.9) reveals a slightly disturbed jet for simulation #1 and a highly disrupted jet for simulation #4. Also interaction time of the simulation #4 is higher than #1, which is also sustained jet disruption. This results from the fact that, each configuration lies close to the transition line between regimes 4 and 5 of Table 2.1, and there is no clear transition between these regimes. Thus, simulation #1 yielded interaction of regime 5, whereas simulation #4 revealed regime 4.

A similar result is observed by comparing simulation #2 and 5, for which η is 1.82. Screenshots and comparison of jet transverse momenta are given in Figure 2.11 and Figure 2.12, respectively.

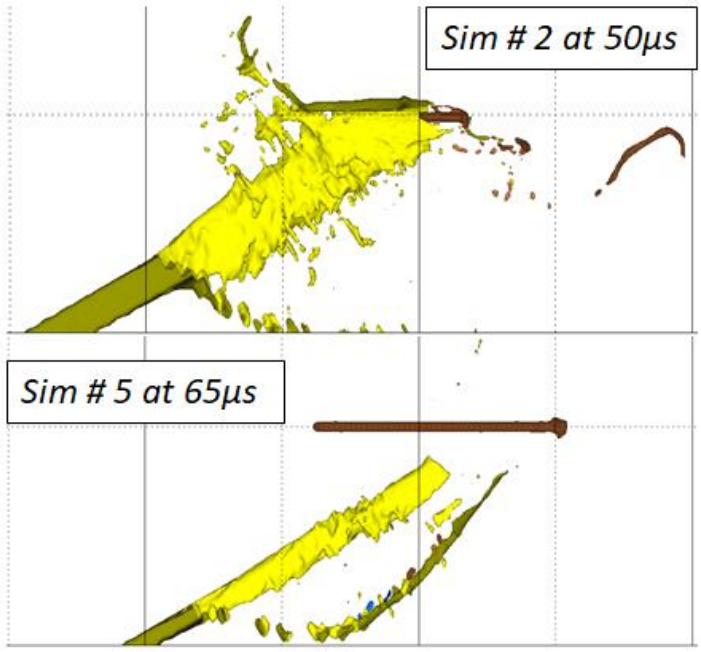

Figure 2.11 Comparison of simulation # 2 and 5 at 50 μs and 65 μs respectively

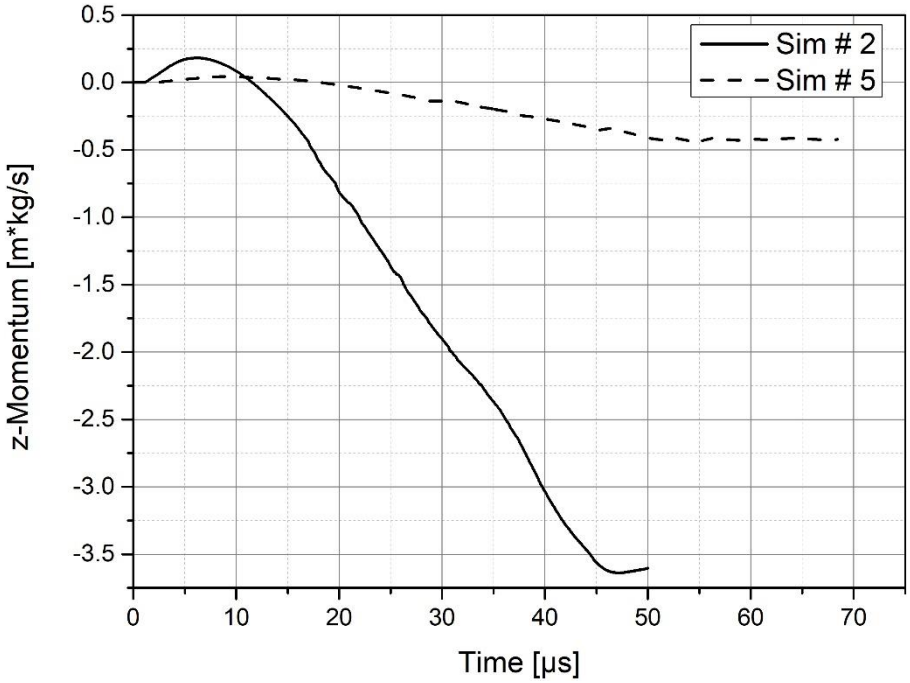

Figure 2.12 Comparison of jet momenta for simulation #2 and 5

The predictions for interactions of simulations #5 and 2 fall into regimes 3 and 4 when Table 2.1 is considered, despite of the fact that their mass flux ratios are the same. As expected, no complete perforation of plate is observed for simulation #5 (Figure 2.11). Nevertheless, the plate is too fast and quickly gets out of line of sight of the jet, clearing the way for the tail of the jet to escape undisturbed. On the other hand, disruptive type of interaction is observed for simulation #2 and as a result, the momentum transfer to the jet is higher (Figure 2.12).

In simulation #3 and 9; jet diameter and velocity and plate velocity are kept constant and the plate thickness is decreased from 10 to 5 mm. The resulting η are 4.76 and 2.44 respectively. Comparison of simulation screenshots and jet transverse momenta are given in Figure 2.13 and Figure 2.14.

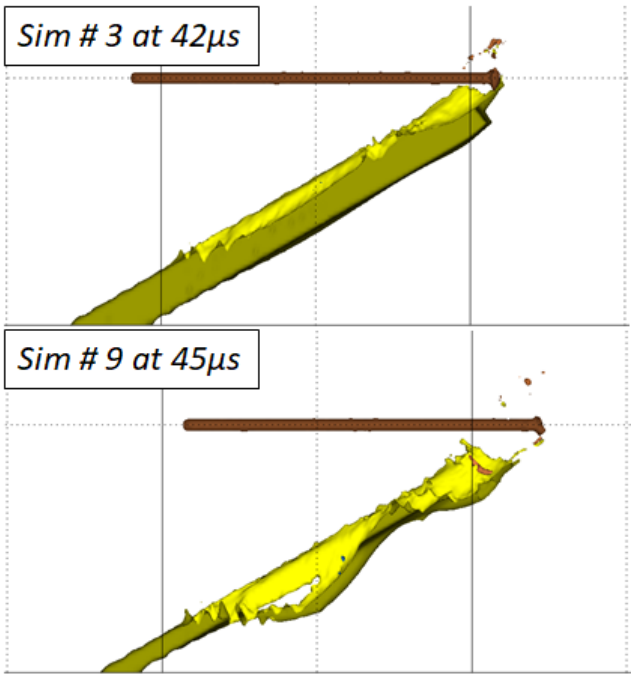

Figure 2.13 Comparison of simulation # 3 and 9 at 42 and 45 μs respectively

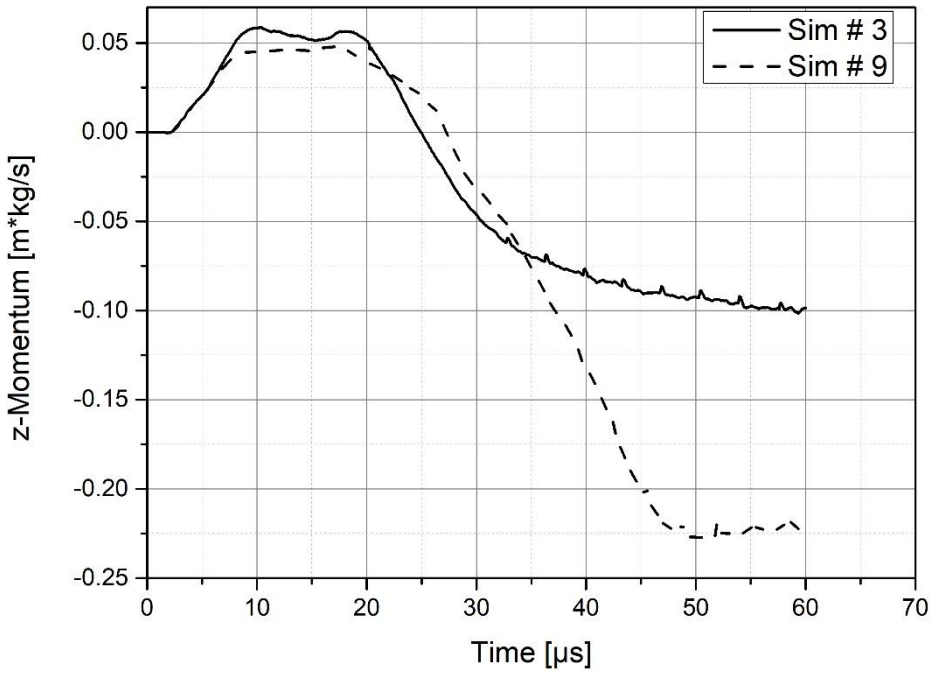

Figure 2.14 Comparison of jet momenta for simulation #3 and 9

Both of the simulations #3 and 9 yield interaction in the regime 3, which can be predicted by using Table 2.1. Front section of the jet is being deflected in the upward

direction therefore as shown in Figure 2.14 momentum in z-direction slightly increases in positive direction, yet, after the penetration starts, momentum starts to decrease, as the process goes on. In simulation 9, the jet penetrates more into the plate (however not the perforation of the whole thickness) and gets more momentum transfer in negative z-direction. In both cases, the plate is too fast and quickly gets out of line of sight of the jet and the rest of the jet escapes intact.

A similar comparison is made with simulations #1, 6 and 7, in which plate thickness is taken as 10, 9 and 4 mm respectively; and all other parameters are kept constant. The comparison of simulation screenshots and resulting jet momenta are given in Figure 2.15 and Figure 2.16.

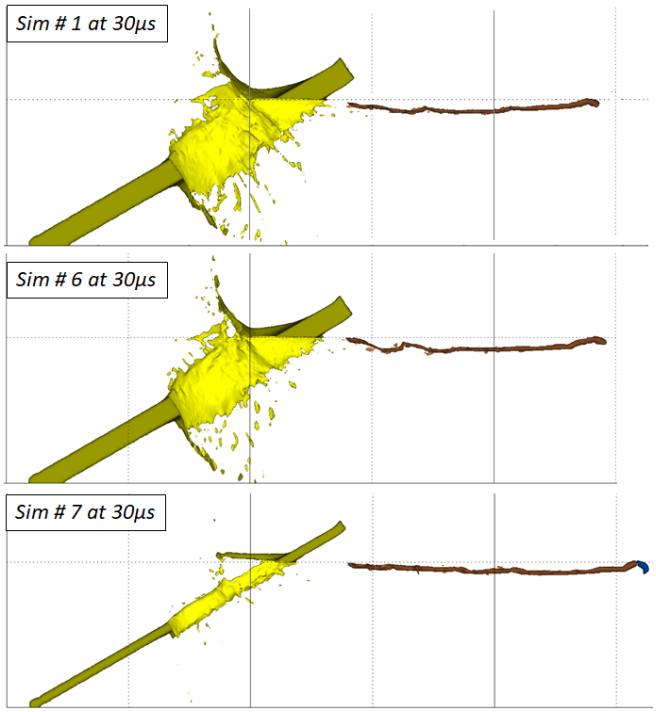

Figure 2.15 Comparison of simulation # 1, 6 and 7 at 30 μs respectively

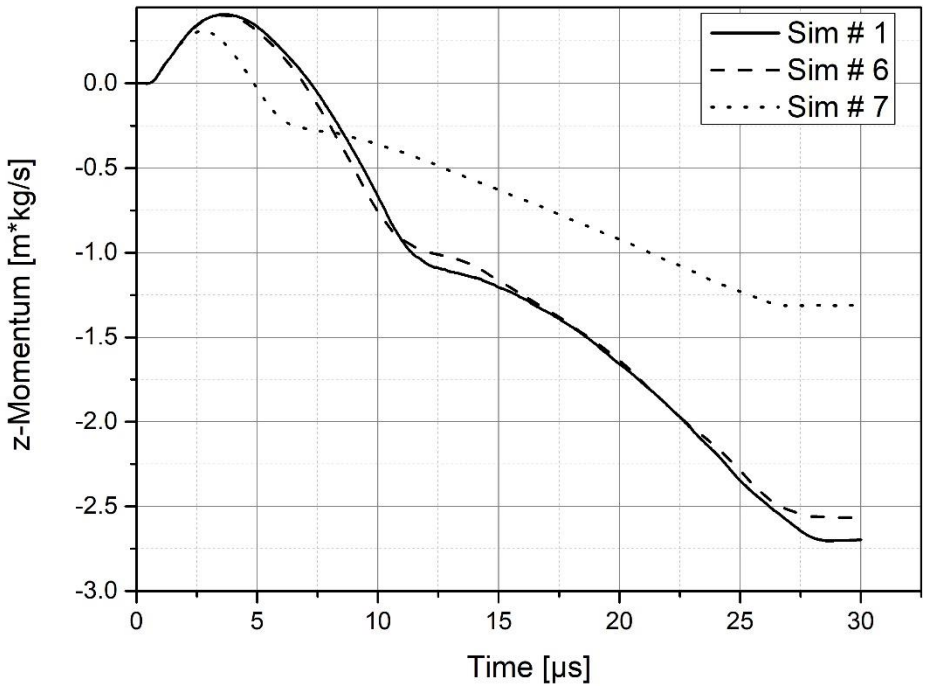

Figure 2.16 Comparison of jet momenta for simulation #1, 6 and 7

The disruption efficiency (η) decreasing for #1, 6 and 7, so it is expected that the jet will be less disturbed by increasing ratio. Transfer of transverse momentum to jet material supports this (Figure 2.16).

The plate velocity is decreased throughout simulations #8, 9, 10, 11, 12, 13, 14, 15, 16 and 17 and all the other parameters are kept constant. The disruption efficiency (η) therefore decreases. The comparisons of simulation screenshots and jet momenta are given in Figure 2.17 and Figure 2.18.

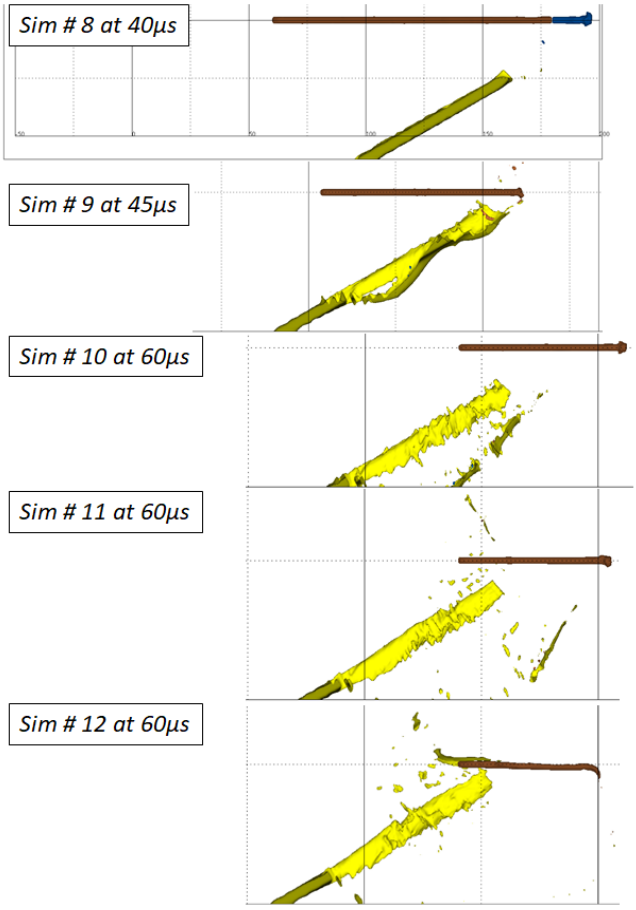
Sim # 8 at 40µs
Sim # 9 at 45µs
Sim # 10 at 60µs
Sim # 11 at 60µs
Sim # 12 at 60µs

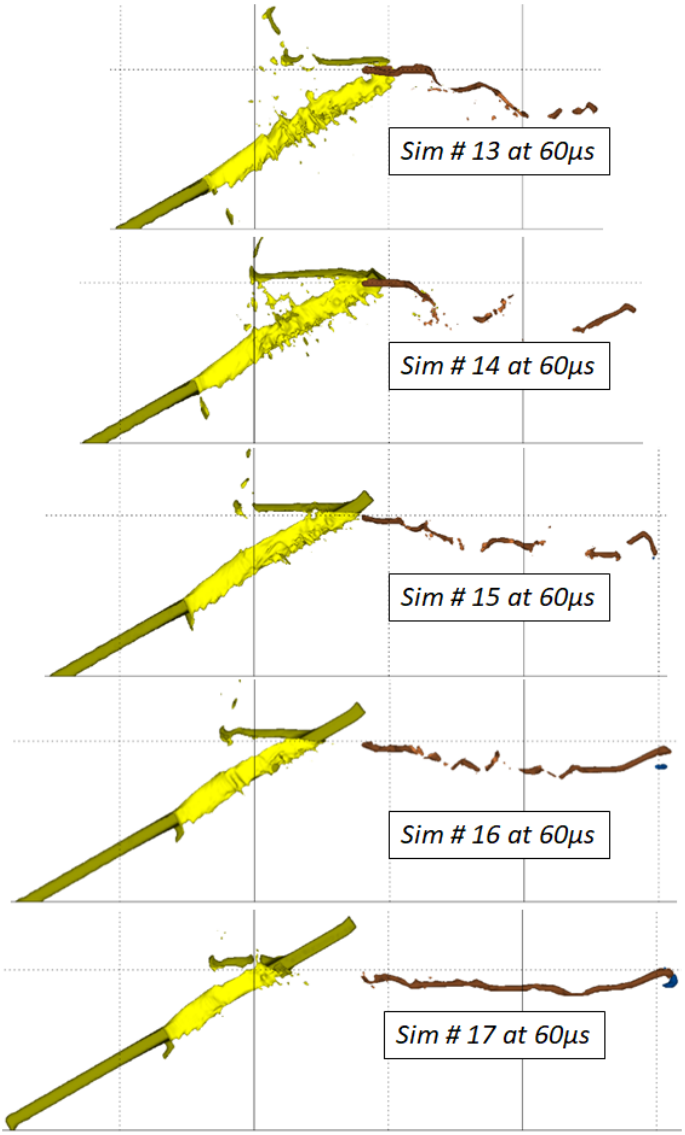

Figure 2.17 Comparison of simulation #8, 9, 10, 11, 12, 13, 14, 150 16 and 17

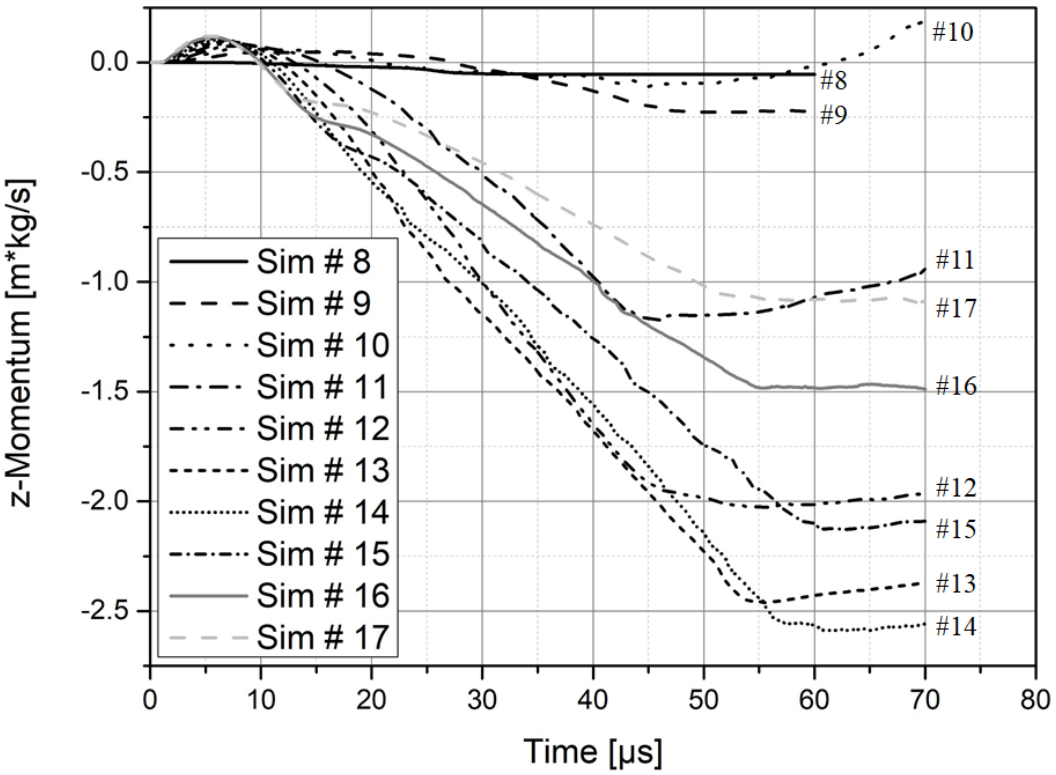

Figure 2.18 Comparison of jet momenta for simulation #8, 9, 10, 11, 12, 13, 14, 15, 16 and 17

As the interaction regimes are examined, simulation #8 fall into regime 2, simulations #9, 10, 11 and 12 fall into regime 3, simulation #13 fall into regime 4 and simulations #14, 15, 16 and 17 fall to regime 5. This prediction is supported by simulation results presented in Figure 2.17, in which, the largest disturbances are observed for simulations #13 and 14. Moreover, the comparison of the average slopes of jet momenta at the steady-state interaction given in Figure 2.19 indicates increasing negative slopes for #10, 11 and 12, with 12 being the highest of all, whereas similar slopes for 13 and 14 and decreasing slopes for #15, 16 and 17. The slopes for #12, 13 and 14 are the highest, with 12 being slightly higher. However, interaction time for #12 is lower as a result of plate moving away from the path of the jet. Thus the total momentum transfer of #12 is lower than those of #13 and 14. #14 achieved the highest total momentum transfer. #13, falling into regime 4, performed slightly lower total momentum transfer with regard to #14, falling into

regime 5. This suggests that there is no sharp transition of interaction efficiency between regimes 3, 4 and 5.

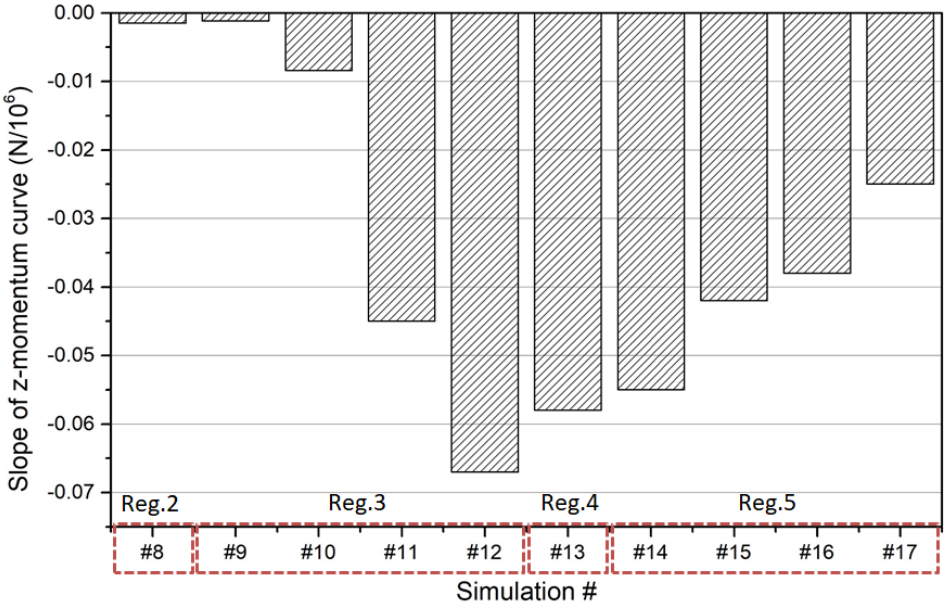

Figure 2.19 Comparison of average slope of z-momentum curves for simulations

The calculation of limit velocity for regime 3 necessitates estimation of target resistance to penetration R_t and dynamic jet yield strength Y_j. Walters [46] suggests R_t values being equal to 1-3 times that of yield strength of target material, whereas Rosenberg [47] suggests 4-6 times. This correction in R_t compensates for the effects of strain, strain-rate and state of non-uniaxial stress state. This correction factor is taken as 5 in the calculations, and the resulting interaction efficiency (η) versus V_{pj} (V_p/V_j) plot is given in Figure 2.20 for clear comparison of simulations.

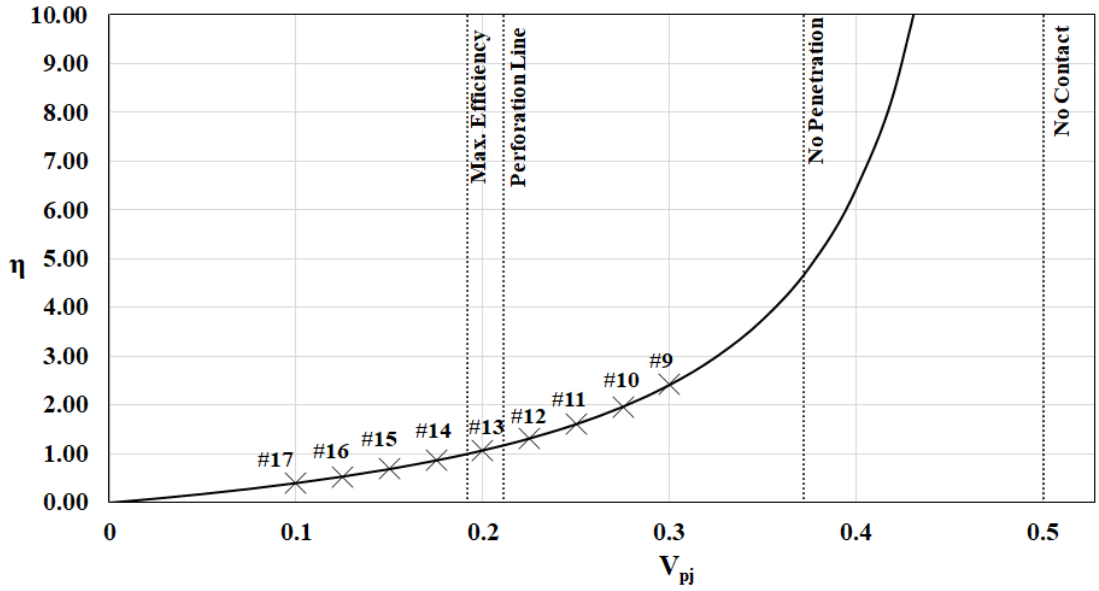

Figure 2.20 Interaction efficiency versus V_{pj} plot for simulations #9-10-11-12-13-14-15-16 and 17 (#8 is out of range of plot)

To sum up, simulation study proves suggested interaction regimes for FMP shown in Table 2.1, however, there is no clear cut transition between these regimes.

CHAPTER 3

ENGINEERING MODEL FOR CALCULATION OF PENETRATION BEHIND ERA

Design of ERA cassette necessitates evaluation of several design parameters such as selection of cassette materials and their thicknesses, cassette size, obliquity of the impact, stand-off distance of the warhead, space between ERA cassette and witness plate (or vehicle structure), SCJ impact position and similar parameters. Hydrocode numerical simulations provide good results in qualitative manner however, the time needed for each simulation ranges from a few hours to a couple of days, depending on mesh size. In order to achieve optimization of ERA cassettes, the design matrix should include trials of combinations of several parameters. Thus, finding a suitable solution will take too much simulation time. Therefore, an engineering model will be a valuable tool for estimating the effects of such design parameters quickly, in addition to hyrocode numerical simulations.

Formation of an engineering model capable of handling these design parameters requires an understanding of the physical processes occurring during the interaction of the SCJ with ERA flyer plates. The main physical processes that determine the efficiency of ERA should include: 1) formation of holes in the plates of ERA cassettes when they contact with SCJ; 2) initiation of detonation in the explosive charge; 3) explosive acceleration of plates; 4) interaction of moving plates with SCJ.

It is evaluated that the engineering model should be able to deal with the aforementioned tasks, by considering the physical events in the order of occurrence during the interaction. This chapter covers the work done for the basics of the engineering model and evaluation of the results.

There are several studies in literature that cover SCJ penetration at various stand-off distances and interaction of SCJ with reactive armor. Hancock [48] classifies these SCJ penetration models either empirically or geometrically according to the treatment of particles' drift and cutoff velocities. The well-known DSM model (DiPersio-Simon-Merendino) [49] is an example of empirical modeling of SCJ penetration. Examples of geometrical models can be found in [50, 51, 52, 53]. Works on reactive armor models include empirical modeling [54, 55] and geometrical modeling [56].

In this study, a pragmatic choice is made in favor of empirical modeling, since geometrical modeling will also require experimental data on drift velocities and break-up times, and fitting of statistical modeling parameters.

3.1. Shaped Charge Jet Penetration

The first object is to model the SCJ penetration into a semi-infinite target, and be able to capture the variance of depth of penetration with SOD - stand of distance (from the shaped charge warhead cone base to the witness plate).

The main approach is to approximate the SCJ as a discrete series of particles with known axial velocities, lengths, positions and densities; taken as an output from hydrocode numerical simulation of jet formation and to be used as input for the engineering model calculations of the jet interaction with ERA and base armor. The drift velocities are assumed zero and the reduction of penetration due to these velocities is accounted for with an approximation mentioned in Section 3.1.3. Then, a hydrodynamic penetration is assumed to take place. Particles are assumed to elongate during the flight to the penetration channel because of the velocity gradient in the jet. This elongation ends as breakup takes place.

3.1.1 Penetration Velocity

Penetration velocity is calculated from the theory of Alekseevski-Tate [44, 4] by the following equation.

$$U_P = \frac{v_j - \sqrt{\frac{\rho_t}{\rho_j}v_j^2 + \left(1-\frac{\rho_t}{\rho_j}\right)\frac{2(R_{tP}-Y_j)}{\rho_j}}}{1-\rho_t/\rho_j} \tag{3.1}$$

In 3.1, it is important to note that the target resistance to penetration R_{tP} is different than the target resistance to hole growth R_{tR}, which will be assessed later.

3.1.2 Semi-Infinite Target Crater Diameter

Target crater diameter formed by the impact of a jet particle on the semi-infinite target is calculated by the Szendrei equation [57].

$$D_{cf} = \frac{\sqrt{\rho_t \rho_j}\, d_j v_j}{\sqrt{2R_{tR}}\left(\sqrt{\rho_t} + \sqrt{\rho_j}\right)} \tag{3.2}$$

3.1.3 Calculation of Penetration

The jet is assumed to elongate without any drift velocity up to break-up time. After that, the particles are assumed to disperse and do not elongate any more. The depth of penetration is calculated with the following equations along the jet, up to penetration cutoff velocity [54].

$$dP = \frac{U_p}{v_j - U_p} l_j \qquad (t_{arrival} \le t_b) \tag{3.3a}$$

$$dP = \frac{U_p}{v_j - U_p} l_j \left(1 - \frac{g}{g_0}\right) \qquad (t_{arrival} > t_b) \tag{3.3b}$$

$$P = \sum_{i=1}^{n} dP \tag{3.4}$$

It should be noted that Equation 3.3a accounts for the penetration of jet particles before the break up whereas Equation 3.3b applies after the break up [58]. In Equation 3.3b, g is the gap distance between particles, non-dimensionalized with respect to jet piece length and g_0 is an empirical parameter that accounts for the quality of the warhead, generally taken as 4-6 for small or non-precision shaped charges. The break-up times are calculated as given by Hancock [48]. The elongated

length of the jet particle at the time of impact is calculated with the following equations.

$$l_j = l_j^i + t_{arrival}\Delta V \qquad (t_{arrival} \leq t_b) \qquad (3.5a)$$

$$l_j = l_j^i + t_b\Delta V \qquad (t_{arrival} > t_b) \qquad (3.5b)$$

Correction of the jet diameter is also made by assuming that there is no volume change.

$$d_j = \sqrt{\frac{l_j^i}{l_j}} d_j^i \qquad (3.6)$$

3.2. Breakup Times

A breakup model is needed to model the penetration of particulated jet. The model from Hancock is employed to estimate the breakup times of jet segments [48]. His model assumes breakup time duration τ_b is related to the slope of accumulated mass curve of SCJ.

$$\pi\rho_j c_b^2 \tau_b^3 = -dM/dv \qquad (3.7)$$

where, c_b is the necking speed. The assumption is, all particles are originated from the virtual origin, at time zero, therefore, it is needed to make a conversion to calculate break-up times of particles according to clock of the model. Breakup time t_b, according to model clock is deduced from virtual origin time (Figure 3.1):

$$\tau_b = t_b - t_{VO} \qquad (3.8)$$

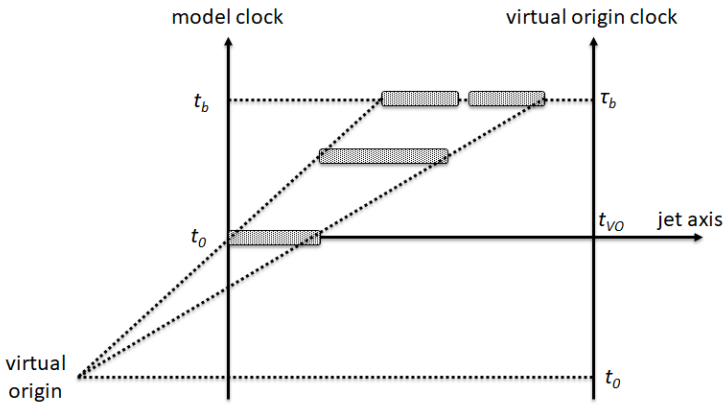

Figure 3.1 Model and virtual origin clock demonstration for a sample jet particle

3.3. Penetration Cutoff Velocities

Modeling of drifting and tumbling of jet particles and hence hitting edges of the penetration channel is not taken into account. Therefore, it is necessary to define at which point, the shaped charge jet ceases penetration process. The choice is to use a penetration cutoff velocity criterion and omit penetration of slower particles according to U_{min} model of Hancock [48]. This model will be a plausible assumption, since, the cutoff velocity will be a function of stand-off distance.

In his model, the minimum penetration velocity U_{min}, is assumed to be a function of radial drift of particles δ_r and jet particle break-up radius r_b:

$$U_{min} = U_0(1 + b\delta_r/r_b) \tag{3.9}$$

where, U_0 and b are model parameters. It is assumed that particle drift occurs at a velocity v_d beginning from the virtual origin, so that:

$$\delta_r = v_d(t - t_{VO}) \tag{3.10}$$

Moreover, it is assumed that break-up time duration τ_b and break-up radius r_b are proportional with necking speed c_b along the entire jet:

$$\tau_b(v) = r_b(v)/c_b \tag{3.11}$$

Finally, penetration cutoff velocity v_c will be found by equating average penetration rate to zero:

$$\frac{v_c}{1+\gamma(1+g/L)} - U_{min} = 0 \tag{3.12}$$

where, $\gamma = (\rho_t/\rho_j)^{1/2}$, if hydrodynamic penetration is assumed.

3.4. Interaction with Reactive Cassette

Interaction of shaped charge jet with the reactive cassette is handled with the following sequence:

- SCJ penetrates the BMP and crater (hole) growth is initiated
- As soon as SCJ touches the explosive layer, flyer plates start to accelerate
- SCJ penetrates the FMP and crater (hole) growth is initiated
- The escaping parts are calculated taking into account:
    - The crater (hole) closure durations for BMP and FMP, for escaping jet precursor
    - Life durations of BMP and FMP for escaping jet tail (i.e. when the plates get out of line of sight of the jet flight axis)

The residual penetration is attributed to precursor parts and undamaged tail of the jet.

Schematic view of the model setup is given in Figure 3.2.

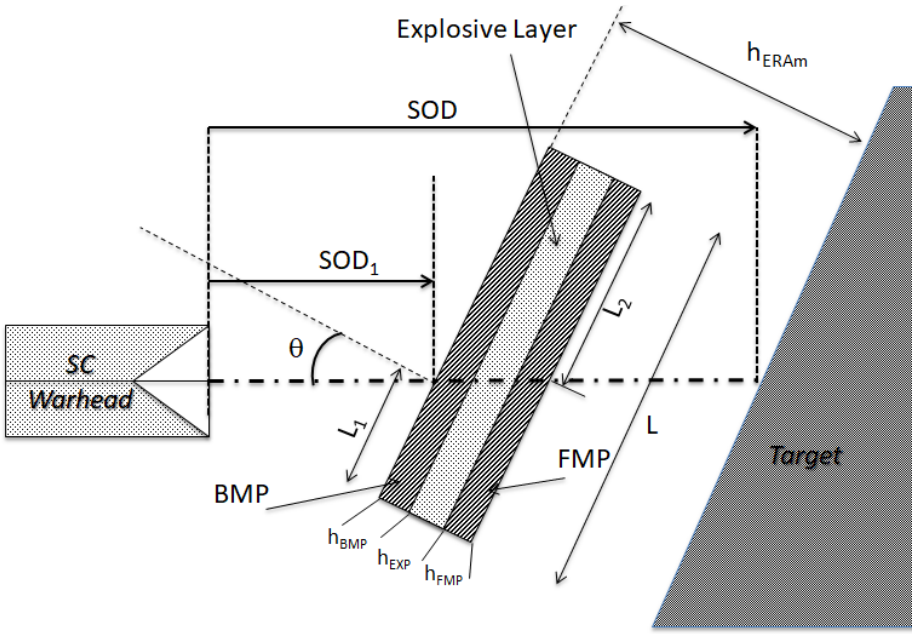

Figure 3.2 Schematic view of the model setup

3.4.1 Plate Acceleration

Final plate velocity as a result of explosive acceleration is calculated by using the Gurney velocity approach [31, 59, 60].

$$M = \rho_{FP} h_M \qquad N = \rho_{FP} h_N \qquad C = \rho_{EXP} h_{EXP} \qquad A = \frac{1 + 2\frac{M}{C}}{1 + 2\frac{N}{C}}$$

$$V_{PM} = V_G \left[\frac{(1+A^3)}{3(1+A)} + \left(\frac{N}{C}\right) A^2 + \frac{M}{C}\right]^{-\frac{1}{2}} \tag{3.13}$$

Acceleration of the flyer plate is calculated with the help of an exponential expression. Therefore the velocity of the plate at time t is approximated by Equation 3.14 [61]. In Equation 3.14, τ is the acceleration time constant.

$$V_{FP} = V_{PM}\left(1 - e^{-\frac{t}{\tau}}\right) \tag{3.14}$$

3.4.2 Crater Radius on Flyer Plate

The interaction of the jet tip with the flyer plate forms a crater (hole) on the flyer plate. Crater radius in the flyer plate is calculated with the help of Naz [62] formula:

$$r_C = \sqrt{r_{cf}^2 - \left(\sqrt{r_{cf}^2 - r_j^2} - 2\sqrt{\frac{R_{tR}}{\rho_t}}t_e\right)^2} \tag{3.15}$$

t_e is the interaction time proportional to the craterization time:

$$t_e = \alpha \frac{h_{FP}}{U_p cos\theta} \tag{3.16}$$

where, U_p is the penetration velocity and α is an experimentally determined coefficient set by Naz to be 4.5.

3.4.3 Crater Closure Duration

The hole is imparted on the plate as the jet penetrates. After the activation of the explosive layer, the plate is accelerated in acute direction to the jet flow. Therefore, the edge of the hole touches the jet flow at some time. This is termed as hole closure duration t_c and found by the solution of the following equality.

$$\frac{r_c}{tan\theta} = V_{PM}\left(t_c - \frac{r_c}{D} + \tau e^{\frac{\frac{r_c}{D} - t_c}{\tau}}\right) \tag{3.17}$$

It should be noted that, flyer plate starts to accelerate after the detonation wave travels distance r_c.

3.4.4 Flyer Plate Life Duration

As the flyer plates have finite lateral dimensions in real case, it is therefore necessary to define the life duration of the flyer plate as it gets out of line of sight of the SCJ flight direction.

For the BMP, life duration t_{BMP} is found by solving the following equality. Sketch regarding the interaction is given in Figure 3.3.

$$\frac{L_1}{\tan\theta} = V_{PM}\left(t_{BMP} - \frac{L_1}{D} + \tau e^{\frac{\frac{L_1}{D} - t_{BMP}}{\tau}}\right) \tag{3.18}$$

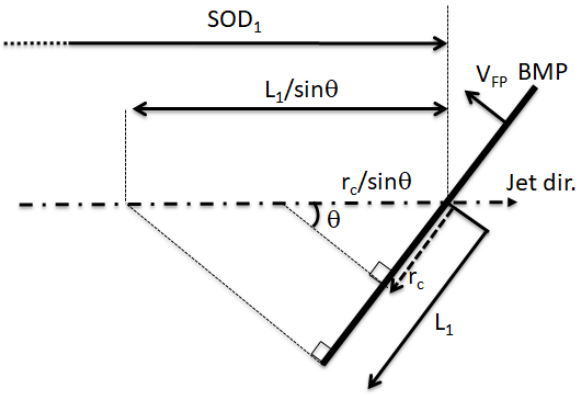

Figure 3.3 Sketch showing dimensions on BMP

The case is however different for the FMP (Figure 3.4 and Figure 3.5). The flyer plate would either move out of line of sight of the SCJ flight direction (first case) or hit the base armor and stop its motion (second case). If the following inequality is satisfied, the plate will move out before hitting the base armor (first case).

$$h_{ERAm} - h_{BMP} - h_{EXP} - h_{FMP} \geq \frac{L_2}{tan\theta} \tag{3.19}$$

In this case, the life time t_{FMP} is the solution of the following equality (Figure 3.4).

$$\frac{L_2}{\tan\theta} = V_{PM}\left(t_{FMP} - \frac{L_2}{D} + \tau e^{\frac{\frac{L_2}{D} - t_{FMP}}{\tau}} - \tau\right) \tag{3.20}$$

In the second case, FMP hits the base armor and stops thus, the life time t_{FMP} is the solution of the following equality (Figure 3.5).

$$t' = t_{FMP} - \frac{(h_{ERAm} - h_{BMP} - h_{EXP} - h_{FMP})tan\theta}{D} \tag{3.21a}$$

$$h_{ERAm} - h_{BMP} - h_{EXP} - h_{FMP} = V_{FP}\left(t' + \tau e^{\frac{t'}{\tau}}\right) \tag{3.21b}$$

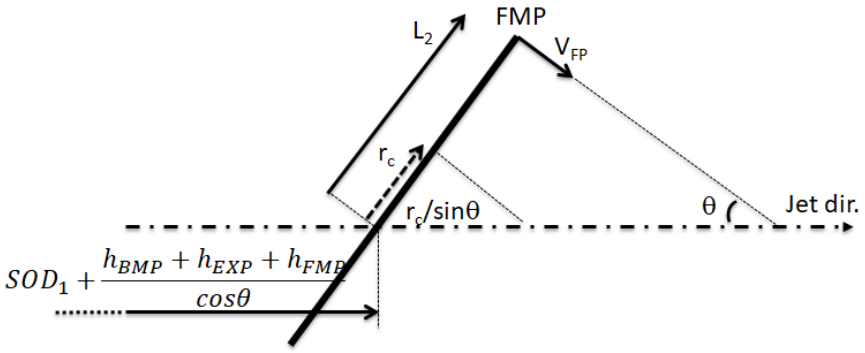

Figure 3.4 Sketch showing FMP interaction for the first case

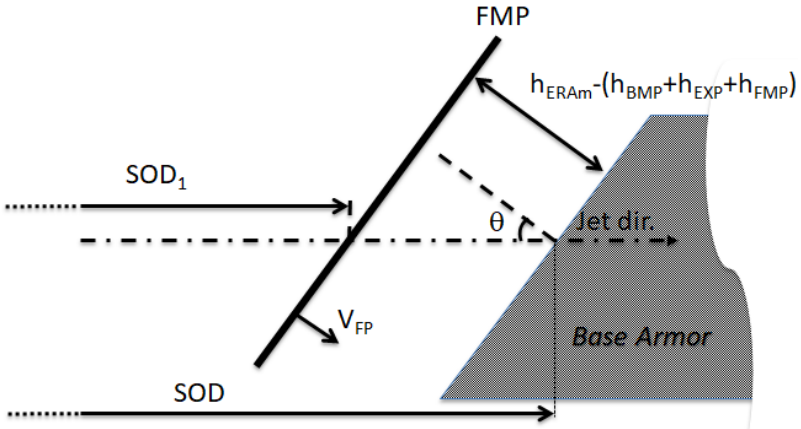

Figure 3.5 Sketch showing FMP interaction for the second case

3.4.5 Calculation of Residual Penetration

Crater radii are calculated considering the first particles that touch the flyer plates. Moreover, the activation time of explosive layer is calculated for the first particle after the penetration of the BMP. This duration is added to crater closure and flyer plate life durations.

$$t_{act} = \frac{SOD_1 + \frac{h_{BMP}}{cos\theta} - pos_i}{v_{ji}} \tag{3.22}$$

It takes some time for the edges of the holes on the BMP and FMP to reach the flight path of the SCJ. Also the plates may move out of the flight path or the FMP may hit the base armor and stop. Therefore, some jet particles escape the reactive cassette without any interaction with the flyer plates.

For the i[th] particle to escape the BMP and FMP before crater closure, the following inequalities are checked respectively.

$$pos_i + t_c^{BMP} v_{ji} > SOD_1 - \frac{r_{cm}^{BMP}}{sin\theta} \tag{3.23}$$

$$pos_i + t_c^{FMP} v_{ji} > SOD_1 + \frac{h_{BMP}+h_{EXP}+h_{FMP}}{cos\theta} + \frac{r_{cm}^{FMP}}{sin\theta} \tag{3.24}$$

For the i[th] particle to pass BMP intact, as BMP moves out, following inequality is checked.

$$pos_i + t_{BMP} v_{ji} < SOD_1 - \frac{L_1}{sin\theta} \tag{3.25}$$

Following inequalities are checked for interaction with FMP, for the case inequality in Equation 3.19 holds or does not hold respectively.

$$pos_i + t_{FMP} v_{ji} < SOD_1 + \frac{L_2}{sin\theta} + \frac{h_{BMP}+h_{EXP}+h_{FMP}}{cos\theta} \tag{3.26a}$$

$$pos_i + t_{FMP} v_{ji} < SOD \tag{3.26b}$$

After the escaping particles are determined, Equations 3.3 and 3.4 are called for these particles to determine the residual penetration due to precursor and the tail part of the shaped charge jet that escapes without having any interaction with the ERA plates.

3.5. Shaped Charge Jet Input Preparation

The analytical model accepts jet information as the position, velocity, radius and density of each jet segment or particle. The information, except the radius distribution, is easily taken from simulation result at any instant; however, some calculations need be performed to get the radius as a function of position.

Jet formation simulations are performed up to a point where the jet tip reaches the built in stand of distance of the shaped charge device. Then, the following information as the mass per unit velocity *dM/dv*, strain rate $\eta(v,t)$ and density $\rho(v,t)$

data are extracted from the simulation file. Then, using Equation 3.27 [63], diameter *d(v,t)* data is calculated for the SCJ.

$$\frac{dM}{dv} = -\rho(v,t)\ \frac{\pi}{4}\frac{d^2(v,t)}{\eta(v,t)} \tag{3.27}$$

The CAD model of the test warhead is prepared for the liner, casing and the explosive material. Then, 2D jet formation analysis is conducted with SPEED hydrocode. The setup is prepared with 0.1 mm mesh size in both directions (Figure 3.6).

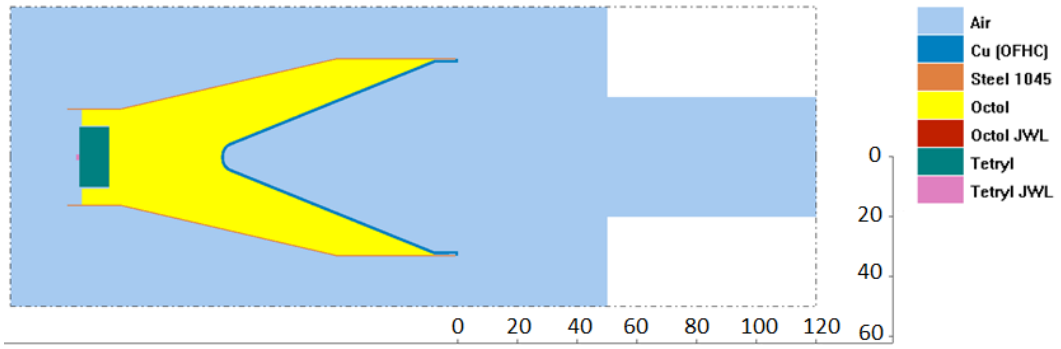

Figure 3.6 Jet formation model

The jet formation simulation is run for 32 μs. The resulting jet is given in Figure 3.7.

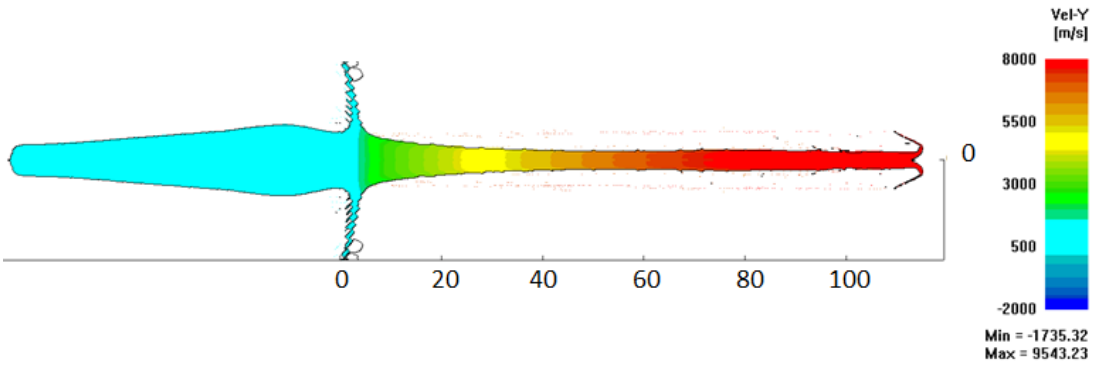

Figure 3.7 Velocity fringe plot of the jet

Jet velocity as a function of position is plotted in Figure 3.8. Tip velocity is calculated as 8437 m/s as compared to 8628 m/s, 8475 m/s, 8301 m/s and 8000 m/s after recordings from 4 test firings.

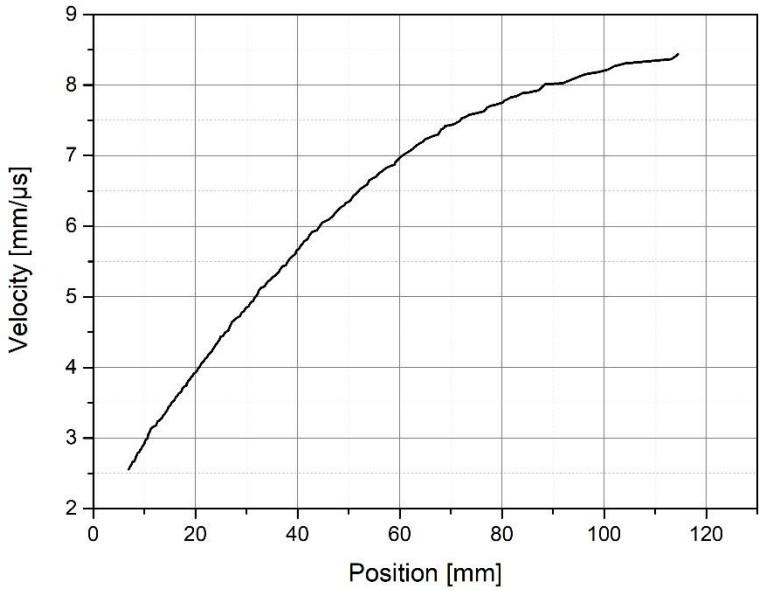

Figure 3.8 Velocity distribution along the jet obtained from jet formation simulation

CHAPTER 4

EXPERIMENTS AND SIMULATIONS

This part of the thesis covers the work done in experimental studies and numerical simulations performed to analyze the experimental results.

4.1. Experiments

Experiments are performed for the investigation of shaped charge jet interaction with non-steel reactive cassettes. First, an investigation of the available materials from international vendors is conducted. Following materials are selected from commercially available ballistic materials within the budget of the project:

- Alumina (different grades available)
- SiC (Silicon Carbide)
- B4C (Boron Carbide)
- Borosilicate glass

After the selection of candidate materials, it is necessary to form the testing plan for the procurement of materials. Following decisions are made to limit the number of free variables in the design space:

- Areal density is kept the same for comparing different materials.
- Symmetric cassette structure is employed in terms of areal density, ie. the weight of the BMP and FMP are the same.
- Obliquity of the cassette is kept the same for all configurations.
- SOD is kept the same for all tests.
- Distance between the (front face of the) cassette structure and the witness plate is kept the same for all tests.
- Explosive thickness is kept the same for all configurations.

- Test warhead is the same for all tests.

4.1.1 Material Selection

4.1.1.1. Test Charge Selection

The warhead that is used in experiments has a liner diameter of 66 mm. It is composed of four main parts, which are copper liner, steel casing, main charge, and booster charge. The apex angle of the copper liner is 44°, and the liner thickness is 1 mm. The main explosive charge is octol, and initiation is achieved by a tetryl booster, which has 20 mm diameter and 10 mm depth. Standard No-8 type electrical detonators are used to start the firing process.

RHA penetration tests are performed to have a basis for calculations of ballistic efficiency.

4.1.1.2. Explosive Sheet Selection

Two different alternatives of explosive sheet are available at the time of study. These are:

- Primasheet 2000 sheet explosive from EBAD, USA; containing 87% RDX
- Semtex Pl SEM sheet explosive from Explosia as, Czech Republic; containing 87% RDX.

3, 5 and 7 mm thicknesses of Primasheet 2000 sheet explosive is procured. It has 1.60 g/cm^3 density and 8200 m/s velocity of detonation, as reported by the vendor. Its surfaces are sticky, which is useful to fix the flyer plates in construction of ERA cassette.

4.1.1.3. Flyer Plate Material Selection

The selected candidate materials are alumina (Al_2O_3) 99.5%, alumina 98%, silicon carbide (SiC), boron carbide (B_4C) and borosilicate glass. Selection is made based on proposed physical and mechanical properties, and availability from the vendor.

Materials that are procured from international vendors are given in Table 4.1.

Table 4.1 Procured Materials

No	Commercial Name	Material	Vendor	Dimensions	Thickness
1	AK99.5	Al_2O_3 99.5%	Barat	100x100 mm	8.1mm
2	AK99.5	Al_2O_3 99.5%	Barat	100x100 mm	12.1mm
3	Corbit 98	Al_2O_3 98%	Bitossi	100x100 mm	11.2 mm
4	Corbit 98	Al_2O_3 98%	Bitossi	100x100 mm	16.8 mm
5	Hexoloy SA	SiC	Saint-Gobain	6”x6”	10 mm
6	Hexoloy SA	SiC	Saint-Gobain	6”x6”	15 mm
7	HPB4C	B_4C	Coorstek	100x100 mm	12 mm
8	Borofloat 33	Borosilicate	Schott	300x150 mm	15 mm
9	Borofloat 33	Borosilicate	Schott	300x150 mm	21 mm

Properties of the procured materials are given in Table 4.2.

Table 4.2 Material properties for ceramic materials

Property \ Brand	Unit	AK99.5	Corbit 98	Hexoloy SA	HPB4C	Borofloat33
Composition	-	Al2O3	Al2O3	SiC	B4C	Borosilicate
Density	kg/m^3	3910	3870	3130	2510	2220
Hardness (Knoop)	kg/mm^2	1530	1428	2500	3200	480
Compressive Strength at Rt	MPa	2500	2240	3900	2500	1300 [64]
Fracture Toughness	$MPa.m^{1/2}$	4	3.7	3	2.5	0.8

4.1.2 Construction of ERA Cassettes

Within the context of the thesis, symmetrical three plate ERA cassettes are constructed that consist of a front plate that faces the shaped charge jet (BMP), an explosive layer, and a back plate (FMP). Armox 500T steel plate with 3 mm nominal thickness (3.0 -0/+0.8mm thickness tolerance with 3.6 mm average measured thickness) is chosen as a reference configuration for comparison purposes. The thickness of the explosive layer is taken as 3 mm for all constructions.

Five different candidate materials are taken into consideration as alternatives to steel. The thicknesses of ceramic plates are ground to represent similar areal densities as steel plates. This ensures to achieve a close flying velocity as that of the steel flyer

plates. The candidate brittle materials are as follows: 99.5% alumina (AK99.5 supplied from Barat), 98% alumina (Corbit 98 supplied from Bitossi), silicon carbide (Hexoloy SA™ supplied from Saint-Gobain), boron carbide (HPB4C, supplied from Coorstek), and borosilicate glass (Borofloat™ supplied from Schott). The cassette construction consists of an explosive layer and two flyer plates on both sides.

ERA cassettes possessed a geometry of 300 x 150 mm. Steel and borosilicate glass plates are manufactured as single plates. Silicon carbide and boron carbide plates are constructed from multiple 150 x 150 mm tiles whereas alumina plates from 100 x 100 mm tiles. The construction of the tile assembly ensured that the shaped charge jet will hit the center of a tile (Figure 4.1).

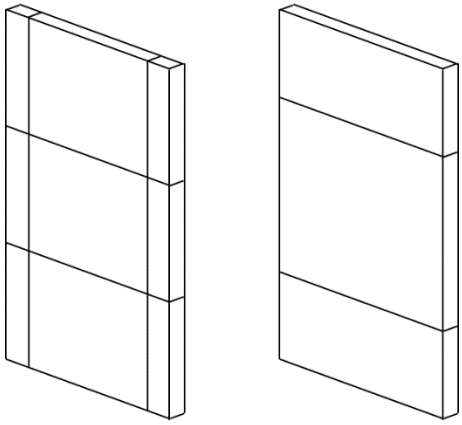

Figure 4.1 Manufacturing of flyer plates from smaller tiles (left: from 100x100mm tiles, right: from 150x150mm tiles)

The flyer plate thicknesses are given in Table 4.3.

Table 4.3 Thicknesses of the flyer plates

Material	Brand	Thickness [mm]
Steel	Armox 500T	3.6
Steel	Armox 500T	4.6
Steel	Armox 500T	6.6
Alumina 99.5%	AK99.5	8.15
Alumina 98%	Corbit 98	8.2
SiC	Hexoloy SA	9.7
B4C	HPB4C	11.7
Glass	Borofloat 33	15.0

4.1.3 Experiment Plan and Test Setup

It is decided to follow the steps below:

- Penetration into RHA at built in SOD of the warhead (Table 4.4)
- Penetration into RHA at different SODs (Table 4.4)
- Steel/Steel cassette configurations, three different areal densities, three different explosive thickness, two different obliquity (Table 4.6)
- Steel/Alternative Material cassette configurations (Table 4.7)
- Alternative Material/Steel cassette configurations (Table 4.7)
- Performance of chosen Alternative Material/Alternative Material cassettes (Table 4.7)

A standard test setup is used in all tests. Fixtures for placing the warhead and ERA cassette are designed and manufactured according to Figure 4.2.

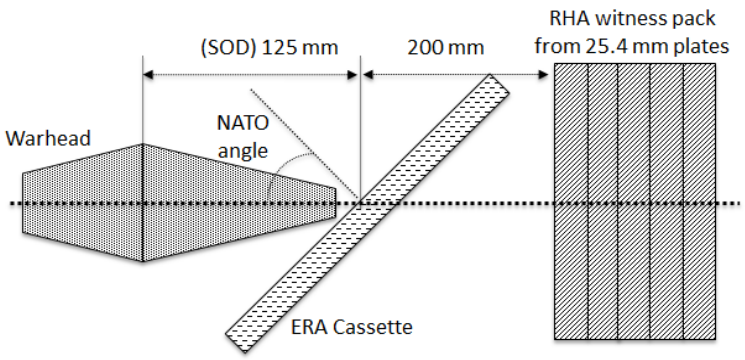

Figure 4.2 Sketch of the standard test setup for ERA cassettes

The test fixtures for holding warhead and target plate are manufactured from wood. The test configurations for RHA DOP tests and ERA tests are given in Figure 4.3 and Figure 4.4 respectively. The angled fixture supports the ERA cassette from sides, so the jet does not encounter any wood material inside of the support.

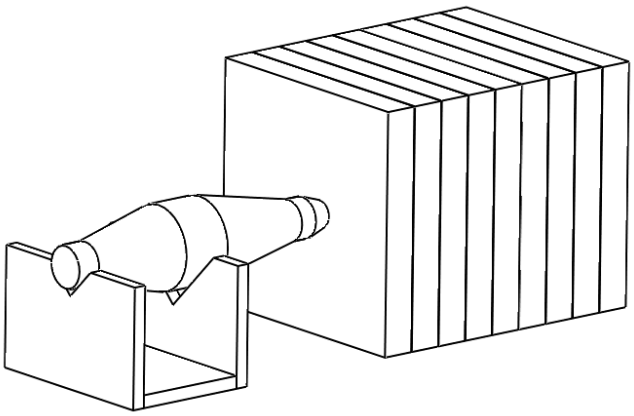

Figure 4.3 Test layout for DOP testing

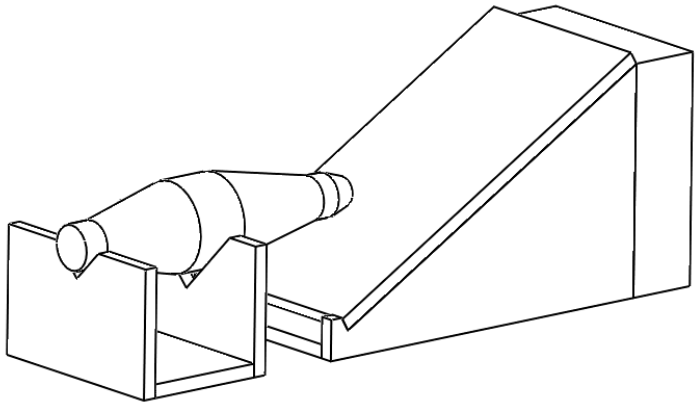

Figure 4.4 Standard test layout for reactive cassettes

4.1.4 Experimental Results

Within the context of the experimental studies, four different groups of tests are organized.

First, the ballistic penetration performance of the 66 mm test warhead is investigated by employing different stand-off distances and by using RHA witness plates. 7 tests are performed to see the effect of stand-off distance on penetration.

An electric circuitry arrangement, which includes make-screens, is used in some of the tests. Make-screens composed of an open circuit, which is shorted when the shape charge jet touches the make-screen layer. This way, time-location data are collected for 6 tests.

Next, the ballistic protection performance of steel/explosive/steel cassettes is examined. In the tests, three different areal density values are considered without changing the explosive thickness and obliquity. Additionally, the effect of flyer plate velocity is examined by increasing the explosive thickness. Lastly, the effect of obliquity is tested. All the cassettes are symmetric, i.e. the thickness (and mass) of the BMP and FMP are the same. In total 17 tests are performed

Then, the ballistic protection performance of hybrid cassettes is investigated by selectively alternating the forward moving plate (FMP) and backward moving plate

(BMP) with alternative materials. Silicon carbide, two grades of alumina, borosilicate float glass and boron carbide are employed as alternative materials. In total 27 tests are performed.

Lastly, ballistic performance of all alternative material cassettes is evaluated. Silicon carbide and alumina plates are selected. Total of 8 tests are performed.

4.1.4.1. Stand-off Characterisation of Test Warhead

Depth of penetration versus stand-off distance characteristic of the test warhead is determined through 7 static firing tests on rolled homogenous armor (RHA) target stacks. A view of a typical test configuration is given in Figure 4.5.

Figure 4.5 Test setup before static firing

Test results are summarized in Table 4.4. The test with make-screen measurements are marked by "*" symbol. All the results are plotted in depth of penetration versus stand-off distance graph, and a curve fitting is performed (Figure 4.6).

Table 4.4 Test Results for Depth of Penetration at Different Stand-Off Distances

Test #	SOD [mm]	DOP [mm]	Measurement
1	325	170.9	No measurement
2*	125	280.4	M1
3*	325	159	M2
4*	125	260.5	M3
5*	175	211.7	M4

Test #	SOD [mm]	DOP [mm]	Measurement
6*	275	180.8	M5
7*	425	148.3	M6

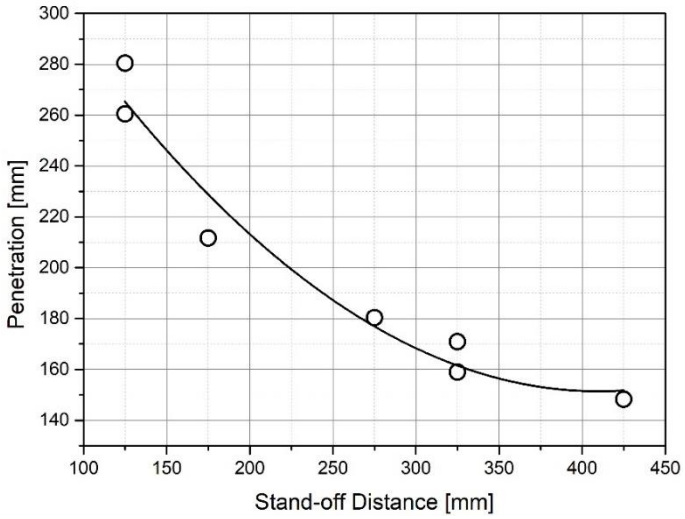

Figure 4.6 Depth of penetration versus stand-off distance curve for the warhead, obtained from test data

Make-screens are placed between witness RHA blocks in order to record the passing/arrival times of shaped charge jet. Typical setup is given in Figure 4.7. The recordings are given in Table 4.5.

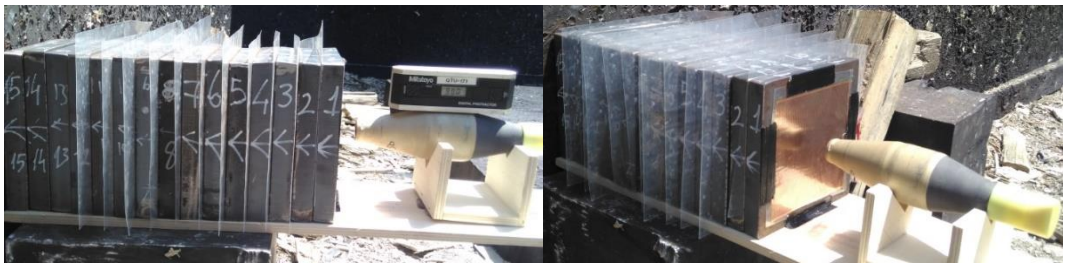

Figure 4.7 Setup for make-screen measurement

Table 4.5 Make screen measurements[4]

M1: 125mm		**M2: 325mm**		**M3: 125mm**	
Pos. [mm]	**Time [µs]**	**Pos. [mm]**	**Time [µs]**	**Pos. [mm]**	**Time [µs]**
0	0	-200	-23.18	0	0
25.4	7.37	0	0	25.4	6.85
50.8	13.09	25.4	6.08	50.8	12.71
76.2	19.47	50.8	12.92	76.2	20.61
101.6	29.2	76.2	43.66	101.6	27.25
127	37.8	101.6	54.82	127	35.41
152.4	46.9	127	66.42	152.4	49.75
177.8	58.8	152.4	N/A	177.8	61.44
203.2	71.78	177.8	N/A	203.2	74.17
228.6	84.88	203.2	126.32	228.6	89.01
254	102.7	228.6	N/A	254	108.7
279.4	153.8	254	N/A	279.4	-
M4: 175mm		**M5: 275mm**		**M6: 425mm**	
Pos. [mm]	**Time [µs]**	**Pos. [mm]**	**Time [µs]**	**Pos. [mm]**	**Time [µs]**
-50	-5.9	-150	-18.07	-300	-37.5
0	0	0	0	0	0
50.8	11.9	50.8	18.13	50.8	12
101.6	25.08	101.6	34.28	101.6	27.1
152.4	45.52	152.4	62.69	152.4	N/A

[4] M1: 125mm represents Measurement 1 at Stand-Off Distance 125mm

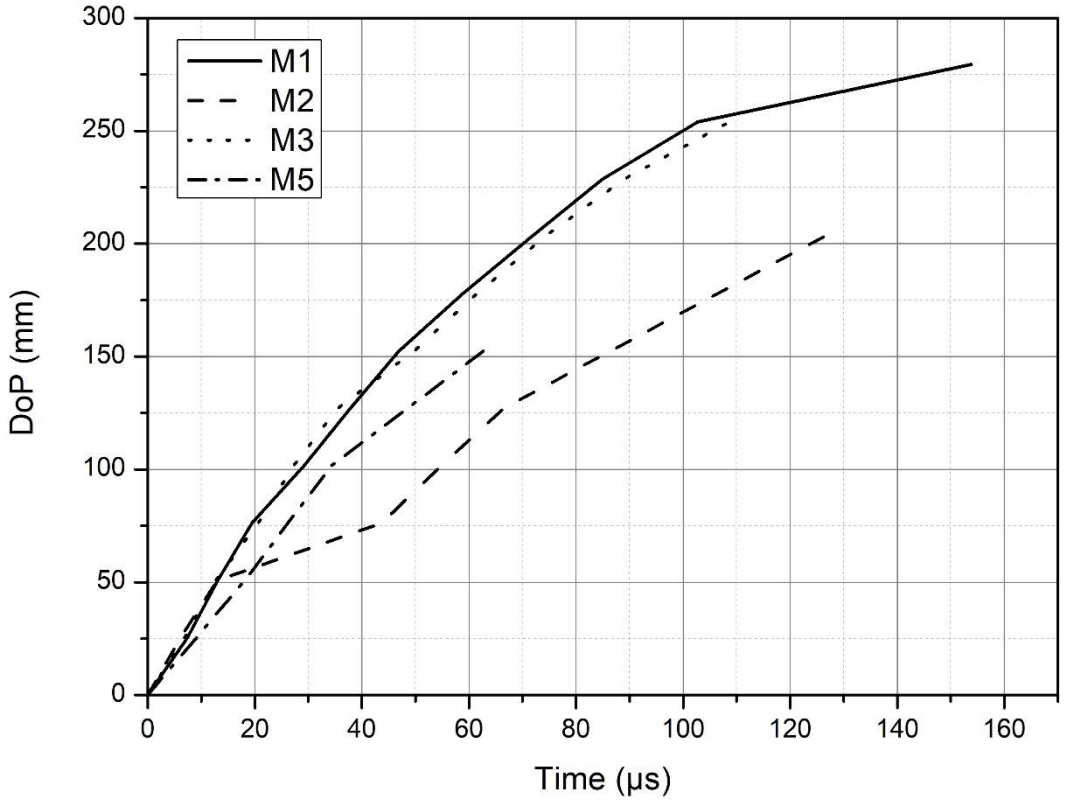

Figure 4.8 Make-screen data comparison for tests with different SOD (Stand-Off Distance) (DOP: Depth Of Penetration)

Jet tip velocity is calculated as 8628m/s, 8475m/s, 8301m/s and 8000m/s after recordings for M2, M4, M5 and M6 tests, respectively.

4.1.4.2. ERA Cassettes

The ballistic protection performance of proposed ERA cassettes are investigated by static firings and measuring residual depth of penetrations in rolled homogenous armor witness plates.

First, performance of steel-steel cassettes is investigated to form bases of comparison for alternative flyer plate arrangements. ERA cassettes had a size of 150x300 mm, and the 300 mm side is placed in angle with respect to the warhead. Steel flyer plates are Armox 500 with 3, 4 and 6 mm nominal thicknesses. The explosive layer is Primasheet 2000, with 3, 5 and 7 mm thicknesses. The detonation velocity of

explosive sheet is 8200 m/s and density is 1.60 g/cm^3 as given in material datasheet. The results of the tests are summarized in Table 4.6.

Table 4.6 Summary of steel/explosive/steel ERA test results

Configuration	**Residual Penetration [mm]**
{3.6St/3/3.6St} at 60°	56.8, 55.8, 51.7
{4.6St/3/4.6St} at 60°	49.2, 36.7, 27.4
{6.6St/3/6.6St} at 60°	79.2, 66.9, 86.1
{3.6St/3/3.6St} at 45°	76.2, 55.4, 93.2
{3.6St/5/3.6St} at 60°	55.5, 28.7, 24.5
{3.6St/7/3.6St} at 60°	40.7, 27.4

Then, forward and backward moving plates are changed with alternative materials with the same weights, in order to understand the effects on residual penetration of those materials. The results are summarized in Table 4.7. The thickness of the explosive layer is 3mm for all tests. A sample test setup can be seen in Figure 4.9. Alternative materials are alumina 99.5% (AD99.5), silicon carbide (SiC), boron carbide (B4C), glass and alumina 98% (AD98). Steel (St) is Armox 500T brand from SSAB AB.

Table 4.7 Summary of alternative material flyer plate test results

Target	**Residual Penetration [mm]**
{3.6St/3/8.15AD99.5} @60°	44.5, 57.4, 37.7
{3.6St/3/9.7SiC} @60°	26.4, 41.4, 82.3
{3.6St/3/15Glass} @60°	103.6, 82.9
{3.6St/3/8.2AD98} @60°	54.2, 48.4, 50.2
{3.6St/3/11.7B4C} @60°	77.9
{8.15AD99.5/3/3.6St} @60°	73.3, 56.5
{9.7SiC/3/3.6St} @60°	60.1, 20.1, 39, 27.2
{15Glass/3/3.6St} @60°	69.2, 76.5, 48.4
{8.2AD98/3/3.6St} @60°	24.1, 20.2, 27.2
{11.7B4C/3/3.6St} @60°	59, 34.9, 39.9
{9.7SiC/3/8.15AD99.5} @60°	61.2, 18.3, 24.3
{8.15AD99.5/3/9.6SiC} @60°	26.4, 43.8, 51.6
{8.2AD98/3/8.15AD99.5} @60°	36.4, 41.5

Figure 4.9 Test setup for ERA cassettes

Mass efficiency (EM) of ERA cassettes is calculated by using Equation 1.8.

4.2. Simulations

Numerical simulation study is performed in the commercial hydrocode SPEED [65]. First, shaped charge jet formation simulation is performed to characterize the jet produced by the test warhead. Then, this jet is used to evaluate the initiation of detonation times of ERA cassette configurations with different BMP materials. Once the initiation times of the explosive layer are determined, ERA cassette impact simulation is performed to observe the events that take place in the interaction of shaped charge jet with the flyer plates. Lastly, ERA flyer plate acceleration simulations are performed without including jet impact.

4.2.1 Jet Formation

Jet formation simulations are performed in 2D axial-symmetric modeling with the help of Eulerian solver. Liner is modeled with Johnson-Cook strength model [66] and failure model [67] parameters of Cu (OFHC) with shock equation of state [68]. The same material model types are used for steel casing. The main explosive charge (octol) and booster charge (tetryl) are represented with shock equations of state for unreacted explosive material [69] and the JWL model for the detonation products [69, 70]. The detonation point is specified as a single point behind the booster charge.

The mesh setup is prepared for a space of 50 mm in radial direction whereas 270 mm in axial direction (which can be extended for investigation of jet elongation analysis).

The origin of the axial axis is taken to be the bases of the liner. Cells with centers greater than 20 mm in radial and 50 mm in axial direction are filled with unused material to save computational time. The “Flow out” boundary condition is applied to allow exit of the detonation products at the boundaries of the mesh area. The simulation setup is given in Figure 4.10.

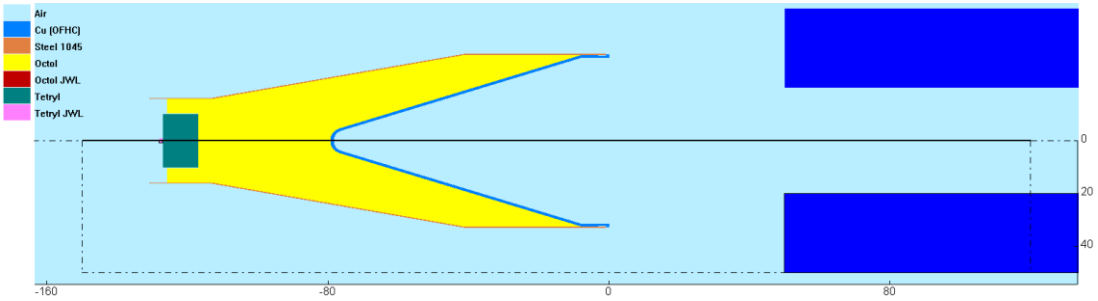

Figure 4.10 Simulation setup for jet formation

Jet formation simulations are performed by using mesh sizes ranging between 0.25 and 0.10 mm. A satisfactory convergence is achieved for the jet tip velocity and the jet velocity distribution at 0.10 mm mesh size. The formed jet is elongated to SOD (Figure 4.11). Then, the front part of the jet (that participates in penetration process) that has velocities greater than 2.8 mm/μs is used for remapping into 3D simulations, assuming that the penetration cutoff velocity [71] is not less than 3.0 mm/μs (Figure 4.12).

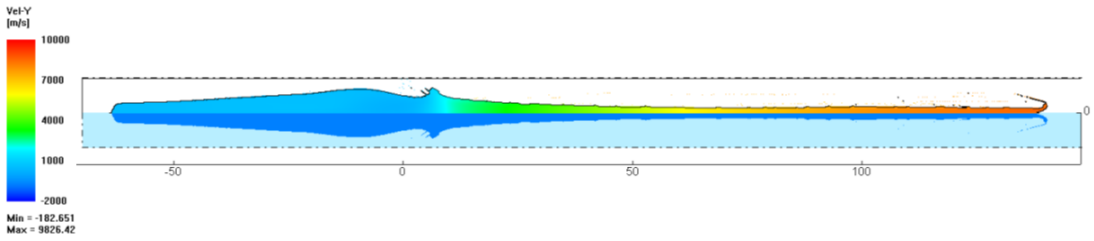

Figure 4.11 Formed jet (at 32 μs)

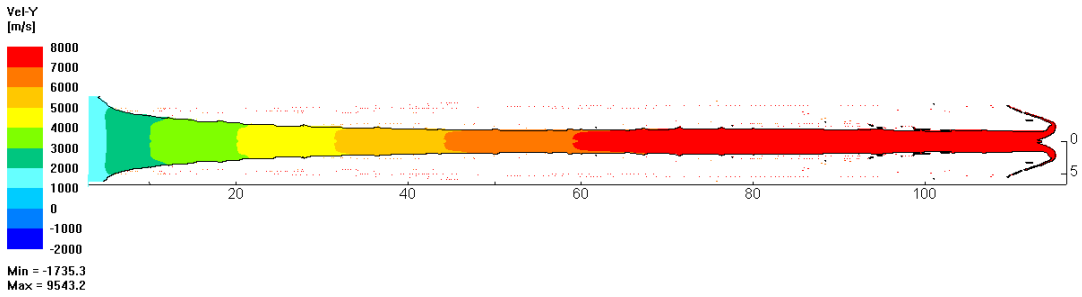

Figure 4.12 The front part of the jet

4.2.2 Initiation of the Explosive Layer

When modeling the detonation of the explosive layer is considered, two different approaches are possible. First, "burn on time" modeling can be employed using JWL [72] model together with user-defined detonation point and time. The other way is to assume an "ignition and growth type" model such as Lee Tarver [73] or History Variable Reactive Burn (HVRB) [74] model. The use of ignition type of material models is limited to problems such as detonation of the explosive layer with impact and it is not suggested to use these models for plate acceleration [65]. Therefore, it is decided to use Lee Tarver detonation model for determining the location and time of detonation for the explosive layer. Then, simulations for flyer plate acceleration and jet interaction are performed with JWL explosive model and user-defined detonation time and location.

Detonation times for reactive cassettes with different types of BMP materials are decided with simulations. Explosive material is modeled with Lee Tarver model parameters of PBXN-110 [75]. The thickness of the explosive layer is kept 3 mm for all the simulations in the study (similar to the experimental matrix). These simulations are run for five different BMP materials, namely Armox 500T, Al2O3 99.5%, SiC, B4C and glass by keeping the FMP steel (screenshots for detonation times for Armox 500T and 99.5% Alumina are given in Figure 4.13 and Figure 4.14, respectively). HVRB model is applied in two configurations for comparison with Lee Tarver.

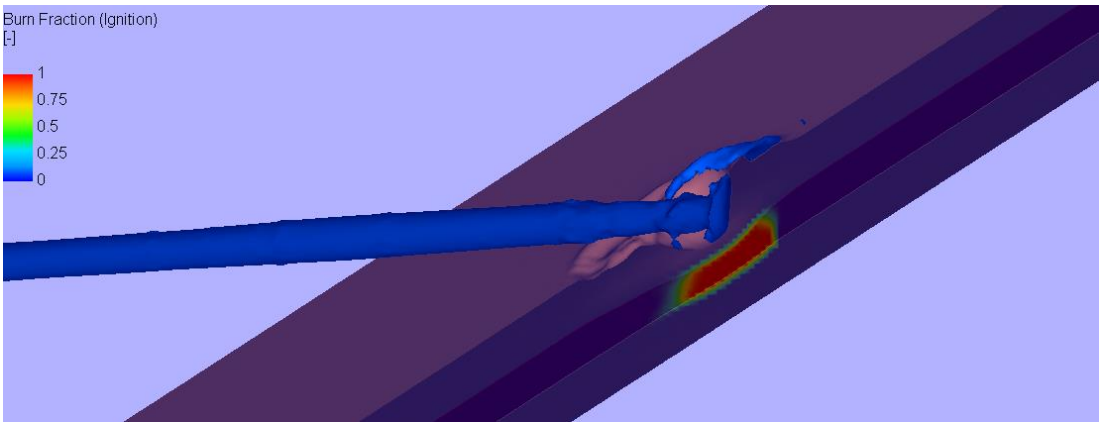

Figure 4.13 Ignition simulation for 3.6mm Armox 500T BMP[5]

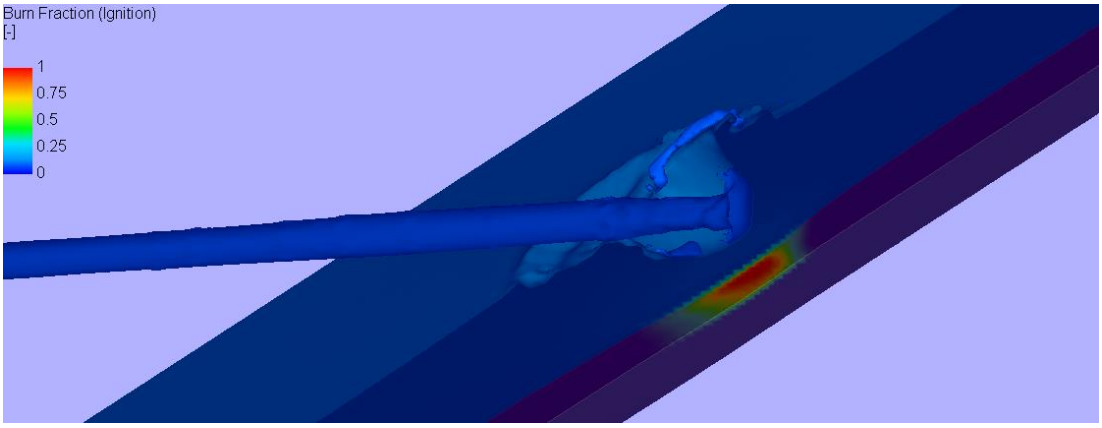

Figure 4.14 Ignition simulation for 8.15mm 99.5% alumina BMP[6]

Detonation times of explosive layer with respect to BMP (front plate) is given in Table 4.8. Note that, starting time of simulation is 32 μs, the instant at which the jet formation is ended and the jet from 2D simulation is remapped into 3D simulation setup. It is seen that, Lee-Tarver and HVRB models yield the same results in terms of detonation times.

---

[5] start of detonation detected at 33.6μs

[6] start of detonation detected at 35μs

Table 4.8 Detonation times of ERA configurations concerning BMP

BMP	**Detonation Time [μs]**
3.6 mm Armox 500T	33.6
8.15 mm Alumina	35
9.7 mm Silicon Carbide	35.6
15 mm Glass	36.8
11.7 mm Boron Carbide	35.7
3.6 mm Armox 500T (HVRB)	33.6
8.15 mm Alumina (HVRB)	35

4.2.3 Interaction of shaped charge jet with ERA cassettes

Shaped charge jet impact on ERA cassette is evaluated with 3D numerical hydrocode simulations. The simulation setup is established large enough to accommodate maximum 40 mm thick ERA cassettes (at 60° impact angle) and front part of the shaped charge jet. Half symmetry is employed throughout all 3D numerical simulations. The element size is kept 0.5 mm at the direction of the impact (x-axis) and at the other direction (z-axis) lying in the symmetry plane. In the direction perpendicular to the symmetry plane (y-axis), 0.5 mm is attained for 10 mm (keeping in mind, it is in the vicinity of the impact) and the size is gradually increased to 2 mm at 80 mm distance (mesh size is 5mm greater than the half plate size of 75 mm). Simulation models consisted more than 13 million elements.

Next, material models for the flyer plates are selected. It is decided to employ the Johnson-Holmquist-2 material model [76] for alumina, silicon carbide, boron carbide and glass, and Johnson-Cook strength model for Armox 500T material in ERA. Material model parameters for alumina (99.5%), silicon carbide, boron carbide and glass are given in Table 4.9, and for Armox 500T are given in Table 4.10.

Table 4.9 Material model parameters of non-metallic flyer plates

Parameter	**Al_2O_3** [77]	**SiC** [78]	**B4C** [76]	**Glass** [79]
Ref. Density	3890	3163	2510	2530
Bulk Modulus K1 (GPa)	231	204	233	45.4
Pressure Coefficient K2 (GPa)	-160	0	-593	-138
Pressure Coefficient K3 (GPa)	2774	0	2800	290

Parameter	**Al_2O_3** [77]	**SiC** [78]	**B4C** [76]	**Glass** [79]
Spec. Heat Capacity cv (J/kg/K)	850	810	900	503
Shear Modulus G (GPa)	152	183	197	30.4
Hugoniot Elastic Limit (HEL) (GPa)	7	14.6	19	5.95
Tensile Strength T (MPa)	462	370	260	150
Intact Strength Coeff. A	0.88	0.96	0.927	0.93
Intact Strength Exp. N	0.64	0.65	0.67	0.77
Strain Rate Coeff. C	0.007	0	0.005	0.003
Frac. Strength Coeff. B	0.45	0.35	0.7	0.088
Frac. Strength Exp. M	0.6	1	0.85	0.35
Max. Fracture Strength	1	0.8	0.2	0.5
Damage Coeff. D1	0.0125	0.48	0.001	0.053
Damage Exp. D2	0.7	0.48	0.5	0.85
Bulking Factor beta	1	1	1	1

Table 4.10 Material model parameters for Armox500T [80]

Parameter	**Value**
Shear Modulus G	84.12 GPa
Initial Yield Stress A	1470 MPa
Hardening Constant B	702 MPa
Strain Rate Constant C	0.00549
Hardening Exponent n	0.199
Temperature Exponent m	0.811
Melting Temperature T_m	1800 K

The explosive layer is modeled with JWL equation of state parameters of PBXN-110 material. PBXN-110 has 87-88% HMX content, and it is evaluated that it will provide slightly higher detonation pressure, with respect to Primasheet (87% RDX). Since the aim of the simulation study is to provide comparison, and since the same percentage of numerical error caused by these two explosives is almost the same, PBXN-110 material is being employed in all numerical simulations.

3D numerical simulation is performed for steel-steel cassettes. Then, BMP and FMP of ERA cassettes are switched with alternative material plates, keeping the areal density constant. A view of the typical start-up configuration is given in Figure 4.15.

Note that the explosive layer is not rendered for viewing the interaction of jet and plate. The starting time of the simulation is 32 μs, which is the jet formation time.

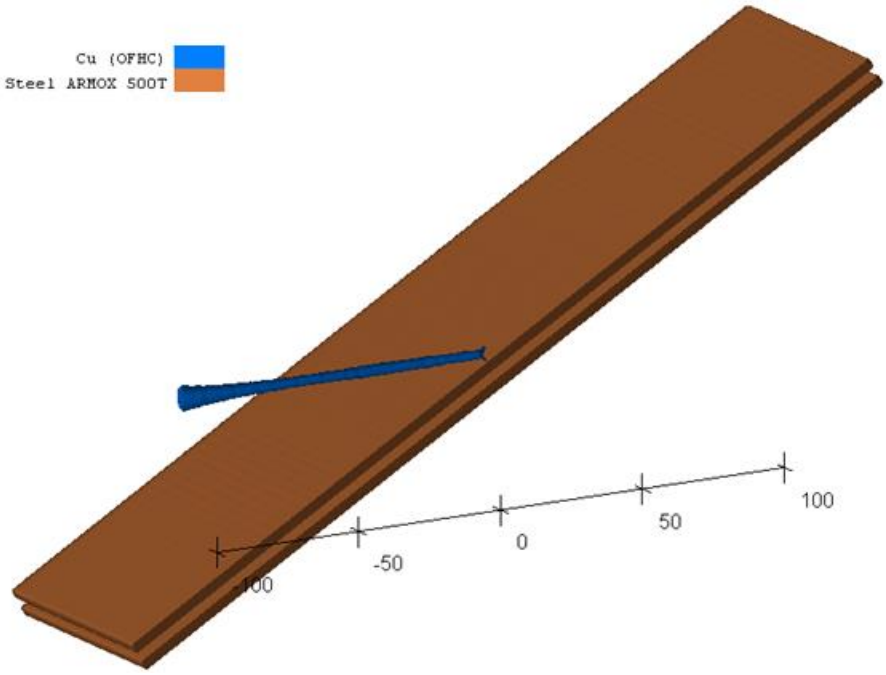

Figure 4.15 Simulation setup for ERA and shape charge jet interaction

CHAPTER 5

RESULTS AND DISCUSSION

5.1. Penetration of RHA and Steel-Steel Cassettes

5.1.1 Verification of Shaped Charge Jet Penetration for Engineering Model

Shaped charge penetration runs are performed for the test charge of 66 mm cone diameter warhead device. The stand of distance is taken as 125 mm, which represents the built-in stand-off distance (BISO) of the warhead. Time-resolved penetration data collected from tests (for Test #2 in Table 4.4 with corresponding measurement data M1 in Table 4.5, given in Figure 5.1) is used for validation of penetration velocity U_p, target resistance parameter R_{tP} and jet strength parameter Y_j. It is seen that an excellent match between the analytical and test results occurs at the beginning of the penetration where the leading parts of the SCJ (which have the highest velocities) are in action. Therefore, the hydrodynamic regime is dominant, therefore strength effects are diminished, and errors in dynamic strength approximation have limited effect. However, at later phases of the penetration, analytic and test results diverge, and variation is observed between test results. It is evaluated that the difference between the analytic calculation and test reading emanates from the relatively simple approximation of target and jet strengths, and possible errors of accuracy in the data acquisition system of the test setup. The approximation of dynamic strengths in penetration equations is to assume a single strength value for each material in a highly dynamic phenomenon.

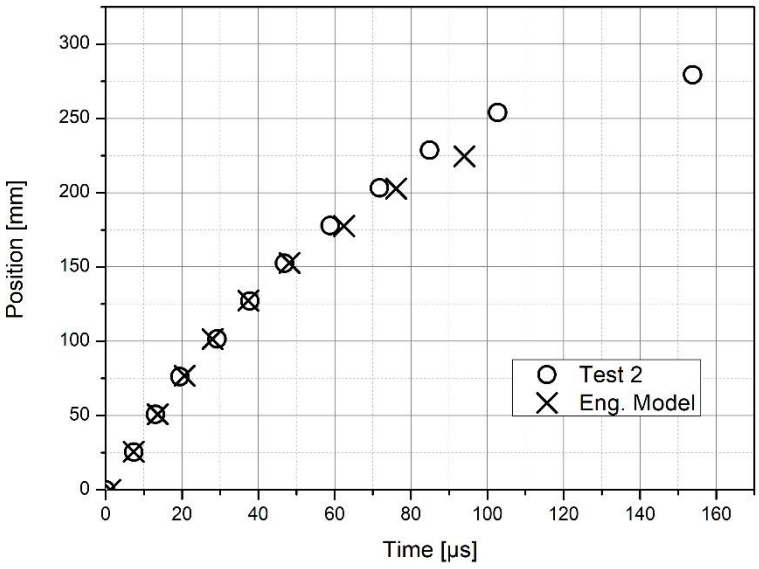

Figure 5.1 Comparison of time-resolved jet penetration into RHA at BISO

Moreover, crater diameters in the target plates are compared in Figure 5.2. These results validate the selection of R_{tR} and Y_j values and confirm the velocity and diameter distribution along the shaped charge jet. This comparison is significant since the velocity and the diameter of the shaped charge jet particle decide the crater diameter on the flyer plate. The crater diameter on the flyer plate has the most severe effects on the calculation of the length of jet precursor, along with the flyer plate velocity.

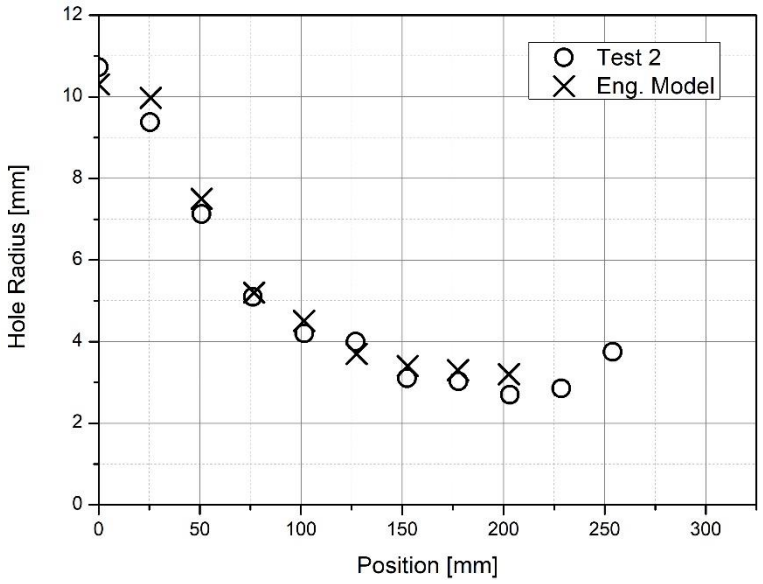

Figure 5.2 Crater diameter versus position graph comparison of test results and engineering model calculations

A comparison of depth of penetration (DOP) data is given in Figure 5.3. It is seen that the model can represent the stand-off distance behavior of the jet, although the penetration at built-in stand-off distance is less than the test results. It is evaluated that representation of penetration value at 325 mm stand-off distance is critical since, it represents the position of witness block in test configuration (Figure 4.2). The variation on the penetration value at BISO is caused by the modeling of the tip part of the jet, which deviates from the flight path of the jet as a result of drift velocities, at longer stand-off distances.

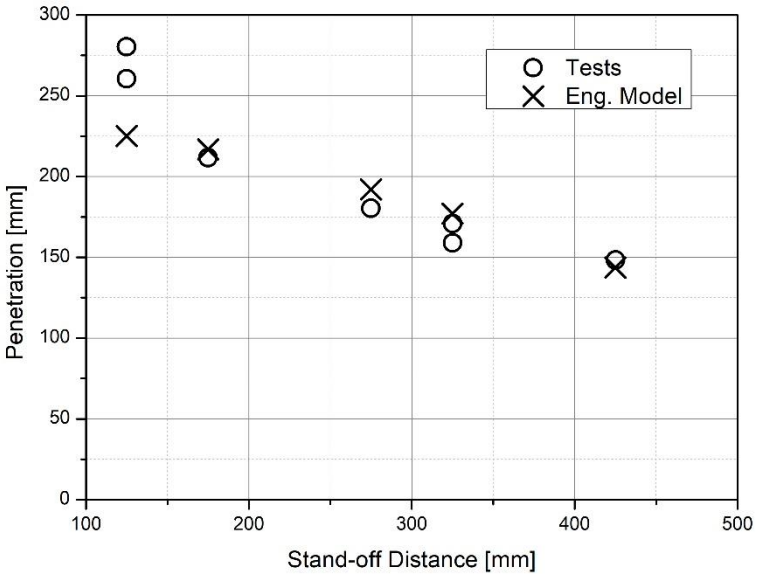

Figure 5.3 Depth of penetration (DOP) as a function of stand-off distance (SOD)

5.1.2 Verification of Penetration Behind ERA for Engineering Model

Comparison of test results with engineering model for varying steel flyer plate thickness is given in Figure 5.4. The explosive thickness and reactive cassette obliquity with respect to shaped charge jet flight direction is kept the same and flyer plate thickness is varied for a symmetric cassette (i.e. BMP and FMP layer thicknesses are equal). The test results indicate increasing residual penetration up to 6mm flyer plate thickness. The comparatively low value of residual penetration for 4 mm flyer plate configuration is attributed to variation in warhead performance. The model foresees an increasing residual penetration with increasing flyer plate thickness, up to 6 mm. The residual penetration is calculated from combined effect of flyer plate velocity and crater diameter on the flyer plate. The flyer plate velocity decreases with increasing plate thickness since, the weight of the explosive charge is not altered. The crater diameter, on the other hand, decreases with increasing flyer plate thickness. Thus, the aforementioned two contrasting effects are calculated and the resulting trend is increasing residual penetration (i.e. decreasing performance of the cassette) with increasing flyer plate thickness.

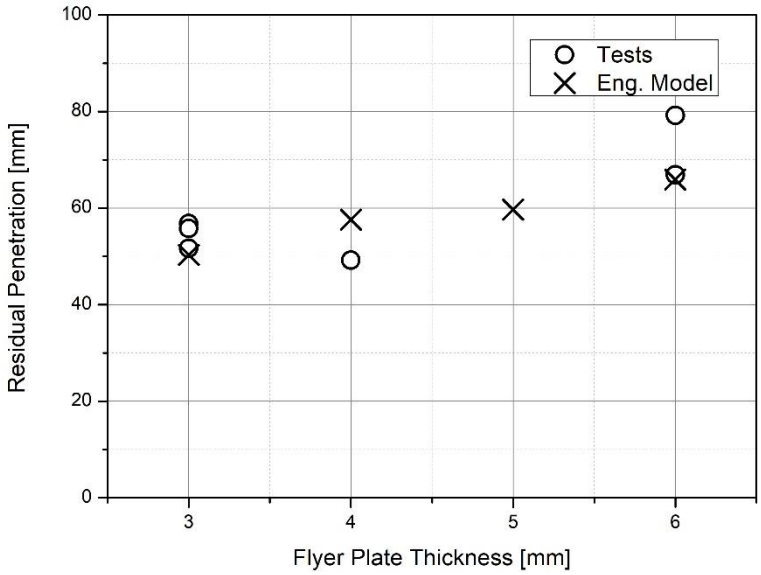

Figure 5.4 Residual penetration as a function of steel flyer plate thickness (x/3/x at 60°)

The dependence of residual penetration on NATO angle of the steel cassette is examined by tests and comparison with engineering model calculations is given in Figure 5.5. The thicknesses of each layer of the cassette is kept the same and the NATO angle (i.e. respective angle between the normal of the FMP and the shaped charge jet flight path) is varied. It is seen that the trend in model calculation correlates well with the test results. This is an expected result since the length of the jet precursor is determined with the time duration that the edge of the initial crater intersects with the flight path of the jet. The length of the jet precursor determines the residual penetration. The velocity of the flyer plate is decomposed into two directions, which are parallel and perpendicular with respect to jet direction. The perpendicular component increases with increasing cassette obliquity. Thus, the time needed for the edge of the crater on the flyer plate to travel and touch the jet flight path decreases. As a result, crater closer happens sooner for cassettes of high obliquity. Once the interaction is established, the jet precursor is established and the tail parts of the jet are disrupted or deflected by the flyer plate interaction.

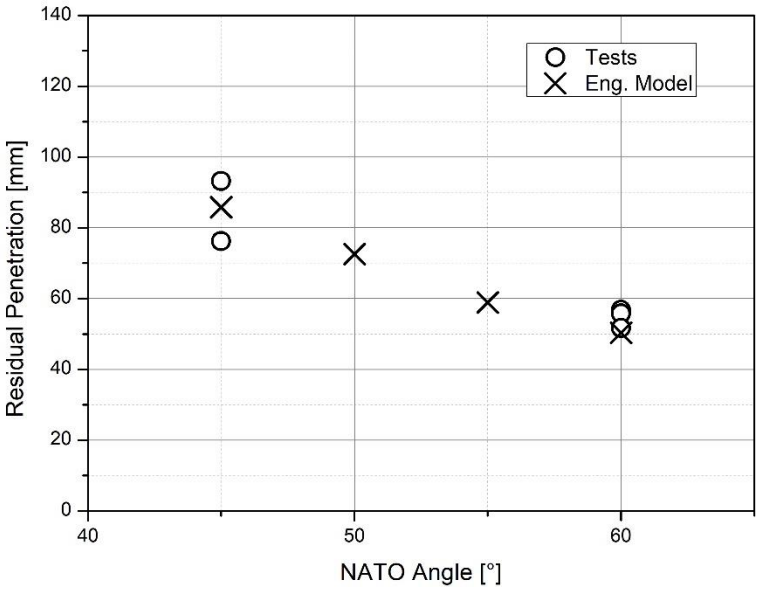

Figure 5.5 Residual penetration as a function of NATO angle (3/3/3 at x°)

The impact of explosive thickness is also investigated by tests, in which steel flyer plate thickness and obliquity of the reactive cassette remained unchanged. Comparison of the experimental results with the model results is given in Figure 5.6. Increasing the thickness of the explosive charge results in a higher velocity of the flyer plate. The time needed for the edge of the crater on the flyer plate to reach is decreased for faster moving flyer plates. Thus, the length of the shaped charge jet precursor decreases with increasing explosive layer thickness. This behavior is seen in both test and model results. Moreover, the effect is parabolic, which is seen in both cases.

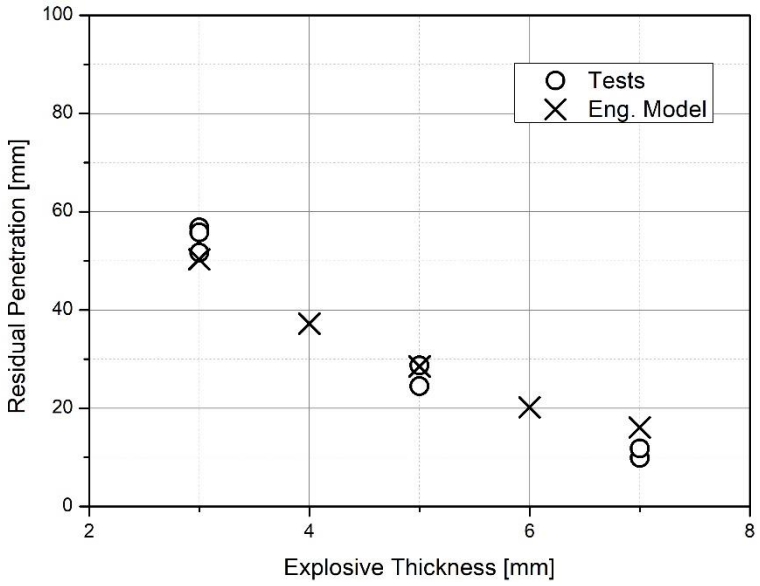

Figure 5.6 Residual penetration as a function of the explosive thickness (3/x/3 at 60°)

Time-resolved penetration data obtained from test results and model calculation are almost identical to each other at the beginning of the penetration, in which high velocity jet segments are in action. On the contrary, the model has divergence from the test results at the later phases of the penetration. This may stem from the following reasons:

- Leading parts of the jet reveal clear hydrodynamic penetration behavior. However, tail parts that are slower approach lower limits of hydrodynamic penetration and strength effects of the target become significant.
- Target strength is highly dependent on strain rate. A complex model can be employed instead of a constant resistance approximation for R_{tp}.
- Uncertainty and errors related to the data acquisition device and electric circuitry, and positioning errors of make-screens during the test setup stage.

Crater hole diameters on the witness RHA plate are also compared with experimental results. Good correlation is observed in general. This in fact, verifies the numerical modeling of the shaped charge jet (i.e. velocity and diameter distribution along with the jet).

The engineering model captures the basic physics of shaped charge jet interaction with explosive reactive armor cassettes. It is assumed that the jet precursor (i.e. escaping jet length) determines the residual depth of penetration. In order to calculate the jet precursor, the idea is to model the initial crater formation on the flyer plates and acceleration of flyer plates. Thus, crater diameter and flyer plate velocity are crucial in calculations. The jet is cut when one of the crater edge on the flyer plates touch the jet flight path. Thus, this interaction happens sooner if the perpendicular velocity component is higher. Keeping in mind this, it is expected that higher obliquities of the cassette or higher thickness of the explosive layer should result in lower residual depth of penetrations. This is shown both by experiments and model calculations. Moreover, the trend in residual depth of penetration is parabolic in case of increasing explosive layer thickness.

When the impact of flyer plate thickness is considered, two effects are contradictory to each other. First, the velocity of the flyer plate decreases with increasing flyer plate weight. Second, the thicker the plate, the lower the crater diameter. It is seen that; the effect of the flyer plate is more significant on the determination of the residual depth of penetration.

The test and model results are quite in correlation for varying NATO angle and explosive thickness analysis.

To sum up; the presented engineering model proved to be a useful tool in the evaluation of shaped charge jet penetration against steel ERA cassettes. Such similar parametric studies can easily be performed to investigate a) the effect of flyer plate and explosive thicknesses and their materials, b) the effects of stand-off distance, the distance between ERA cassette and witness plate, and shape charge jet hit position on the cassette.

The analysis presented is based on metallic materials. Hence, it may be improved to accommodate non-metallic flyer plate materials. This can be achieved through modifications in the plate acceleration and crater formation. Moreover, the

degradation of the shaped charge performance is modeled by employing "penetration cutoff velocities". The results can be improved with physical modeling of jet particles with transverse velocities, so that it will be possible to model whether the particles reach the crater bottom or edges of the crater. Therefore, there will be no need for penetration cutoff velocities. However, this approach necessitates flash X-ray images of particulated jet at two different times. Flash X-ray equipment was not available at the time of experimental study.

5.2. Penetration of Cassettes with Non-Steel Flyer Plates

5.2.1 Simulation Results

The interaction of reactive armor with shaped charge jet proceeds in three phases [41, 30]. First, the jet penetrates the cassette and creates holes in all layers of the cassette and the explosive layer is initiated. The tip of the jet is also eroded. During the second phase, the jet moves forward without any interaction with the flyer plates through the initial holes, while the flyer plates start to accelerate by the explosive action. Only the leading part of the jet is disturbed by the action of detonation products. And in the third phase, the flyer plates establish contact with the jet by the re-interaction of the initial crater edges as a result of plates' movement in the transverse direction to the jet flight path. This phase proceeds until either the edge of the plate or the tail of the jet is reached. The jet is heavily disturbed by the flyer plates in this phase, unlike the front portion of the jet that escapes undisturbed in the second phase.

Theoretical investigations [29, 81] of shaped charge jet interaction with reactive armor reveal that the residual penetration behind the reactive armor cassette correlates well with the escaping undisturbed tip portion of the jet before the interaction starts, which is further supported by experimental evidence [36]. This part is termed "the jet precursor" [82].

Hence it is necessary to take a closer look at the factors that determine the length of the so-called jet precursor. Pioneer work by Mayseless et al [41] showed that the

nature of the interaction between the BMP and the shaped charge jet is deflection, whereas the disruption of the jet is provided by the FMP. In addition, the first major disruption along the jet is caused by the FMP [29], although the BMP is the first to re-interact with the jet in time. Therefore, the length of the jet precursor can be characterized by the time taken by the FMP for re-interaction with the jet. The theoretical approach developed by Mayseless [82] showed that the length of the jet precursor is a function of the initial crater radius on the flyer plate, the reduction of the jet tip velocity due to erosion while perforating the plate, and the duration of the explosive acceleration of the flyer plate.

The simulation study focused on the effect of the flyer plate material selection on the determination of the jet precursor length. The results are presented in three groups; crater diameter on the flyer plate, jet tip erosion, and explosive acceleration of flyer plates.

Simulation of shaped charge jet interaction with the base steel-steel ERA cassette configuration yielded the first phase of interaction between 32nd and 40-42nd microseconds (Figure 5.7). During this stage, the jet penetrated all layers, creating holes on the BMP and the FMP, and the explosive layer is detonated.

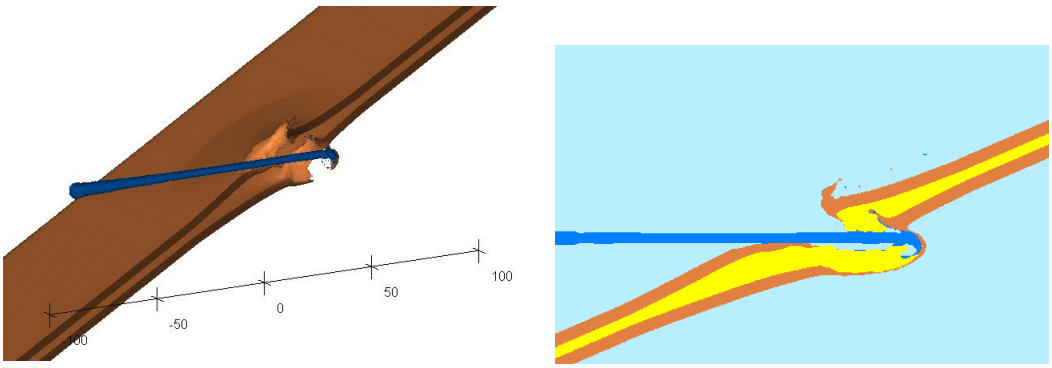

Figure 5.7 Simulation screenshot of jet interaction with steel-steel ERA cassette at 40. μs (left: 3D auxiliary view, right: 2D section view)

During the second phase, the leading part of the jet leaves the ERA cassette undisturbed. This phase ends around the 48th microsecond when the edge of the

initial crater on the FMP establishes contact with the jet and starts disruption of the jet (Figure 5.8). Although the interaction with the BMP is re-established earlier, the effect on the jet is a deflection from its original path, as expected by theoretical investigations.

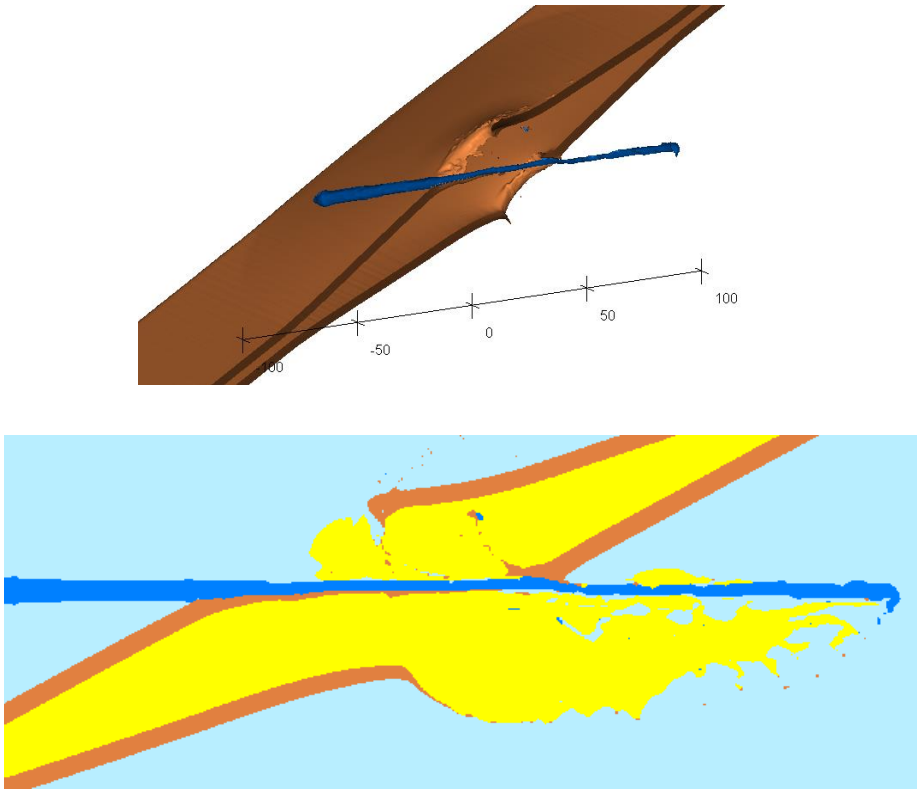

Figure 5.8 Simulation screenshot of jet interaction with steel-steel ERA cassette at 48. μs (up: 3D auxiliary view, down: 2D section view)

The last phase of interaction starts from the 48th microsecond and lasts until the last part of the jet reaches the cassette. A screenshot of the simulation at the 58th microsecond is given in Figure 5.9. It is clearly seen that the BMP deflects the jet whereas the FMP is in a disruptive type of interaction. The jet precursor is seen behind the ERA cassette.

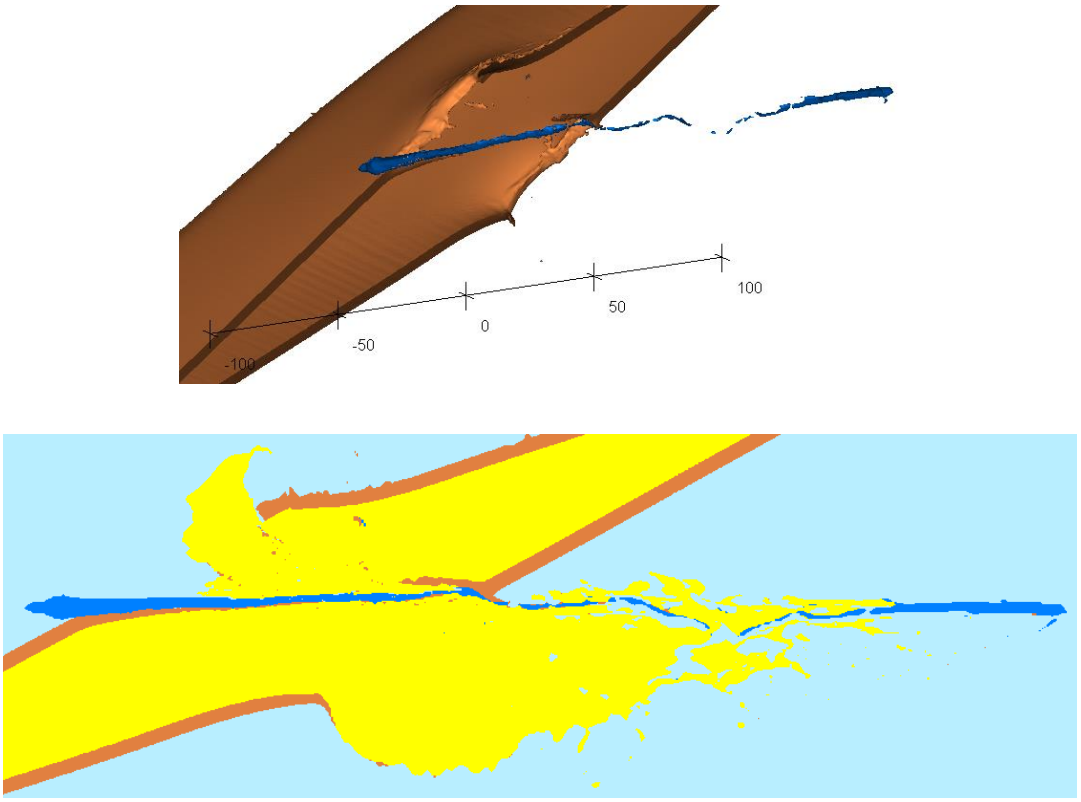

Figure 5.9 Simulation screenshot of jet interaction with steel-steel ERA cassette at 58. μs (up: 3D auxiliary view, down: 2D section view)

As one of the main factors affecting the length of the precursor, the crater diameters on the non-steel BMP and FMP are compared by observing the screenshots of the simulations at 44th microseconds of the simulations, where in all cassette types, the first stage of jet penetration is ended. The simulation screenshots of different BMP and FMP configurations are given in Figure 5.10.

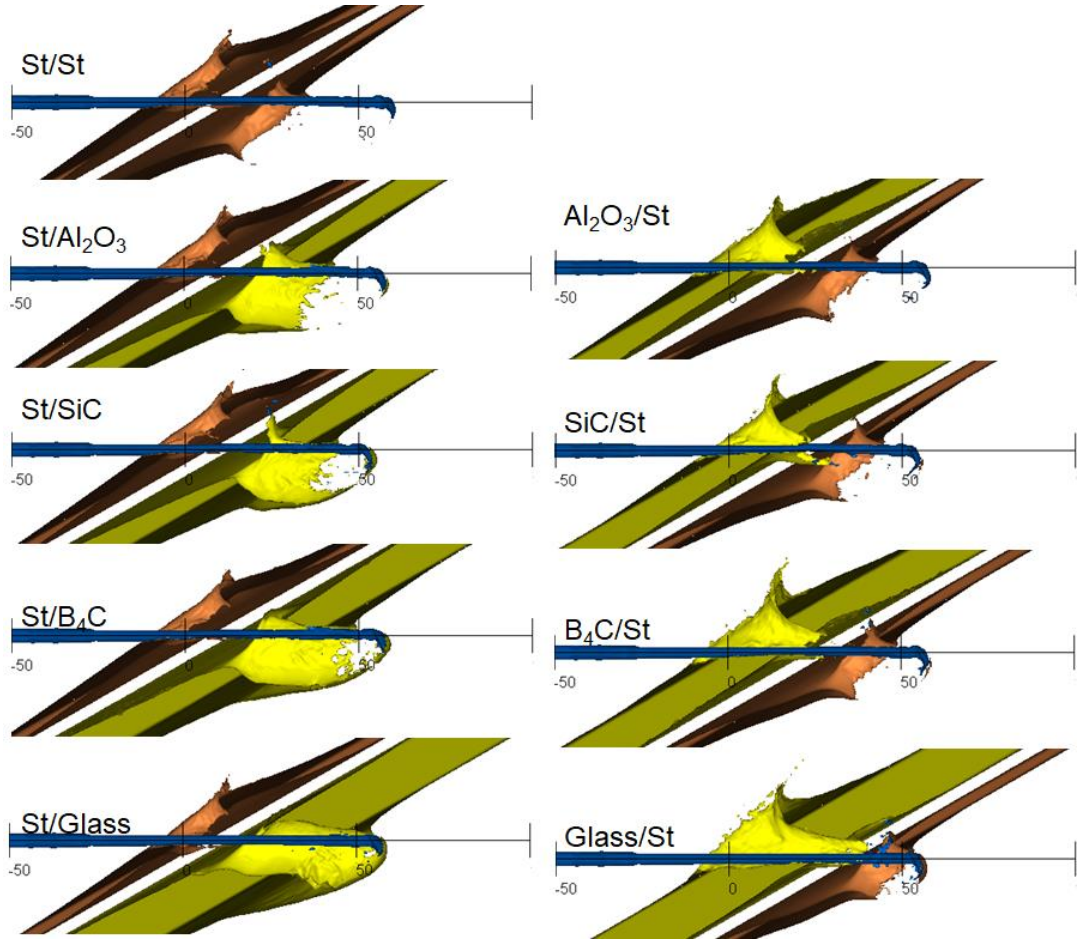

Figure 5.10 Crater diameter comparison of alternative cassette configurations at 44th μs

From Figure 5.10, the crater diameters can be observed as following:

- Crater diameter on the BMP: Glass > Steel ≈ B4C ≈ Al2O3 > SiC
- Crater diameter on the FMP: Glass > Steel ≈ B4C ≈ Al2O3 > SiC

Moreover, jet tip erosions for different configurations are compared by recording new jet tip velocities at the 44th microsecond (Table 5.1). The original jet tip velocity before the impact is 8500 m/s. It is seen that replacing the steel plate with ceramic or glass plate increases the erosion of the jet, which is a result of the lower density according to the dependence of hydrodynamic penetration to density [83]. In

particular, switching the BMP yielded better results as compared to FMP. This is attributed to the fact that the cracked material of the BMP is supported by the FMP, and in the other case the cracked material is free to move out of the way of the jet. Among all the cases, the configuration with glass BMP yielded the best result, however, its ballistic protection is not promising, the reason is explained later.

Table 5.1 Jet tip velocities after the first phase of interaction

BMP	**FMP**	**Tip Velocity (m/s)**
Steel	Steel	7544
Steel	Al2O3	7232
Steel	SiC	7081
Steel	B4C	7084
Steel	Glass	6830
Al2O3	Steel	7160
SiC	Steel	6930
B4C	Steel	6904
Glass	Steel	6358
SiC	Al2O3	6642
Al2O3	SiC	6521

Another major parameter that influences the length of the jet precursor is the acceleration of flyer plates. First, the selection of BMP results in a change in time to detonation. The results depicted in Table 4.8 show that there can be up to 3 μs difference in detonation times of different BMP configurations. However, it is evaluated that this will impart a minute effect on the result since the detonation starts when the jet reaches the explosive layer and the flyer plates start to accelerate at that instant.

Second, the acceleration times of different plate configurations are investigated by simulations. Two gauges are placed on the front and rear surfaces of the flyer plates for recording absolute velocity and displacement, and the explosive layer is detonated without remapping the shaped charge jet into the setup. Simulations are performed for steel-steel, alumina-steel, and glass-steel cases to evaluate each case

for metal, ceramic, and glass. The absolute displacement graphs for the first (gauge on the BMP) and second (gauge on the FMP) are given Figure 5.11 and Figure 5.12. It is seen that the gauge on the glass starts the acceleration with a 2-3 μs delay, which is a very critical shortcoming since this delay causes at least 14mm more of jet precursor to escape without interaction depending on the jet tip velocity. This shortcoming is caused by the combined effect of slow sound speed and increased thickness in glass (or similar low density materials) [84], thus the stress waves causing the acceleration of the plate need more time to reach the other surface of the plate and the reflections take more time. On the contrary, relatively higher sound speeds of ceramics accounts for the increased thickness and the time loss from acceleration is minute. It is interesting to note that, the steel FMPs do not reach the same displacements at the same instant, although the areal densities of each configuration are exactly the same and the cassettes are symmetric in areal density wise. Moreover, the final velocity reached by the glass plate is lower than the steel or alumina plate. It is evaluated that the lower impedance of glass resulted in lower amplitudes of shock reflections in the explosive material, thus symmetric cassette assumption in gurney velocity calculation does not hold.

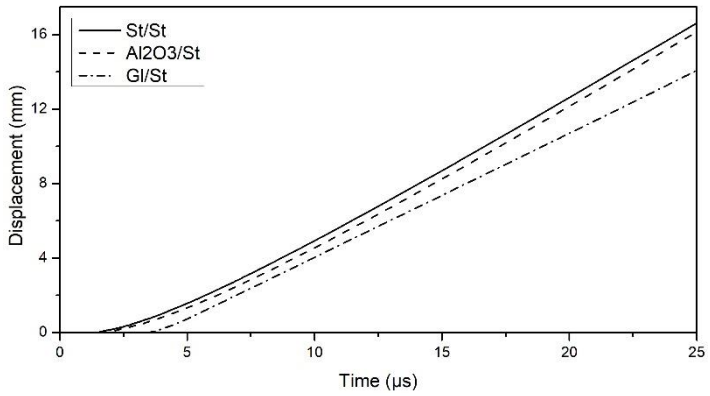

Figure 5.11 Displacement data from Gauge#1 (BMP)

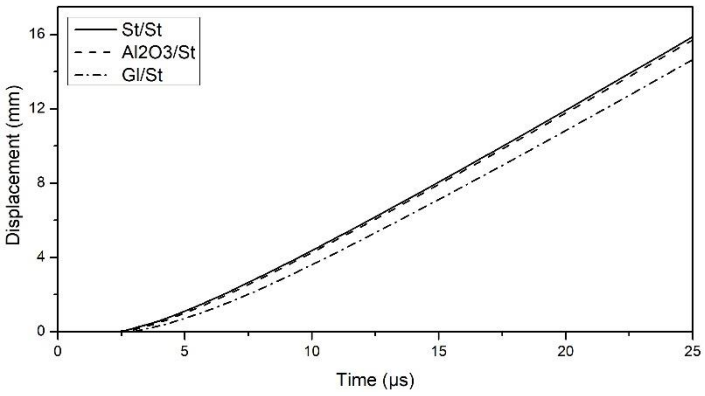

Figure 5.12 Displacement data from Gauge#2 (steel FMP)

Simulation studies revealed the basics of the first and second stages of shaped charge jet and reactive cassette interaction. It is seen that the FMP causes the first major disruption on the jet although the BMP is first to establish re-interaction in time. Thus, the crater diameter and acceleration of the flyer plate are critical for the performance of FMP. Ceramics are found to possess an advantage with smaller crater diameters and does not yield serious drawback for plate acceleration.

The BMP, on the other hand, contributes to the performance of the cassette by causing erosion on the jet tip. It is seen that replacing the steel BMP with ceramic or glass yielded more erosion contrary to replacing the FMP. Moreover, eliminating the jet tip provides benefits to the rear plate since the crater size on plates significantly depends on the velocity of the incoming jet.

5.2.2 Experimental Results

Mass efficiencies (E_M) of the configurations are calculated from the test results by using Equation 5.1, where, P_{REF} is the depth of penetration of the warhead at built-in stand-off distance, P_{RES} is the residual depth of penetration measured in the witness steel pack behind the reactive cassette, AD is the areal density of the cassette and ρ_{steel} is the density of steel.

$$E_M = \frac{P_{REF} * \rho_{steel}}{P_{RES} * \rho_{steel} + AD} \tag{5.1}$$

Since it is needed to compare performances of alternative cassette configurations with the base steel-steel cassette, there is a need to normalize the mass efficiencies. The efficiency of the steel-steel cassette is used for this purpose, where normalized mass efficiencies (E_{MN}) are calculated by dividing mass efficiency of the alternative cassette configuration with that of the steel-steel cassette. In Equation 5.2, $P_{RES,st}$ and AD_{st} are residual penetration and areal density of steel-steel cassette. With the help of this method, the reference depth of penetration of the warhead is eliminated from the calculation.

$$E_{MN} = \frac{P_{RES}*\rho_{steel}+AD}{P_{RES,st}*\rho_{steel}+AD_{st}} \tag{5.2}$$

The comparisons and discussions of test results are given for ERA cassettes by selectively changing BMP, FMP and both flyer plates with non-steel plates are given in the following sections.

5.2.2.1. Non-steel BMP Cassettes

Comparison of test results for normalized mass efficiencies of non-steel BMP ERA cassettes are given in Figure 5.13.

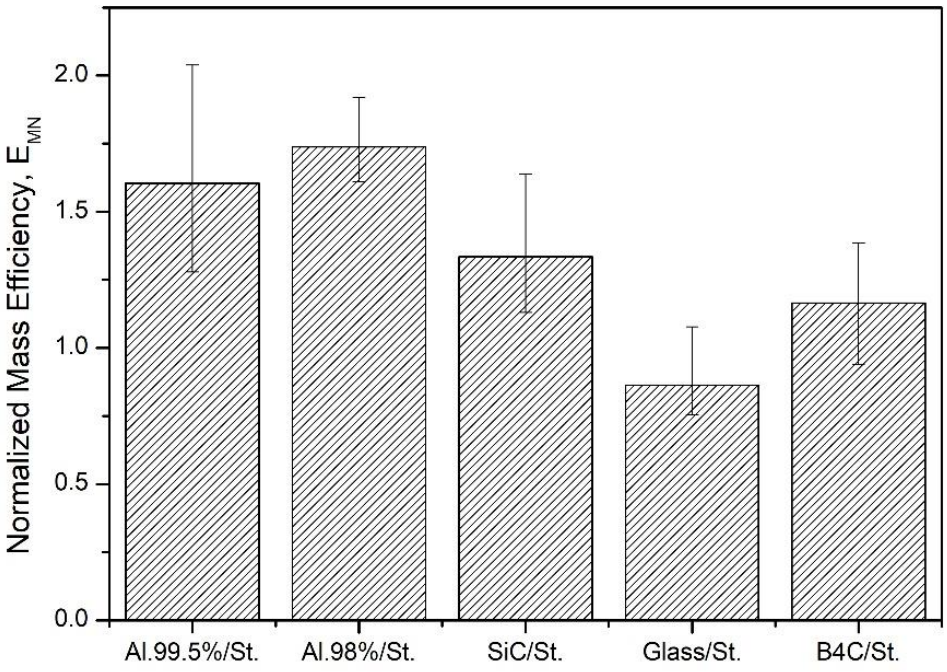

Figure 5.13 Normalized mass efficiencies of non-steel BMP configurations

It is seen that; both grades of alumina, silicon carbide, and boron carbide yielded higher efficiencies with respect to steel. On the other hand; glass revealed slightly lower performance. The highest performance in experiments is achieved by alumina 98% with a 74% increase efficiency with respect to Armox 500T BMP. The worst performing material is borosilicate glass, with a 14% decrease in performance. The poor performance of glass is referred to its slower acceleration, as explained in the former section.

The normalized mass efficiencies of non-steel BMP ERA cassettes are plotted as functions of material properties in Figure 5.14, Figure 5.15, Figure 5.16, Figure 5.17, Figure 5.18, and Figure 5.19. The material properties that are taken into consideration are bulk impedance, compressive strength, density, fracture toughness, Knoop hardness, and Hugoniot Elastic Limit (HEL). A strong relationship is observed concerning density and fracture toughness. As the main function of the BMP is to eliminate the jet tip and erode it as much as possible, it is known that hydrodynamic penetration mainly depends on density for elevated impact velocities such as 7-8 km/s. The material strength effects are diminished so it is plausible to

observe less dependence on compressive strength. Moreover, the second role of the BMP is to support the acceleration of FMP by maintaining shock reflections on the explosive, hence the bulk impedance and density are the required qualities for that purpose. Increased fracture toughness also supports keeping the detonation pressures high, by keeping the integrity of the plate during the initial phases of the detonation.

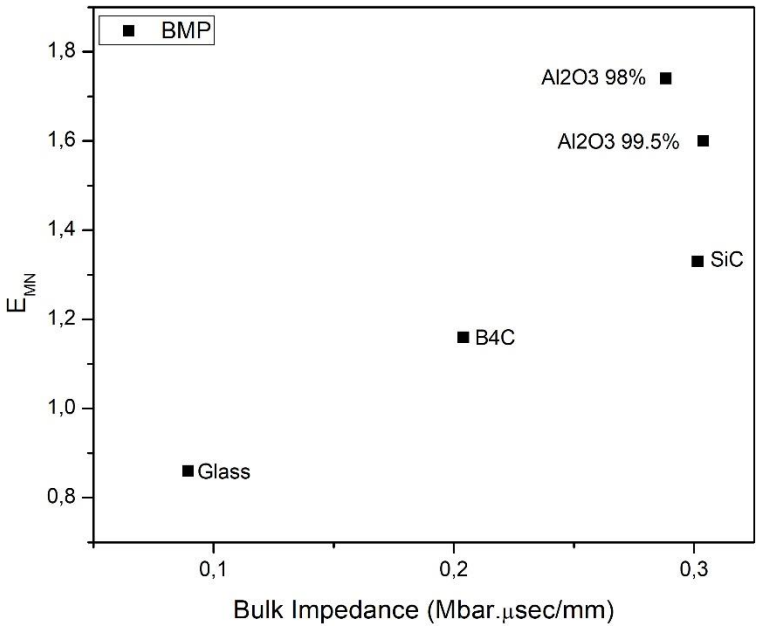

Figure 5.14 Normalized mass efficiencies of non-steel BMP configurations as function of bulk impedance

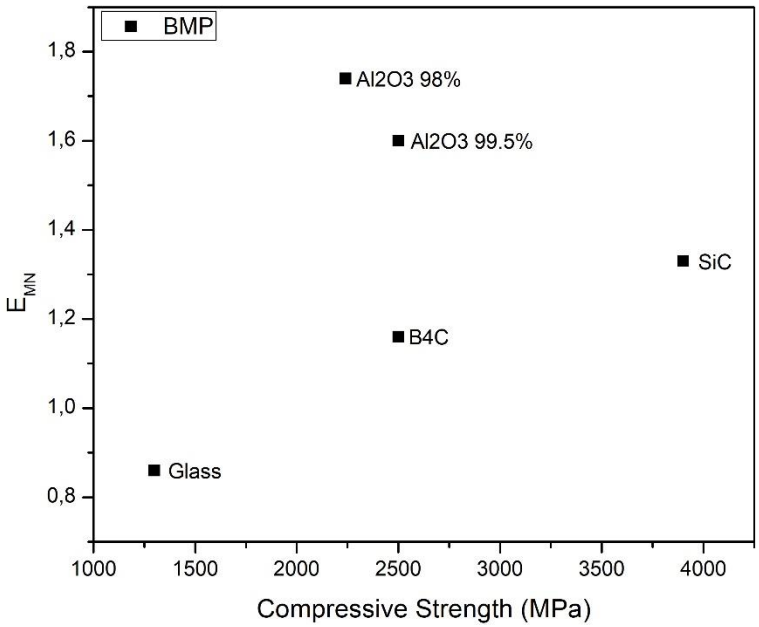

Figure 5.15 Normalized mass efficiencies of non-steel BMP configurations as function of compressive strength

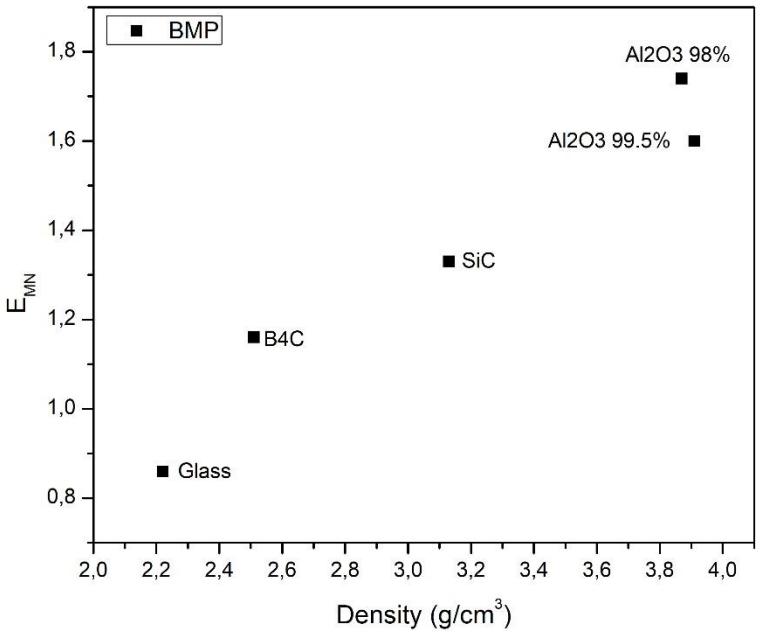

Figure 5.16 Normalized mass efficiencies of non-steel BMP configurations as function of density

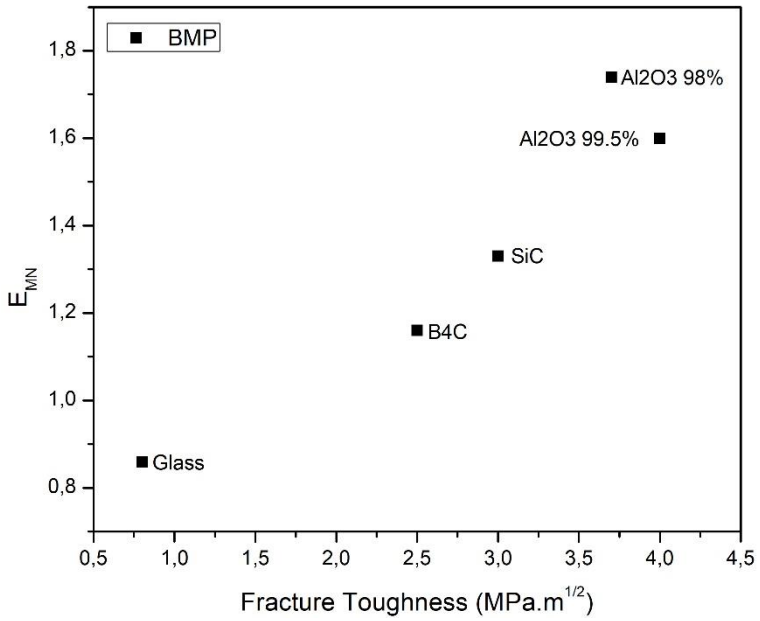

Figure 5.17 Normalized mass efficiencies of non-steel BMP configurations as function of fracture toughness

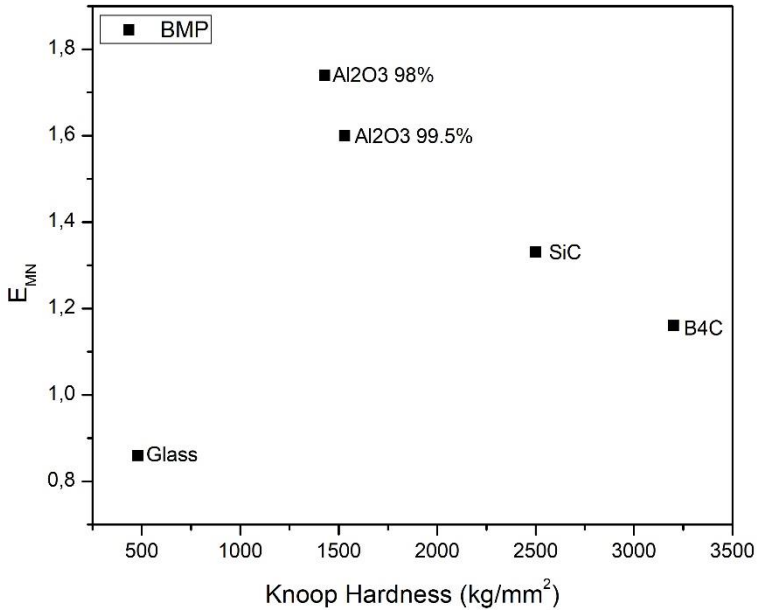

Figure 5.18 Normalized mass efficiencies of non-steel BMP configurations as function of hardness

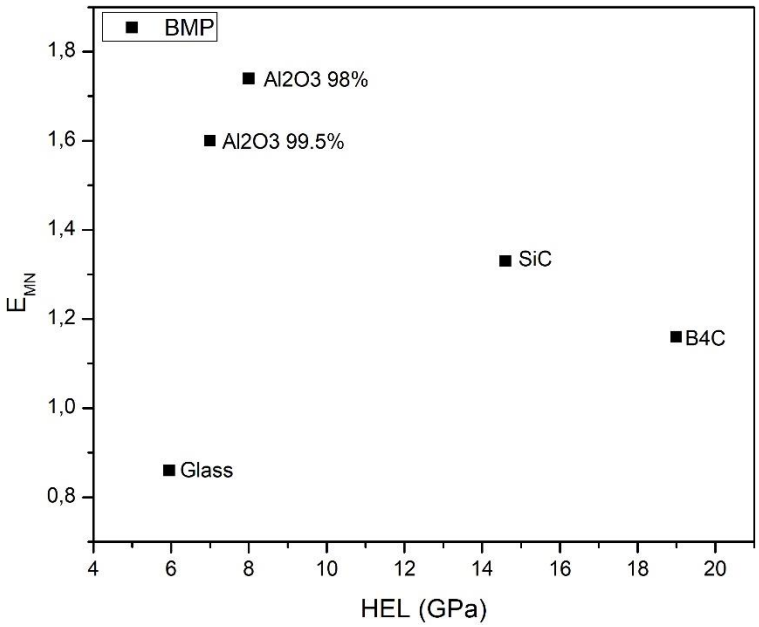

Figure 5.19 Normalized mass efficiencies of non-steel BMP configurations as function of HEL

Surprisingly there is a reverse correlation of Knoop hardness for ceramics. It is evaluated that the Knoop hardness is not a direct factor for the performance but it is an indirect effect of the fracture toughness. It is known that the fracture toughness depends on the ratio of the strength to the hardness [85].

The penetration resistance of ceramics is closely dependent on the HEL at velocities below hydrodynamic penetration [86, 87]. However, the strength effects are well below the impact pressures, so there is no clear relationship for HEL.

5.2.2.2. Non-steel FMP Cassettes

Comparison of test results for normalized mass efficiencies of non-steel FMP ERA cassettes are given in Figure 5.20.

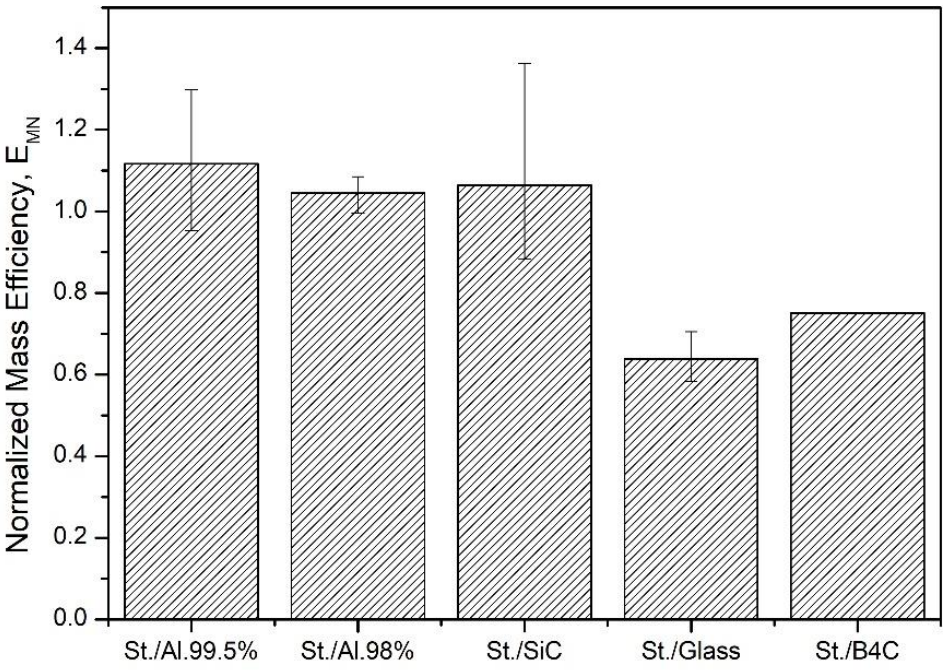

Figure 5.20 Normalized mass efficiencies of non-steel FMP configurations

Experimental results show that, cassette configurations containing alumina (both 99.5% and 98%) and silicon carbide yield slightly higher efficiencies than that of steel-steel cassette. The performance of the ERA cassette highly depends on the FMP's crater diameter and acceleration, so that glass with low sound speed and high thickness, yields slower acceleration. Moreover, its higher crater size is key to poor performance. Boron carbide, on the other hand, yielded surprisingly low performance. Two possible reasons can be addressed. First, the crater diameter is expected to be higher than other ceramics, as the simulations foresee. Second, the interaction performance during the third phase of interaction, which is expected to be disruptive, could be deteriorated by the decreased dynamic strength of this particular ceramic. The reduced performance of boron carbide is attributed to possible phase transformations by Vogler and Fanchini [88, 89]. The strength of the ceramic is significantly decreased once the HEL is exceeded. However, this is not the case for other ceramics like silicon carbide [90].

The normalized mass efficiencies of non-steel FMP ERA cassettes are plotted as functions of material properties in Figure 5.21, Figure 5.22, Figure 5.23, Figure 5.24,

Figure 5.25, and Figure 5.26. It is seen that the performance of the cassette reveals a parabolic correlation with the bulk impedance. Also, the density and the fracture toughness yield a strong relationship. It is shown by the simulation study that the performance of the FMP is a function of crater diameter and plate's acceleration. Thus, a higher bulk modulus will result in a smaller crater and faster acceleration of the plate. The higher the density, the smaller the crater diameter on the other hand. Moreover, the interaction zone of the flyer plate with the jet is larger since the flyer plate is much thicker. This particularly results in improved interaction efficiency of the FMP, which disrupts the center and the slow parts of the jet [84]. A higher fracture toughness supports the acceleration of the BMP by keeping the integrity of the plate for longer at the initial acceleration phases and provides an indirect contribution to the performance.

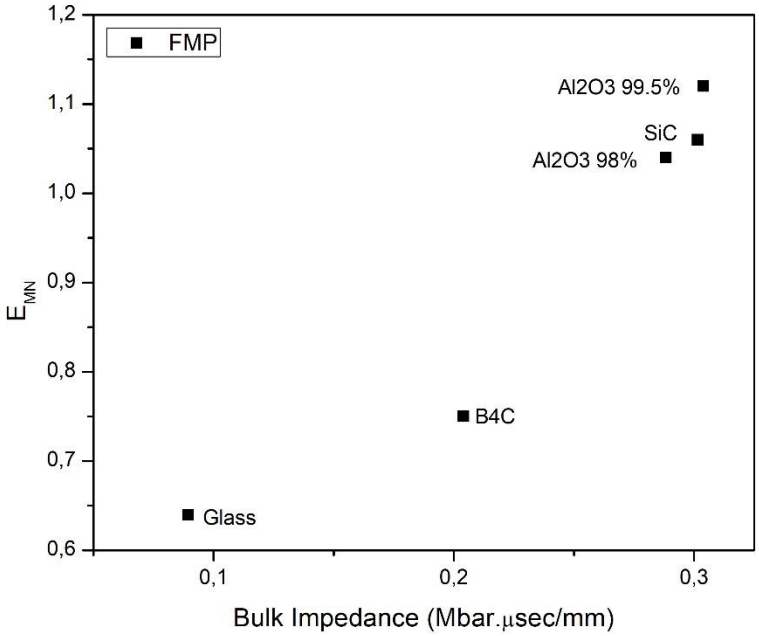

Figure 5.21 Normalized mass efficiencies of non-steel FMP configurations as function of bulk impedance

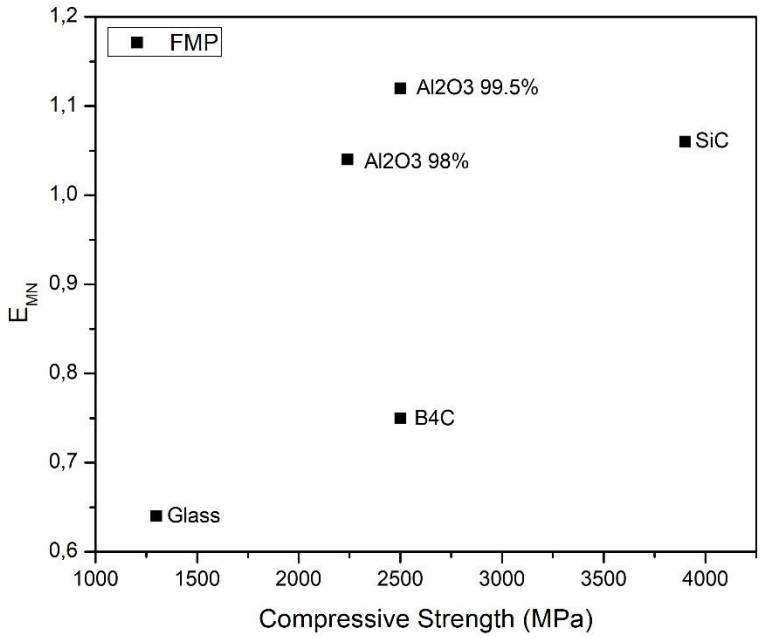

Figure 5.22 Normalized mass efficiencies of non-steel FMP configurations as function of compressive strength

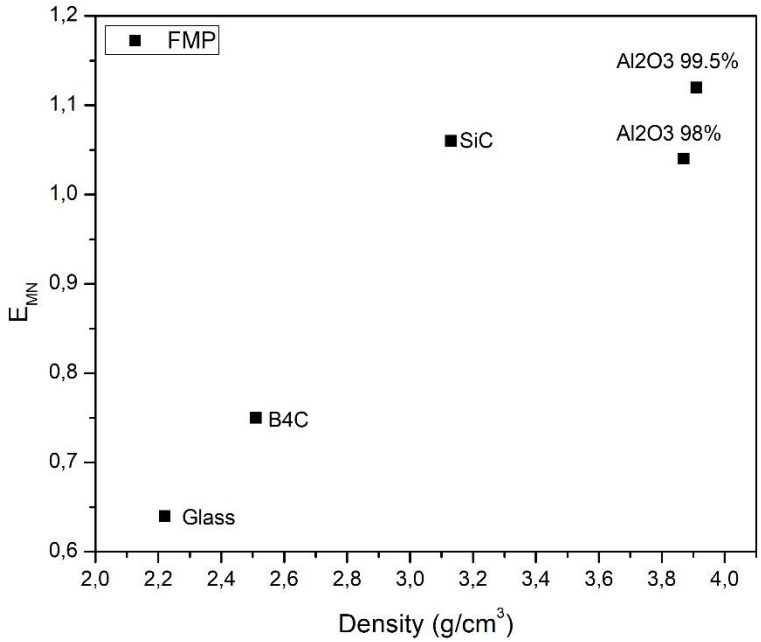

Figure 5.23 Normalized mass efficiencies of non-steel FMP configurations as function of density

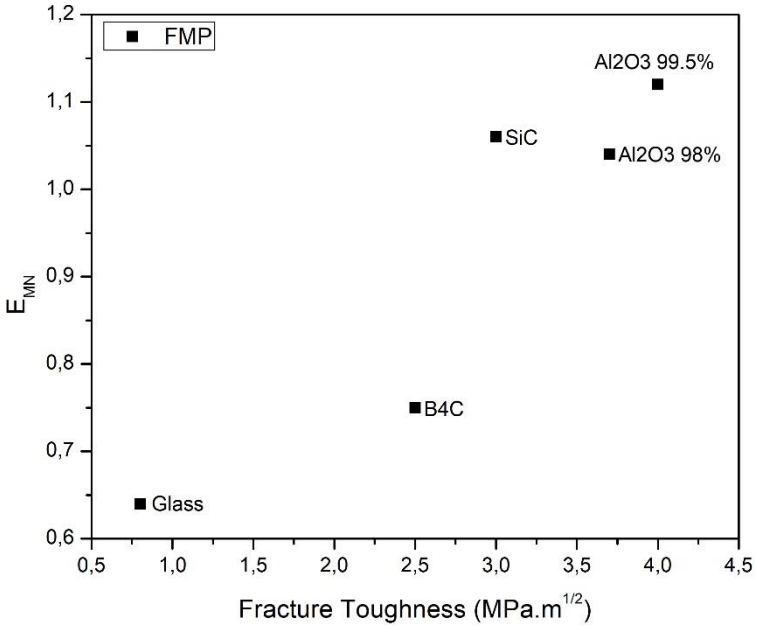

Figure 5.24 Normalized mass efficiencies of non-steel FMP configurations as function of fracture toughness

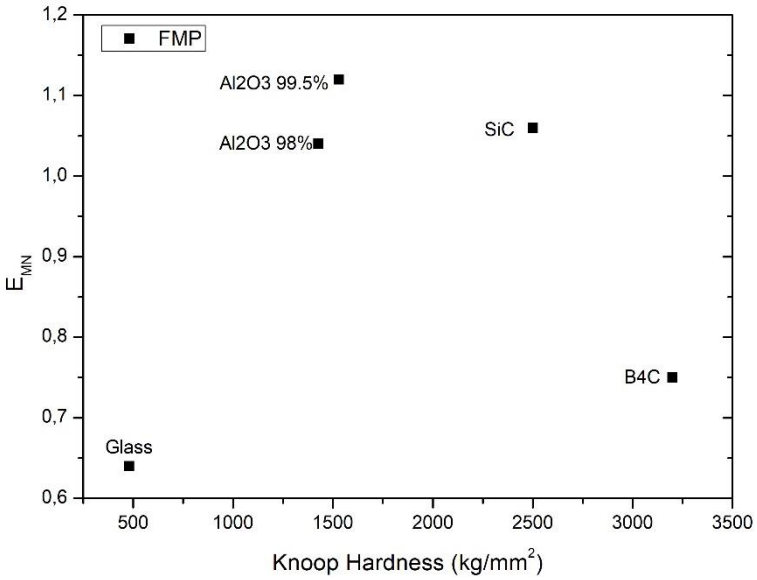

Figure 5.25 Normalized mass efficiencies of non-steel FMP configurations as function of hardness

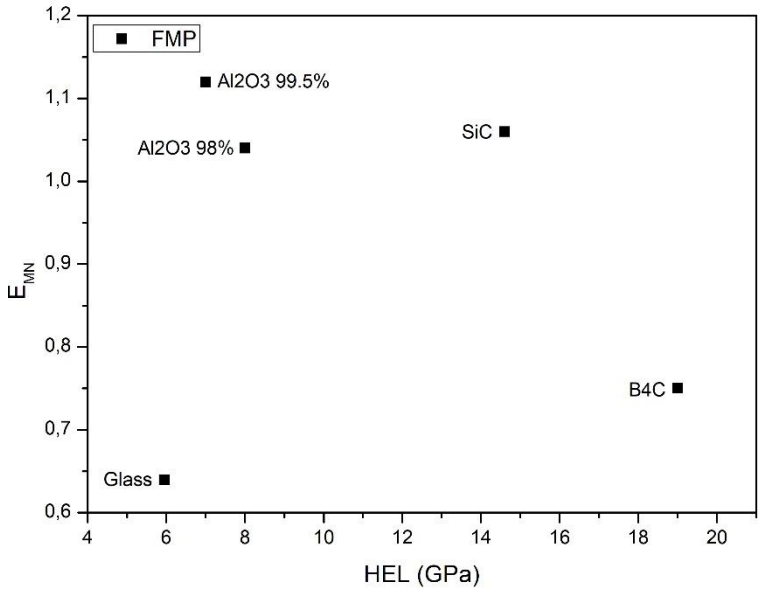

Figure 5.26 Normalized mass efficiencies of non-steel FMP configurations as function of HEL

There is no apparent correlation for compressive strength, Knoop hardness, and HEL. The interaction process during phase 3 is mostly hydrodynamic so dynamic material strength and target penetration resistance is much lower compared to impact pressures. Therefore, it is plausible to observe no correlation for compressive strength, Knoop hardness, and HEL.

5.2.3 Non-steel Cassettes

Comparison of test results for normalized mass efficiencies of non-steel flyer plate ERA cassettes are given in Figure 5.27.

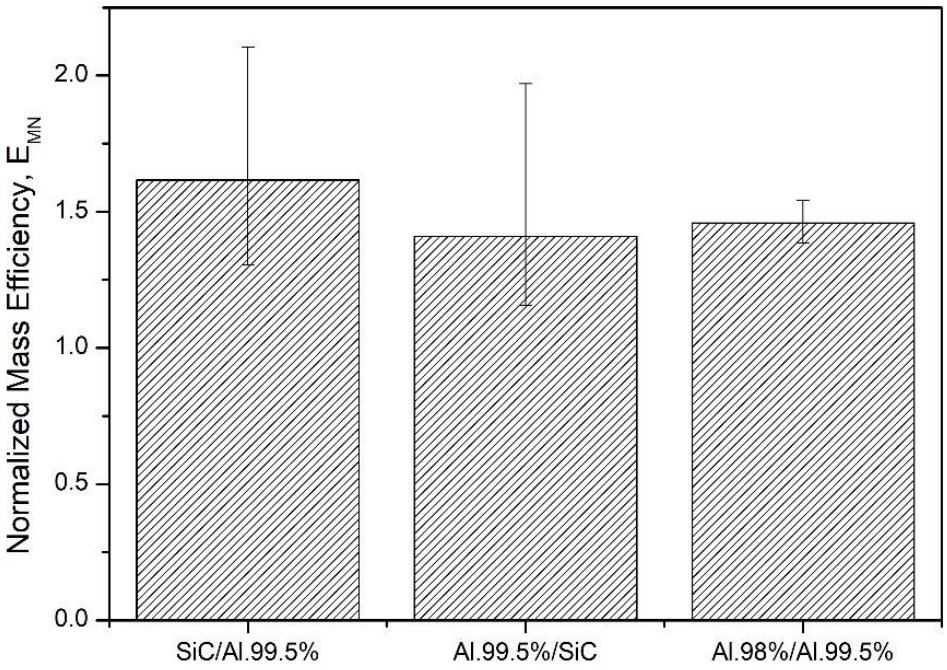

Figure 5.27 Normalized mass efficiencies of non-steel BMP and FMP configurations

It is evaluated that, cassettes from non-steel flyer plates yield higher efficiencies compared to steel. The best performing materials as BMP are silicon carbide and alumina and are coupled with alumina 99.5% and silicon carbide, which are the best performing material as the FMP. These configurations revealed a 62 and 46% increase in efficiency respectively.

The non-steel cassettes enjoy higher performances with the help of contributions of both the BMP and the FMP. The jet tip is much more eroded and the crater diameters are smaller while having no significant loss of plate acceleration compared to steel.

CHAPTER 6

CONCLUSION

In this chapter, a summary of the thesis is presented. Then, the thesis is concluded with final remarks on the subject. Last, recommendations are provided for future studies.

6.1. Summary

The thesis aims to provide the feasibility of employing ceramics and glass as flyer plates in a reactive armor cassette. The idea is to eliminate the collateral damage emanating from flyer plates of explosive reactive armor (ERA) with the mechanism of pulverizing and dispersion within a short distance of interaction. Thus, only the blast effect remains, which is generally lower than the blast from the detonation of the incoming warhead. The first chapter provides fundamentals of jet penetration and ERA working mechanisms. Then, a literature review on the subject is presented with experimental results from other research groups. The rationale of the study is given in this chapter.

The performance of an explosive reactive cassette depends on how much the flyer plates deform the incoming hypervelocity jet and the length of the jet precursor that escapes from the initial hole undisturbed. These two issues are addressed in the second and third chapters. In chapter 2, modes of interaction of flyer plate with hypervelocity jet are proposed. The interaction modes are validated with the help of hydrocode numerical simulations. Then, in chapter 3, an engineering model is proposed for the calculation of the length of the jet precursor and final residual depth of penetration.

Experimental work and simulation study performed within the context of the thesis are presented in chapter 4. Two different grades of alumina, silicon carbide, boron carbide, and borosilicate glass are selected as candidate flyer plate material replacement for steel. First, ballistic penetration tests are performed for symmetric steel/steel cassettes to investigate the impact of flyer plate and explosive layer thickness and obliquity of the cassette. Secondly, candidate ceramic and glass materials are tested by alternatively replacing the steel backward moving plate (BMP) and forward moving plate (FMP) in the cassette configuration. Residual penetrations on the witness plate are recorded and used in calculations of mass efficiencies. Then, best performing alternative flyer plate materials are chosen as BMP and FMP. Subsequently, non-steel cassettes are constructed by the selected materials and are tested. The simulation study is performed as a companion to experimental work to investigate a) the detonation time of explosive layer, b) the acceleration and dispersion of flyer plate and c) the reaction of flyer plate with the shaped charge jet.

The results of the experimental work and simulation study are given in chapter 5 and the discussion of the results is presented. It is seen that the proposed engineering model correlates well with the trends in varying flyer plate, explosive layer thickness, and cassette obliquity. Moreover, investigation of the non-steel flyer plates revealed the performance of selected materials. It is observed that the performance of BMP is improved by increasing the erosion of the jet tip and decreasing the diameter of the initial crater. This is best accomplished by both alumina grades, which possess high fracture toughness and bulk impedance. Although the density of ceramics is lower concerning steel (and hence, the plate thickness is higher), the acceleration is similar with the help of the high sound speed. Poor performance of glass is attributed to slower plate acceleration due to the higher thickness of the plate, slower sound speed, and higher crater diameter.

For the case of FMP, the best performing materials are alumina and silicon carbide. Although BMP established contact with the jet earlier, the resulting interaction slightly deflects the jet. On the contrary, FMP disrupts the jet once the contact is

established, as an outcome of higher mass flux of the flyer plate. Moreover, it is seen that fracture toughness and bulk impedance correlates well with the flyer plate performance.

6.2. Conclusion

The performance of the reactive armor depends on the length of the jet precursor that escapes from the first crater on the flyer plates that is formed after the interaction with the jet tip. Moreover, characterization of the interaction of flyer plate with hypervelocity jet is crucial.

It is demonstrated that the quality of the jet-plate interaction is governed by the mass flux ratio. For that reason, a determination method for regimes of interactions is proposed.

Residual penetration highly depends on escaping tip portion of the jet, which is called the precursor. This is further validated by the proposed model. Increasing the explosive thickness results in increased protection, and the trend of the decrease in the residual penetration is parabolic. Moreover, the higher the obliquity, the lower the residual penetration is.

Ballistic protection performance of ceramics and glass are tested by selectively varying FMP and BMP in symmetric (both plates having similar areal density) cassette configurations. It is shown that it is possible to achieve similar or even higher efficiencies by using ceramic flyer plates, instead of steel.

It is shown that ceramics provide increased efficiencies to ERA cassettes. This is achieved with the help of several mechanisms. First, lower density materials are more efficient in stopping the jet, as a result of hydrodynamic penetration. Therefore, the jet tip is more eroded by ceramic flyer plates.

The increased sound speed of the ceramics yields low degradation of the acceleration, despite the increased plate thickness. Fast acceleration provides earlier

re-interaction of the edges of the initial crater with the jet, resulting in a shorter jet precursor. It is evaluated that, the combined effect of bulk impedance and compressive strength reveal slower crater opening and smaller final crater diameter. It is further evaluated that, higher fracture toughness supports the integrity of the plate during the initial phases of explosive acceleration, hence, the acceleration of the FMP is supported.

Ceramic BMP yielded higher efficiencies concerning steel as a result of a slightly more eroded jet tip. This results in a slower jet tip, and therefore the crater diameter on the FMP becomes smaller. This is an indirect contribution from the lower density BMP. The results are best observed for alumina flyer plates, which possess a combination of high fracture toughness and density.

When the FMP is considered, the role of crater diameter becomes more significant since the length of the jet precursor is decided by the re-interaction time. Hence, higher bulk impedance is needed. Alumina and silicon carbide possess the highest densities and bulk impedances. Therefore, the best results are achieved by these materials. Boron carbide, in particular, yielded surprisingly low performance, due to its potential phase transformations in increased dynamic pressures.

Non-steel cassettes, on the other hand, combine the strengths of BMP and FMP by increased erosion of the jet tip and lower crater diameter on the FMP, without having a significant loss in plate acceleration.

To sum up, ceramic materials provide a big potential as a replacement of steel in ERA cassettes, owing to their lower density, comparable sound speed, and high fracture toughness.

6.3. Future Work

Future research on the subject should consider the collateral effects of ceramic flyer plates. Comparative tests with steel and non-steel cassettes can be performed using thin witness plates located at varying distances.

When the modeling of residual penetration is considered, the calculation method for the crater diameter on the flyer plate can be updated to accommodate ceramic materials.

REFERENCES

[1] J. Carleone, Tactical Missile Warheads, vol. 155, Washington DC: Progress in Astronautics and Aeronautics, 1993.

[2] G. Birkhoff, D. MacDougall, E. Pugh and T. G, "Explosives with Lined Cavities," *Journal of Applied Physics,* vol. 19, no. 6, p. 563, 1948.

[3] D. Pack and W. Evans, "Penetration by High-Velocity "Munroe" Jets: I," *Proceedings of the Physical Society. Section B,* vol. 64, no. 4, pp. 298-303, 1951.

[4] A. Tate, "A theory for the deceleration of long rods after impact," *J. Mech. Phys. Solids,* vol. 15, pp. 387-399, 1967.

[5] F. Allison and F. Vitali, "A New Method of Computing Penetration Variables for Shaped-Charge Jets," U.S. Army Ballistic Research Lab., Rept. 1184, 1963.

[6] R. DiPersio and J. Simon, "The Penetration-Standoff Relation for Idealized Shaped-Charge Jets," U.S. Army Ballistic Research Lab., MR 1542, 1964.

[7] M. Held, "Refined Shaped Charge Jet Penetration Measurement in Various Materials Versus Hydrodynamic Prediciton," in *Proceedings of the 10th International Symposium on Ballistics,* San Diego, 1987.

[8] M. Held, "Protective arrangement against projectiles, particularly hollow explosive charge projectiles". Germany Patent 2008156, 21 February 1970.

[9] D. Rototaev, "How explosive reactive armor was created," *Russian Journal,* 1994.

[10] G. R. Vered, "Evolution of BLAZER reactive armor and its adaptation to AFVs," *Military Technology,* pp. 53-55, 12 1987.

[11] C. F. Fos, "Exploding the ERA myth," *Janes Defence Weekly,* 2 December 1989.

[12] R. Simpkin, "From array to disarray? Tactical aspects of active and reactive armors," *Military Technology,* pp. 18-28, 4 1986.

[13] M. Held, "Overview on reactive armor," in *European Fighting Vehicle Symposium*, UK, 1996.

[14] J. S. Nicholson, M. C. Roggers, R. J. Cox and G. Merritt, "The use of an analytical shaped charge jet and target response model to predict the efficiency of jet disruption by single and multiple explosive armor targets," in *Proceedings of the 9th International Symposium on Ballistics*, Shrivenham, UK, 1986.

[15] O. Chuping and A. Bo, "Study of penetration of jet against reactive armor," in *Proceedings of the International Conference on Ballistics*, China, 1988.

[16] H. S. Yadav, "Interaction of metallic jet with a moving target," *Propellants, Explosives, Pyrotechnics*, vol. 13, pp. 74-79, 1988.

[17] H. S. Yadav and P. V. Kamat, "Effect of moving plate on jet-penetration," *Propellants, Explosives, Pyrotechnics*, vol. 14, pp. 12-18, 1989.

[18] J. Brown and D. Finch, "The shaped charge jet attack of confined and unconfined sheet explosive at normal incidence," in *Proceedings of the 11th International Symposium on Ballistics*, Brussels, Belgium, 1989.

[19] W. Schwartz, "Reactive armor," in *Proceedings of the 10th Seminar on Defence and Technology*, Pakistan Ordnance Factory, 1990.

[20] N. Gov, Y. Kivity and D. Yaziv, "On the interaction of shaped charge jet with a rubber filled metallic cassettes," in *Proceedings of the 13th International Symposium on Ballistics*, Stockholm, Sweden, 1992.

[21] M. Mayseless, E. Marmor, N. Gov, Y. Kivity, J. Falcovitz and D. Tzur, "Interaction of a shaped charge jet with reactive or passive cassettes," in *Proceedings of the 14th International Symposium on Ballistics*, Quebec, Canada, 1993.

[22] S. Friling, M. Benyami and D. Yaziv, "The interaction of shaped charge jet with combined reactive-inert cassettes," in *Proceedings of the 14th International Symposium on Ballistics*, Quebec, Canada, 1993.

[23] M. Held and W. Schwartz, "The importance of jet tip velocity for the performance of shaped charge against explosive reactive armor," *Propellants, Explosives, Pyrotechnics*, vol. 19, pp. 15-18, 1994.

[24] R. C. Goleworthy, "The effect of transverse velocity on shaped charge performance," in *Proceedings of the 7th International Symposium on Ballistics*, Den-Hague, Netherlands, 1983.

[25] R. C. Golesworthy, "Analytical model of shaped charge penetration in the direct and overflying top attack modes," in *Proceedings of the 8th International Symposium on Ballistics*, Orlando, Florida, 1984.

[26] M. Held, "Transverse shaped charges," in *Proceedings of the 8th International Symposium on Ballistics*, Orlando, Florida, 1984.

[27] M. Held and R. Fischer, "Penetration theory for inclined and moving shaped charges," *Propellants, Explosives, Pyrotechnics,* vol. 11, pp. 115-122, 1986.

[28] E. Marmor, Y. M-Bar, M. Mayseless and M. Green, "A model for calculating the penetration of an overflying-top-attack jet into a moving target," in *Proceedings of the 12th International Symposium on Ballistics*, San Antonio, Texas, 1990.

[29] M. Mayseless, "Effectiveness of Explosive Reactive Armor," *Journal of Applied Mechanics,* vol. 78, pp. 051006,1-11, 2011.

[30] M. Held, M. Mayseless and E. Rototaev, "Explosive reactive armor," in *Proceedings of the 17th International Symposium on Ballistics*, Midrand, South Africa, 1998.

[31] R. W. Gurney, "The Initial Velocities of Fragments From Bombs, Shells and Grenades," BRL Report 405, 1943.

[32] V. Grigoryan, N. Dorokhov and I. Kobylkin, Chastnye voprosy konechnoy ballistiki [Particular issues of terminal ballistics], Moscow: BMSTU Publ., 2006.

[33] H. Kaufmann and A. Koch, "Terminal ballistic effects of low density materials used as confinement plates for explosive reactive armor," in *Proceedings of the 22nd International Symposium on Ballistics*, Vancouver, BC Canada, 2005.

[34] S. Bianchi, H. Kaufmann and A. Koch, "Effect of ceramic, fibre reinforced plastics and aluminum used as confinement plates for explosive reactive armors," in *Proceedings of the 24th International Symposium on Ballistics*, New Orleans, Louisiana, USA, 2008.

[35] A. Koch and S. Bianchi, "Protection efficiency of steel and ceramic confinement plates for explosive reactive armours against shaped charges," in

Proceedings of the 25th International Symposium on Ballistics, Beijing, China, 2010.

[36] M. Mayseless, S. Bianchi, H. Kaufmann, Z. Katzir and S. Chanukaev, "Non-metallic reactive armor," in *Proceedings of the 27th International Symposium on Ballistics*, Freiburg, Germany, 2013.

[37] P. J. Hazell, T. Lawrence and C. Stennett, "The defeat of shaped charge jets by explosively driven ceramic and glass plates," *Int J. Appl. Ceram. Technol.*, vol. 9, no. 2, pp. 382-392, 2012.

[38] M. Mayseless, "Controlled-Harm Explosive Reactive Armor (COHERA)". International Patent WO 2003103968 A2, 18 December 2003.

[39] P. J. Hazell, "Low Collateral Damage Explosive Reactive Armour". International Patent WO 2011/128608 A1, 20 October 2011.

[40] E. Liden, A. Helte and T. Eriksson, "Reactive Panels with Non-metallic Cover Plates," in *Proceedings of the 30th International Symposium on Ballistics*, Long Beach, CA, 2017.

[41] M. Mayseless, Y. Ehrlich, Y. Falcovitz, D. Weihs and G. Rosenberg, "Interaction of Shaped Charge Jets With Reactive Armor," in *Proceedings of the 8th International Symposium on Ballistics*, Orlando, Florida, 1984.

[42] M. Held, "Momentum theory of explosive reactive armours," *Propellants, Explosives, Pyrotechnics*, vol. 26, pp. 91-96, 2001.

[43] M. Mayseless, "Reactive armor - simple modeling," in *Proceedings of the 25th International Symposium on Ballistics*, Beijing, 2010.

[44] V. Alekseevski, "Penetration of a rod into a target at high velocity," *Combustion Explosion and Shock Waves,* vol. 2, pp. 63-66, 1966.

[45] I. Kobylkin and E. DA, "Mode Establishment of Interaction Between Long Rods and Moving Plates by the Results of Numerical Simulations," *Engineering Journal: Science and Innovation,* vol. 41, 2015.

[46] W. Walters, W. Flis and P. Chou, "A survey of shaped-charge jet penetration models," *Int. J. Impact Engng,* vol. 7, no. 3, pp. 307-325, 1988.

[47] Z. Rosenberg, Y. Ashuach, Y. Yeshurun and E. Dekel, "On the main mechanisms for defeating AP projectiles, long rods and shaped charge jets," *Int. J Impact Engng,* vol. 36, pp. 588-596, 2009.

[48] S. Hancock, "An Extension of the Umin Model for Cutoff of High Precision Jets," *International Journal of Impact Engineering,* vol. 26, pp. 289-298, 2000.

[49] R. DiPersio, J. Simon and A. Merendino, "Penetration of Shaped-Charge Jets into Metallic Targets," BRL Report No. 1296, 1965.

[50] D. Chi, J. Conner and R. Jones, "A Computational Model for the Penetration of Precision Shaped Charge Warheads," in *Proceedings of the 11th International Symposium on Ballistics*, 1989, 1989.

[51] J. Brown, "Modeling and Experimental Studies of a Family of Shaped Charges in a European Collaborative Forum," in *Proceedings of the 12th International Symposium on Ballistics*, San Antonio, 1990.

[52] J. P. Curtis, "A Stochastic Model of the Penetration of a Shaped Charge Jet into a Semi-infinite Homogenous Target," in *Proceedings of the 15th International Symposium on Ballistics*, Jerusalem, 1995.

[53] K. Werneyer and F. Mostert, "Shaped Charge Penetration Prediction with a Statistical Model Which Incorporates Radial Velocity Data by Means of Bayes Theorem," in *Proceedings of the 18th International Symposium on Ballistics*, San Antonio, 1999.

[54] N. Barnea, N. Sela and M. Ravid, "An analytical model for shaped-charge jet interaction with reactive armour and residual penetration," in *Proceedings of the 14th International Symposium on Ballistics*, Quebec, Canada, 1993.

[55] D. Mickovic, S. Jaramaz, P. Elek, N. Miloradovic and D. Jaramaz, "A Model for Explosive Reactive Armor Interaction with Shaped Charge Jet," *Propellants, Explosives, Pyrotechnics,* vol. 41, pp. 53-61, 2016.

[56] R. Golesworthy and I. Townsend, "Penetration Mechanism of the Shaped Charge Jet," in *Tactical Missile Warheads*, Washington, AIAA, 1993, pp. 487-506.

[57] T. Szendrei, "Analytical model of crater formation by jet impact and its applications to calculation of penetration curves and hole profiles," in *Proceedings of the 7th International Symposium on Ballistics*, 1983.

[58] W. P. Walters, W. Flis and P. Chou, "Shaped Charge Jet Penetration Models," in *Proceedings of the 11th International Symposium on Ballistics*, 1989.

[59] G. E. Jones, J. E. Kennedy and L. D. Bertholf, "Ballistic calculations of R. W. Gurney," *American Journal of Physics,* vol. 48, no. 4, pp. 264-269, 1980.

[60] J. Kennedy, "The Gurney Model of Explosive Output for Driving Metal," in *J. A. Zukas and W. P. Walters (editors), "Explosive Effects and Applications"*, New York, Springer, 1997.

[61] Carleone, Joseph, "Velocity of Explosively Driven Liners," in *Tactical Missile Warheads*, Washington, DC, Progress in astronautics and aeronautics, v. 155, AIAA, 1993, pp. 199-222.

[62] P. Naz, "Penetration and Perforation of a Steel Target by Copper Rods - Measurement of Crater Diameter," in *Proceedings of the 11th International Symposium on Ballistics,* 1989.

[63] T. Hartmann, *Training Course Handout,* Ankara: Numerics GMBH , 2013.

[64] C. S. Meredith and J. J. Swab, "Compression Strength of Borosilicate and Soda-lime Silicate Glasses Using a Dumbbell-shaped specimen," ARL-TR-9120, Devcom Army Research Laboratory, 2020.

[65] "SPEED v3.2 Shock Physics Explicit Eulerian / Lagrangian Dynamics Theory Manual," NUMERICS Software GmbH, Mozartring 3, 85238 Petershausen, Germany, 2018.

[66] G. R. Johnson and W. H. Cook, "A Constitutive Model and Data for Metals Subjected to Large Strains, High Strain Rates and High Temperatures," in *Proceedings of the 7th Int. Symp. on Ball.*, the Hague, Netherlands, 1983.

[67] G. R. Johnson and W. H. Cook, "Fracture Characteristics of Three Metals Subjected to Various Strains, Strain Rates, Temperatures and Pressures," *Engineering Fracture Mechanics,* vol. 21, no. 1, 1985.

[68] D. J. Steinberg, "Equation of State and Strength Properties of Selected Materials," LLNL, UCRL-MA 106439 Change 1,, 1996.

[69] B. M. Dobratz and P. C. Crawford, "LLNL Explosive Handbook: Properties of Chemical Explosive and Explosive Simulants," University of California, Lawrence Livermore National Laboratory, Report UCRL-52997, Rev. 2, 1985.

[70] P. C. Souers, B. Wu and J. L. C. Haselman, "Detonation Equation of State ar LLNL, 1995. Revision 3," UCRL-TD-119262, Livermore, CA, 1996.

[71] M. Held, "Penetration Cutoff Velocities of Shaped Charge Jets," *Propellants, Explosives, Pyrotechnics,* vol. 13, pp. 111-119, 1988.

[72] E. L. Lee, H. C. Horning and J. W. Kury, "Adiabatic expansion of high explosives detonation products," Lawrance Livermore National Laboratory, University of California, TID 4500-UCRL 50422, Livermore, 1968.

[73] E. L. Lee and C. M. Tarver, "Phenomenological Model of Shock Initiation in Heterogeneous Explosives," *Phys. Fluids,* vol. 23, no. 12, p. 2362, 1980.

[74] J. McGlaun, S. Thompson and M. Elrick, "CTH - A Three-Dimensional Shock Wave Physics Code," *International Journal of Impact Engineering,* vol. 10, pp. 351-360, 1990.

[75] P. J. Miller, "A SİmplifiedMethod for Determining Reactive Rate Parameters for Reaction Ignition and Growth in Explosives," *MRS Online Proceedings LİbrarY,* vol. 418, pp. 325-330, 1995.

[76] G. R. Johnson and T. Holmquist, "Response of boron carbide to large strains, high strain rates, and high pressures," *J. Appl. Phys,* vol. 85, no. 12, 15 June 1999.

[77] A. Taşdemirci and I. Hall, "Numerical and experimental studies of damage generation in multi-layer composite materials at high strain rates," *International Journal of Impact Engineering,* vol. 34, pp. 189-204, 2007.

[78] C. LeGallic, M. Cauret, J. Y. Tranchet, P. Chartagnac and F. Gil, "A Consideration of Damage in the Interaction Between Tungsten Rod Penetrators and Ceramic Materials," in *Proceedings of the 16th International Symposium on Ballistics*, San Francisco, CA, USA, 1996.

[79] T. J. Holmquist, G. R. Johnson, D. E. Grady, C. M. Lopatin and E. S. Hertel Jr, "High Strain Rate Properties and Constitutive Modeling of Glass," in *Proceedings of the 15th International Symposium on Ballistics*, Jerusalem, Israel, 1995.

[80] P. Skoglund, M. Nilsson and A. Tjernberg, "Fractrure Modeling of a High Performance Armour Steel," *Journal of Physics IV France,* vol. 134, pp. 197-202, 2006.

[81] M. Held and W. Schwartz, "The Importance of Jet Tip Velocity for the Performance of Shaped Charges Against Explosive Reactive Armor," *Propellants, Explosives, Pyrotechnics,* vol. 19, pp. 15-18, 1994.

[82] M. Mayseless, "Jet Plate Interaction: The Precursor," in *Proceedings of the 18th International Symposium on Ballistics*, San Antonio, 1999.

[83] M. Mayseless and R. Genussov, "Jet Penetration into Low Density Targets," in *HVIS 98*, Huntsville, 1998.

[84] M. Mayseless, S. Friling and L. Misiuk, "Re-visiting the mass-flux model for explosive reactive armor and the effect of plate thickness," *Defence Technology,* vol. 15, pp. 779-785, 2019.

[85] J. Sternberg, "Material Properties Determining the Resistance of Ceramics to High Velocity Penetration," *Journal of Applied Physics,* vol. 65, no. 9, pp. 3417-3424, 1989.

[86] A. Tate, "A Theory for the Deceleration of Long Rods After Impact," *Journal of Mechanical Physics of Solids,* vol. 15, pp. 387-399, 1967.

[87] Z. Rosenberg and J. Tsaliah, "Applying Tate's Model for the Interaction of Long Rod Projectiles with Ceramic Targets," *International Journal of Impact Engineering,* vol. 9, pp. 247-251, 1990.

[88] V. TJ, R. WD and C. LC, "Dynamic Behavior of Boron Carbide," *Journal of Applied Physics,* vol. 95, no. 8, pp. 4173-4183, 2004.

[89] G. Fanchini, "Behavior of Disordered Boron Carbide Under Stress," *Physical Review Letters,* vol. 97, p. 035502, 2006.

[90] T. J. Holmquist and G. Johnson, "Characterization and Evaluation of Silicon Carbide for High-velocity Impact," *Journal of Applied Physics* , vol. 97, p. 093502, 2005.

APPENDICES

A. Shaped Charge Jet Characteristics

Shape charge jet formation simulations are performed to characterize the jet of the 66mm diameter shape charge jet. Velocity distributions at different times are given in Figure A.1. The jet has a linear like distribution at time 50 μs. Corresponding cumulative jet mass profile (M(v)), dM/dv and strain rate (dv/dy) graphs are given in Figure A.2, Figure A.3 and Figure A.4.

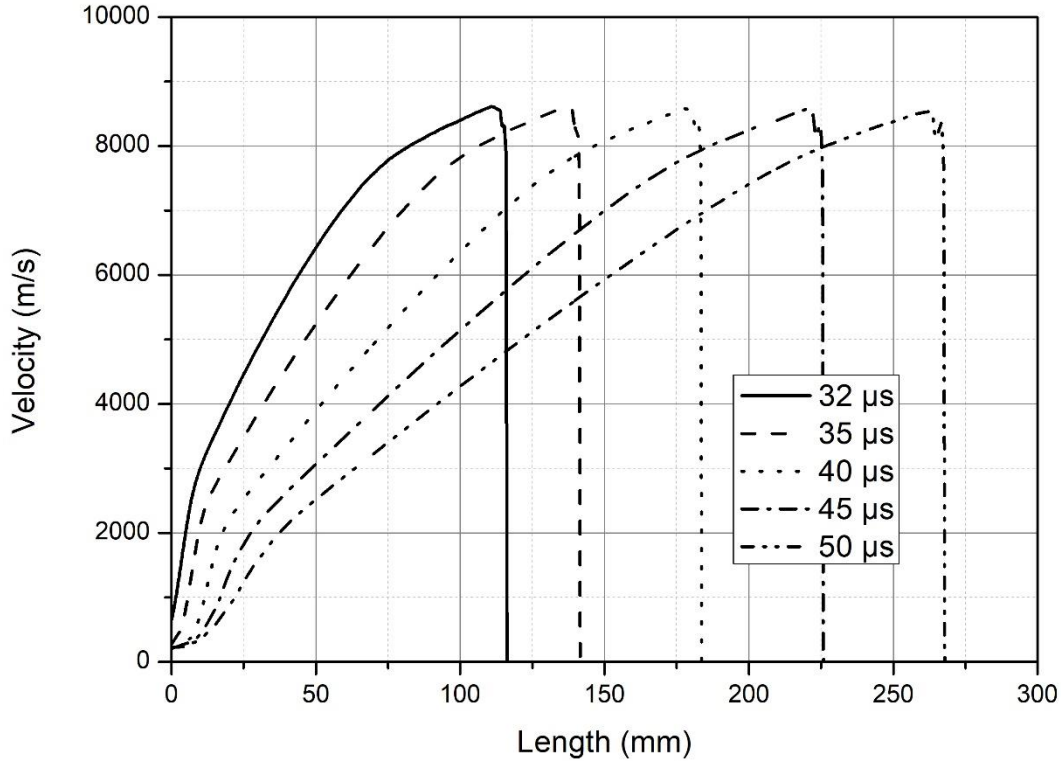

Figure A.1 Velocity distribition at different times

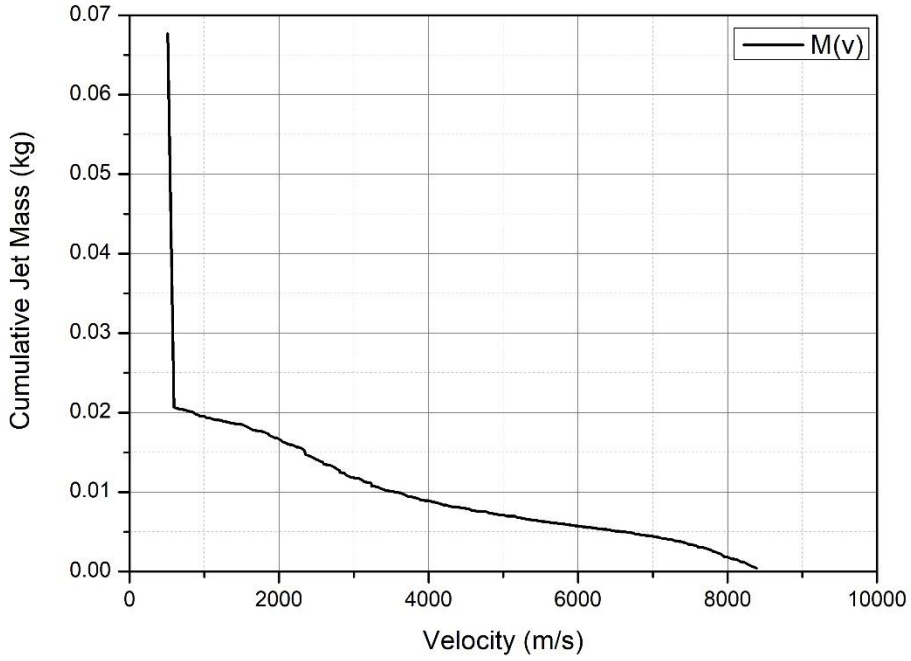

Figure A.2 Cumulative jet mass profile at 50 µs

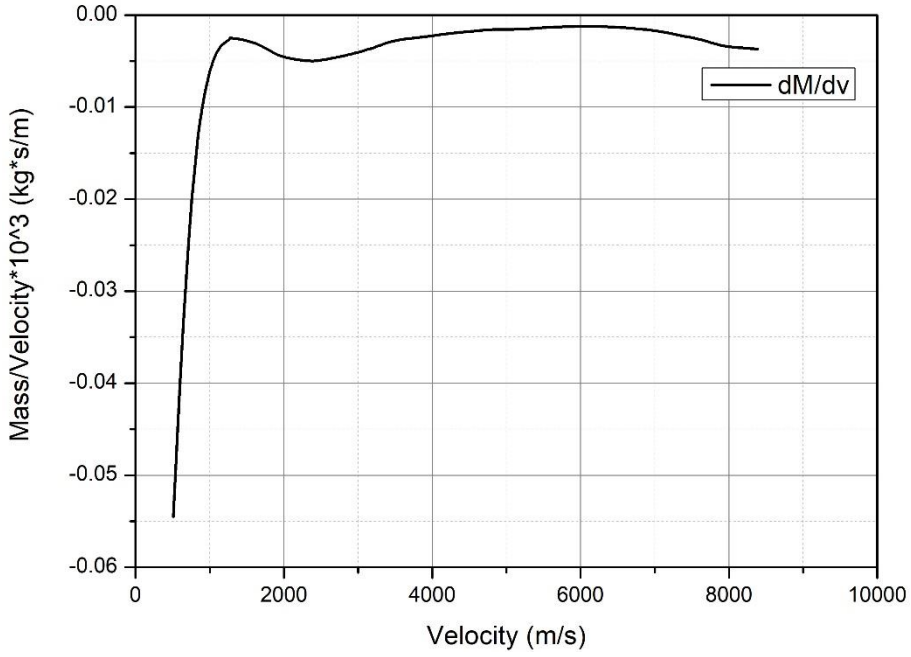

Figure A.3 dM/dv graph at 50 µs

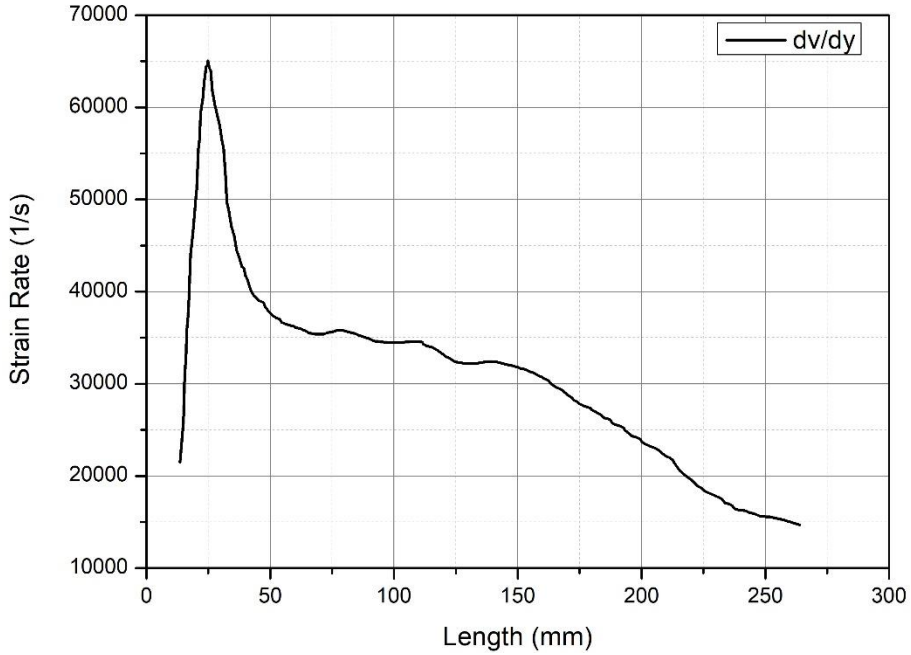

Figure A.4 Strain rate graph at 50 μs

CURRICULUM VITAE

Surname, Name: Deniz, Tansel

EDUCATION

Degree	Institution	Year of Graduation
MS	Dept. of Mech. Eng., METU	2011
BS	Dept. of Mech. Eng., METU	2007
High School	Bornova Anadolu Lisesi	2003

WORK EXPERIENCE

Year	Place	Enrollment
2009-Present	Roketsan Missiles Inc.	Unit Manager
2008-2009	Bias A.Ş.	Engineer
2006-2007	TAI	Part-Time Engineer

PUBLICATIONS

International Conference Publications

Deniz T. and Yıldırım R. O., "Ballistic penetration of hardened steel plates", in Proceedings of the 27th International Symposium on Ballistics, Freiburg, Germany, 2013.

Patents

Kaya A. G. and Deniz T., "Patlama basıncı sönümleyicili parçacık korumalı yangın ilerletmeyen ön patlatmalı sandviç zırh". Türkiye Patent 11797, 15 Ekim 2012.